EVALUATION OF FRACTURE PARAMETERS OF NiTi SHAPE MEMORY ALLOY USING DIGITAL IMAGE CORRELATION

by

Nima Shafaghi

B.S., Mechanical Engineering, Islamic Azad University of Tabriz, 2007

Submitted to the Institute for Graduate Studies in
Science and Engineering in partial fulfillment of
the requirements for the degree of
Master of Science

Graduate Program in Mechanical Engineering
Boğaziçi University

2013

EVALUATION OF FRACTURE PARAMETERS OF NiTi SHAPE MEMORY ALLOY USING DIGITAL IMAGE CORRELATION

APPROVED BY:

Prof. Günay Anlaş (Thesis Supervisor)	.....
Assist. Prof. C. Can Aydıner	.....
Assist. Prof. Kadri Can Atlı	.....

DATE OF APPROVAL: 06.08.2013

To my lovely family.

ACKNOWLEDGEMENTS

I would like to express my deep gratitude to my master thesis advisor, Prof. Günay Anlaş for his endless support, kindness, encouragement and for his precious advice through this work. I have learned not only academic knowledge and skills from him, but also I found him as a real gentle-hearted one. I would also like to thank Assist. Prof. C. Can Aydıner for his insightful comments and mostly for helping me to understand basic concepts about digital image correlation. Special thanks to Assist. Prof. Kadri Can Atlı for his stimulating discussions and valuable comments on the topic, which were really helpful for me.

Thanks to my labmate, Behrouz for his help and fresh ideas and for his friendship, Kenan for his patience and for helping me to learn and conduct experiments properly, Ayça for her kindness and for her comments on DIC which became so helpful and time-saving at the beginning, Arun and Anıl for their supports.

During these two years, my friends made unforgettable and very happy moments for me which have colored my life. The best friends ever, Farhad, Samad, Farid, Paria, Shervin and Saloor, you mean a lot to me.

I would like to mention that this study would not have been possible without the support of my lovely family. Emotional encouragement and financial support from two angels of my life - My mom and dad -, made my way brighter and more joyful. Special thanks to Fariba and Reza, my sister and brother, who life would be meaningless without them.

And finally, I owe more than thanks to my lovely princess Baharak. It is so wonderful having a best friend and a very special person to love all wrapped in one. I feel so lucky, so thankful and so happy to have you in my life.

ABSTRACT

EVALUATION OF FRACTURE PARAMETERS OF NiTi SHAPE MEMORY ALLOY USING DIGITAL IMAGE CORRELATION

In this work, Digital Image Correlation (DIC) is used to investigate the effect of martensitic phase transformation on fracture behavior of NiTi shape memory alloy. To find out the effect of phase transformation from austenite to martensite on fracture behavior of NiTi shape memory alloy, fracture tests were conducted at both room temperature where phase transformation occurs and at the temperature that prevents this transformation. Displacement field that was obtained using DIC was used to estimate critical stress intensity factor. Results were compared to the ones obtained using linear elastic fracture mechanics (LEFM) and finite elements (FE). Before testing NiTi, the whole process was done using aluminum to validate the method. To characterize the NiTi, tensile tests at both temperatures were done and material properties were extracted. An experimental method based on DIC measurements was applied to estimate the size of martensitic phase zone and the result was compared to previous theoretical studies.

ÖZET

NiTi ŞEKİL HAFIZALI ALAŞIMIN KIRILMA PARAMETRELERİNİN DİJİTAL GÖRÜNTÜ KORELASYON KULLANILARAK DEĞERLENDİRİLMESİ

Şekil hafızalı alaşımlar (SMA) ve bu tip alaşımların en bilinen biçimi olan Nitinol (NiTi), sahip oldukları özgün nitelikler sayesinde önemli bir çalşıma alanı haline gelmişlerdir. Bu tez çalışmasında NiTi şekil hafızalı alaşımın kırılma davranışı incelenmiştir. Bu süperelastik NiTi alaşımlarda görülen iki katı faz arası martensitik faz dönüşümünün etkisini araştırmak amacıyla dijital görüntü korelasyonu yöntemi (DIC) kullanılmıştır. Östenit fazdan martenzit faza geçişin NiTi alaşımlarının kırılma davranışı üzerindeki etkisini görmek amacıyla hem faz dönüşümünü mümkün kılan oda sıcaklığında, hem de bu dönüşümü engelleyen sıcaklıklarda kırılma testleri gerçekleştirilmiştir. DIC yöntemiyle elde edilen yer değişim verileri kullanılarak kritik stres yoğunluğu faktörü hesaplanmış, doğrusal elastik kırılma mekaniği (LEFM) ve sonlu elemanlar (FE) analizi ile elde edilen sonuçlarla karşılaştırılmştır. NiTi parçalar test edilmeden önce, davranışı bilinen alüminyum parçalar test edilerek kullanılan yöntemin geçerliliği sınanmıştır. NiTi alaşımını karakterize etmek ve malzeme özelliklerini bulmak için her iki sıcaklıkta da çekme testleri yapılmıştır. DIC ölçümlerine dayanan deneysel bir yöntem uygulanarak martenzitik faz bölgesinin boyutu hesaplanmış, ve önceki teorik çalışmalarla karşılaştırılmıştır.

TABLE OF CONTENTS

LIST OF FIGURES

LIST OF TABLES

LIST OF SYMBOLS

2nsub+1	Subset size in x direction
2msub+1	Subset size in y direction
2nrtx+1	Coarse size in x direction
2nrty+1	Coarse size in y direction

a	Crack length
A_0	Body rotation
A_f	Austenite finish temperature
A_s	Austenite start temperature
B	Specimen thickness
E_A	Elastic modulus of austenite
E_M	Elastic modulus of martensite
$f(\frac{a}{W})$	Dimensionless geometry function
K	Stress intensity factor
K_c	Critical stress intensity factor
K_{Ic}	Critical stress intensity factor for mode I loadind
K_{II}	Stress intensity factor for mode II loadind
K_{III}	Stress intensity factor for mode III loadind
M_d	Martensite deformation temperature
M_f	Martensite finish temperature
M_s	Martensite start temperature
nacc	Final coarse step size
nconfigx	Step divider in x direction
nconfigy	Step divider in xy direction
ntrincx	Coarse step in x direction

ntrincy	Coarse step in y direction
P	Applied force
r_{max}	Greater radius of data filtering
r_{min}	Smaller radius of data filtering
T	T-stress
T_0	Reference temperature
u_0	Body translation
u_x	Displacement in x direction
u_y	Displacement in y direction
u_z	Displacement in z direction
W	Specimen width

ε_L	Transformation strain
μ	Material constant
ν	Poisson's ratio
σ	Applied stress
σ^{tr}	Transformation stress

LIST OF ACRONYMS/ABBREVIATIONS

ASTM	American Society for Testing and Material
BCC	Body centered cubic
CCD	Charge-coupled device
CMOD	Crack mouth opening displacement
COD	Crack opening displacement
CT	Compact tension
CTOD	Crack tip opening displacement
DIC	Digital image correlation
FE	Finite element
LEFM	Linear elastic fracture mechanics
NiTi	Nickel Titanium
RD	Rolling direction
SE	Superelasticity effect
SEM	Scanning electron microscopy
SIF	Stress intensity factor
SIM	Stress induced martensite
SMAs	Shape memory alloys
SME	Shape memory effect
TD	Transverse direction

1. INTRODUCTION

The reversibility of martensitic phase transformation was highlighted in 1962-1963 when efforts to find a proper material which could be used for heat shielding in a re-entry vehicle, resulted in discovering an intermetallic alloy of Nickel and Titanium (NiTi) accidently. Since William J. Buehler introduced NiTi shape memory alloys, which is also known as NITINOL (Nickel Titanium Naval Ordnance Laboratory), intense efforts have been started to discover mechanical properties of SMAs. It was observed that these materials not only have good mechanical properties but also are capable to show major atomic movement between two solid phases named "Austenite" and "Martensite". Unique features of SMAs are the source of special mechanical properties which are needed in some fields of application where traditional metals cannot provide expected features. Shape memory alloys are used in many areas such as aerospace and medical industries. Figure1.1 is a brief illustration for some applications of shape memory alloys. The capability of phase transformation gives extra ability to NiTi to deform more than traditional metals up to 12 % with the possibility to recover all strain to get back to the initial shape. Shape memory alloys show two important properties named "superelasticity"(SE) and "shape memory effect"(SME). Phase transformation between the phases occurs when enough energy is induced to the material in the form of changes in either stress or temperature [35].

1.1. Superelasticity

Superelasticity is the ability to recover from stress-induced deformation after unloading. Above austenite finish temperature A_f, material is in the austenite phase. If austenite is loaded without change in temperature, twinned martensite will appear at the end of elastic deformation. During the forward phase transformation very large strain can be achieved with small increase in stress. It should be mentioned that the

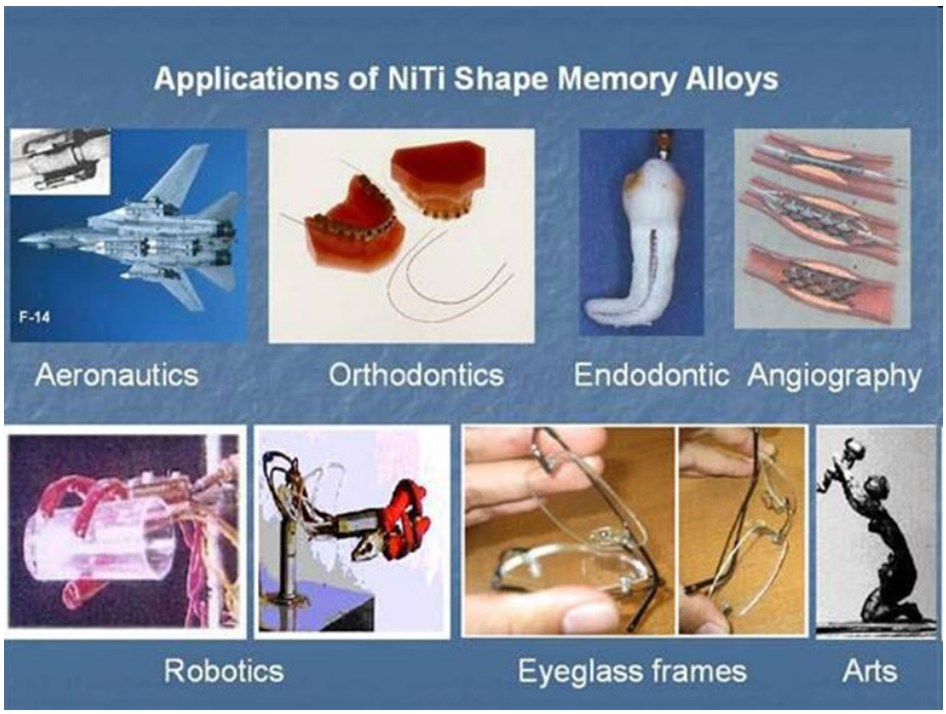

Figure 1.1. Application fields of shape memory alloys [10].

new elastic modulus in some papers is considered as elastic modulus of the martensite E_M but in the works by some others it is mentioned that the slope of the elastic part of fully transformed material is affected by some factors such as untransformed austenite grains, reorientation of martensite variables and etc. They predict a much higher elastic modulus for martensite sometimes even higher than elastic modulus of austenite [25,28,37,54]. With removal of the applied load, fully transformed martensite will regain elastic strain first and will start to get back to the parent austenite phase. Large deformation caused by applied load will be fully recovered. Figure 1.2 illustrates the stress temperature diagram for shape memory alloys. Forward and reverse transformation is shown at temperatures between M_d and A_f. The four temperatures which are shown in the Figure 1.2 are characteristic temperatures of a shape memory alloy [20]. If the material stays at temperature below the martensite finish temperature M_f, martensite will be stable and phase transformation will not occur even if subjected

to stress. Phase transformation does not happen either if the temperature reaches M_d (martensitic deformation temperature). The temperature range which supplies phase transformation under applied stress lies between these two temperatures A_f and M_d.

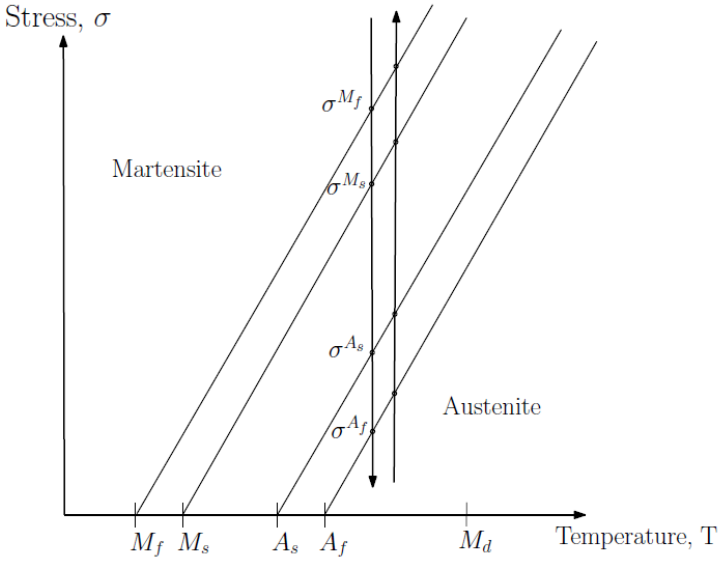

Figure 1.2. Stress-temperature diagram and superelastic effect [20].

1.2. Shape memory effect

Figure 1.3 illustrates stress-temperature curves for a shape memory alloy when the material is subjected to only temperature changes under constant stress [20]. It can be seen from Figure 1.3 that austenite transforms into twinned martensite when temperature reaches martensite start temperature M_s during cooling process. The transformation continues until it finishes at martensite finish temperature M_f where material is fully twinned martensite. Loading twinned martensite at temperature below M_f will cause detwinning with large strain associated. Detwinning process is the dominant deformation mechanism in shape memory alloys which can be compared to plastic deformation produced by slip dislocation mechanism in normal metals. At austenite

start temperature A_s, twinned martensite phase becomes unstable and starts to form austenite phase and continues until material becomes fully austenite at austenite finish temperature A_f.

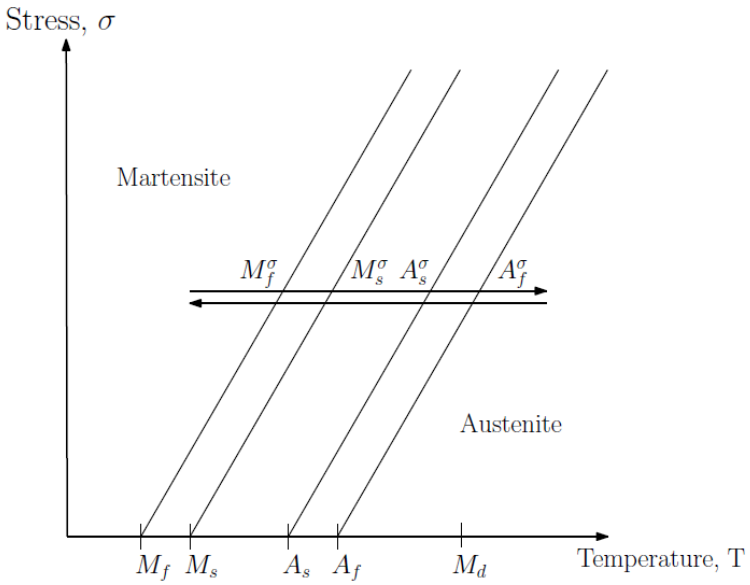

Figure 1.3. Interaction between austenite and martensite at a constant stress and changing temperature [20].

2. PHASE TRANSFORMATION AND ITS EFFECT ON FRACTURE PARAMETERS OF SHAPE MEMORY ALLOYS

2.1. Introduction

Less information about fracture properties of SMAs compared to other mechanical properties has convinced researchers to go through understanding the fracture behavior of SMAs by means of different models and methods. In this chapter, a summary of what has been done before in order to explore the martensitic transformation and its effect on fracture behavior of shape memory alloys is covered.

2.2. Previous studies on shape memory alloys

In 1980, Miyazaki, *et al.* investigated crack initiation and propagation in Cu-Al-Ni shape memory alloys and they came up with results which proved that the initiation and propagation of crack occurs along grain boundaries where large elastic anisotropy causes the stresses which are responsible for crack initiation and propagation. They stated that the propagation path of crack can easily deviate from grain boundaries when the specimens are in martensitic state because the stress concentration at the crack tip becomes more critical than the stresses at the grain boundary where variety of deformation mechanisms at the boundaries help to release these stresses. They also concluded that the main reason of different behavior of Cu-Al-Ni and NiTi alloys in the amount of elongation prior to failure and brittleness and ductility, although both are BCC structured alloys, is due to the grain size [32].

In 1994, Stam, *et al.* discussed about the effect of reversibility of stress-induced martensite transformation on toughness of shape memory alloys. Finite element analysis in their work showed that reversibility of transformation during crack propagation can significantly decrease total amount of toughness increase [41].

The effect of stress induced martensitic transformation on stress intensity factor of a thin plate (plane stress condition) under mode I loading was investigated by Birman in 1997. The size of plastic deformation zone in front of the crack tip was evaluated in his work where he modified the well-known relations used to calculate the plastic radius in common engineering metals. He stated that the size of plastic zone increases as a result of the phase transformation around the crack tip. Similar conclusion was obtained at the end for stress intensity factor. The differences were found to be small and Birman suggested that austenitic stress intensity factor could be used as the material general SIF [2].

Yi and Gao, in 2000, did an analytical study on shape memory alloys using Eshelby inclusion model and weight function method. They used this theoretical analysis without considering volume strain and reverse transformation. Their work based on linear elastic fracture mechanic theory for a semi-infinite pate in plane-strain condition and came up with a different conclusion at the end. According to their work, stress intensity factor decreases as a result of martensitic phase transformation and consequently toughness increases. They also measured size and shape of transformation zone at the crack tip. Temperature dependency of the toughening process was highlighted in their work such that increasing the temperature results in decreasing the toughening process [52].

One year later, Yi, *et al.* used similar methods for mixed mode loading. They focused on energy release rate and load phase angle. The results showed nonsymmetrical transformation zone which depends on phase angle of applied remote load. Other con-

clusion proved their previous work that martensitic transformation increases material toughness [53].

Gall, *et al.* in 2000, investigated fracture mechanisms in NiTi shape memory alloys. They looked at signal crystal NiTi and polycrystalline NiTi with different precipitate sizes to find the dominant fracture mechanisms which leads to failure. [15].

Lopez, in 2001, investigated mechanical behavior of Ti-rich NiTi experimentally. Looking at the surfaces of fracture failure he found that there is an unexpected plasticity and work hardening in material's behavior which cannot be due to dislocation slip systems. He concluded that this kind of behavior can be explained by reverse transformation from martensite to austenite at highly stressed martensitic zone such as the crack tip [26].

Initiation of microcrack was investigated in a work by Lu, *et al.* in 2001. They conducted in-situ tensile tests for CuNiAl shape memory alloy and found that microcracks initiated in the stress induced martensitic and parent phase around the crack tip right after the formation of martensite variants. They came up with the same idea that reverse transformation can occur upon loading or crack propagation. [27].

Yan, *et al.* in 2002, investigated the effect of volume contraction caused by phase transformation and reverse transformation on the fracture parameters of NiTi shape memory alloys. Their results admitted the existence of partial reverse transformation which occurs in the wake of the advancing crack that reduces the toughness of the material, but they found that this phenomenon has a small and negligible effect. Most important conclusion of their work was the great amount of increase in stress intensity due to less than half percent transformation induced volume contraction about 12% for -0.39% volume strain. These results are in contrast with the previous works on zirconia which shows positive volume strain amount and toughening effect [50].

Yan, *et al.* in 2002, established a constitutive model for shape memory alloys which considered plasticity and transformation in the model. Using this model they studied the effects of plasticity in reverse transformation both numerically and analytically. Martensitic volume fraction was the internal variable of their model. They determined the distribution of martensitic volume fraction and equivalent plastic strain around crack tip [51].

In 2005, Chen, *et al.* conducted a series of tensile tests with thin NiTi shape memory alloy tension specimens, using in-situ observation to track fracture behavior (SEM) and found out that specimen's thickness, different notch shapes and different notch acuities impose different effects on crack initiation and propagation. They stated that crack propagates along maximum normal stress after initiating at the root of the notch. They believed that martensitic transformation has toughening effect due to extra plasticity which is caused by the martensitic transformation and blunts crack tip but also they stated that more elaborate work should be done in order to prove it [3].

Wang, in 2006, did a finite element analysis to determine the effect of notch geometry on fracture behavior of shape memory alloys using CT specimen in plane stress condition. Changing the acuity of the notch from blunt one to crack, he investigated three characteristic loads and stress and strain distribution in four regions divided by those loads. The characteristic loads were starting and finishing loads of martensite and the beginning load of the plasticity. The most important result he came up with, was that with increasing the acuity of the notch, stress and strain and their growth rate at the crack tip increase and full martensite zone is produced with lower amount of induced stress. Also he claimed that the more acute crack would result in the less fracture process zone and more stable crack growth [44].

More research on the effect of plasticity continued by Yan and his coworkers in 2006, where they theoretically probed the effect of plasticity on transformation using

a constitutive model which combines both transformation and plasticity [51].

A phenomenological analysis using finite elements was carried out by Wang in 2007. Using the similarity between stress-induced martensitic transformation zone in shape memory alloys and the plastically deformed zone in a metal, he implemented an elastic-plastic constitutive model to a CT specimen under plane stress condition. He referred to a model developed by Auricchio, *et al.* and modified by Yan, *et al.* that considers macroscopic deformation due to transformation, combined with von Misses' isotropic hardening theory. According to this model, transformation is the same as in plasticity and both are of von Misses type. He suggested using equivalent plastic strain instead of martensitic volume fraction in the case of loading. He ignored the elastic mismatch between austenite and martensite and used same elastic modulus and Poisson's ratio for both. He stated that stress and strain increase upon loading and four different features appear due to plastic deformation and transformation zones. He claimed that crack initiation occurs in plastically deformed fully transformed martensite, and the martensitic transformation at the crack tip improves the toughness of the material [46].

The same year, in another work, Wang investigated the stress and strain distribution around the crack tip in both NiTi shape memory alloy and a fully transformed martensite NiTi without transformation using finite elements to give a better understanding to the effect of martensitic transformation on fracture parameters of shape memory alloys. He simulated a NiTi compact tensile specimen (CT) with a notch and in plane stress condition. He used a constitutive model based on the Misses yield theory which can describe both martensitic transformation and the plastic strain in fully transformed martensite. He found that the load needed for plastic deformation in the fully transformed martensitic zone increases by the transformation mechanism and maximum normal stress which derives the crack propagation decreases. All these prevent the crack from nucleation and propagation and increase the toughness of ma-

terial [44].

Gulerthan, *et al.* in 2007, investigated the effect of martensitic transformation on fracture properties of NiTi shape memory alloys. They used a miniature CT specimen under plane stress condition. LEFM was used to obtain the critical stress intensity factor. Several fatigue precracked CT specimens were tested under displacement control mode at a rate of 0.05 mm/min. They calculated critical stress intensity factors using LEFM and found that for a certain ratio of a/W, they did not differ too much. They suggested that for this a/W ratio, the mean of all calculated critical stress intensity factors could be considered as a material property. They observed considerable stable crack growth prior to failure in their specimen. At the end they calculated the size of transformation zone using relations of LEFM [16].

Experimental investigations on fracture behavior of shape memory alloys using CT specimens were continued by Wang, *et al.* and pre-cracked specimens were used to determine fracture toughness. Probing the fracture surface they found out that the fracture process was dominated by cleavage fracture. They compared their results with the ones obtained from finite elements for both pre-cracked and without pre-crack specimens. They used a micromechanical model for pseudoelasticity that considers elastic mismatch between austenite and martensite. Ni-rich NiTi compact tension specimen under plane strain condition was used and the fracture toughness was calculated using LEFM relations. SEM observation showed that the fracture surface at the final fracture zone is smoother than that at the fatigue pre-crack zone indicating more brittle behavior at fracture due to higher crack propagation velocity [47].

Yuval Freed, Leslie Banks-Sills, in 2007, numerically investigated the effect of martensitic transformation on toughening of shape memory alloys under plane strain condition and mode I loading. A cohesive zone model was implemented with independent parameters: cohesive energy G_c, cohesive strength t_0, and the critical separation

length d_c. They investigated the relations between these parameters and the crack growth resistance. The shape and size of the initial transformation zone evaluated using LEFM and assuming small scale transformation zone revealed that the shape and size of the transformation zone and the shape and size of the plastic zone in plastically deformed materials coincide. They also explored the effect of the Young's moduli ratio on crack resistance, and the contribution of reverse transformation. It was found that the moduli mismatch increased the steady-state stress intensity factor. Because of the ease of implementation to numerical studies, they chose a phenomenological model introduced by Panoskaltsis, *et al.* (2004), which is a combination between generalized plasticity theory and the theory of continuum damage mechanics which is able to describe different material moduli for austenite and martensite. Similar to pervious works they came up with the conclusion that reverse transformation significantly decreases the toughening effect of martensitic transformation at the crack tip by decreasing the amount of energy dissipation the wake of the crack tip and consequently by decreasing the load needed for crack propagation [14].

In 2007, Daly, *et al.* investigated the transformation zone shape and size for NiTi shape memory alloy edge-cracked specimen in plane stress condition. They used DIC (Digital Image Correlation) method to relate stress-induced strain field to the boundary phase initiation and propagation. Average plane strain toughness for thin sheet NiTi was calculated for the first time using DIC. Specimen was cut in RD and displacement control tension test was conducted and strain was measured using DIC. Several tests with different a/W ratio were carried out and for each, stress intensity factor measured using linear elastic fracture mechanic relations. [7].

Xiong, *et al.* in 2007, investigated the effect of martensitic transformation on fracture behavior of Ni-Mn-Ga shape memory alloy and compared them with those of NiTi and Cu-Al-Ni. In their theoretical analysis based on the elastic-plastic fracture mechanics, they found that stress distribution around the crack tip is affected by

stress induced martensitic transformation which increases the stress intensity factor at the crack tip. The normalized stress induced martensitic stress intensity factor was calculated as a function of temperature and showed drastic increase as temperature approached to M_s [49].

Robertson, *et al.* in 2007, conducted series of low cycle fatigue experiments on CT specimen under mode I loading and plane stress condition. They used X-ray synchrotron to measure in-situ strain field in both macroscopic and microscopic level. The specimen which they used showed 6-8% global superelastic recovery strain where using a grain by grain resolution local strain field measurement for individual austenite grains revealed strain about 1.5%. This proves that large amount of macroscopic deformation in shape memory alloys is due to the martensitic transformation and plastic deformation of fully transformed martensite very close to the crack tip [38].

Creuziger, *et al.* in 2008, looked at the effect of different crystallographic orientation in fracture behavior of a single crystal shape memory alloys. During the test they used in-situ optical technic to track martensitic transformation. They found that for notch tip samples, transformation structures in the [100] sample initiated at the sides of the notch tip and crack propagation was stable. In [111] notched samples, transformation occurs directly ahead of the notch and unstable crack propagation was observed [6].

In 2008, Lexcellent, *et al.* used a model to determine size and shape of the transformation zone. Their model included the asymmetry between tension and compression and introduced martensitic volume fraction as an internal variable. An average of applied stress intensity factor and a governing stress intensity factor near the crack tip were used to determine the shape and size of the transformation region. Their result met finite element analysis results [23].

Notch geometry came to the investigation again by Wang, *et al.* in 2008. Detailed study on the effect of notch type and size was carried on. Five kinds of notches were studied: semicircular notches with two sizes, V type notches with two sizes and a crack notch. Finite element analysis based on pseudoelastic constitutive model that considers permanent plastic deformation was used and stress, transformation strain and plastic strain were measured. Interestingly no distinct stress plateaus were observed in the case of specimens with larger semi-circular notch, with V type notches and with crack notch. Plastic deformation was observed right before the final fracture. Increasing the notch acuity concentrated the transformation and plastic deformation zone at the crack tip and reduced the stress needed to initiate transformation. SEM observation showed that the fracture mechanisms differ by notch type and size [48].

Gullertan, *et al.* in 2008, did experiments using modified miniature CT specimens made of two kinds of NiTi shape memory alloy with different composition. Their work included three states of material. One with pseudoelastic behavior, one in martensitic state and one in austenitic state without transformation. Tension tests were performed and stress-strain behavior was obtained for each case. To perform a test in the austenite state and without transformation, they had to find the temperature above which transformation dose not happen. To find M_d they conducted several tension tests below and above the room temperature. Precracked CT specimens with different a/W ratios were used to perform fracture tests according to standard ASTM E399-90. LEFM relation was used to calculate the stress intensity factor for each case. Series of fracture tests for each state of material were done and an average stress intensity factor was chosen as K_{IC}. In addition an in-situ tension test was performed using SEM to observe the crack tip of each case subjected to different loads. In the case of martensitic state and pseudoelastic one no crack blunting was observed despite of deviation from linearity prior to unset of microcrack growth. Interestingly they found a higher resistance to crack extension compared to pseudoelastic one and martensitic one. Very important result of their work is the fact that plane strain condition does not prevent martensitic

phase transformation at the center of the crack tip [17].

Falvo, *et al.* in 2008, investigated the evolution of stress-induced martensitic transformation in front of a crack tip using finite element analysis. Single edge-cracked specimens were used. Transformation zone size was calculated using theory of plasticity and the effect of temperature on stress-strain distribution and on the martensitic transformation zone size for NiTi shape memory alloys was explored numerically. They proved the assumption from previous works which states that the distribution of martensitic fraction can be obtained by equivalent plastic strain at the crack tip. Also they stated that an increase in temperature causes a drastic decrease in the size of transformation zone at the beginning but the size of it at the end does not change [13].

Taillebot, *et al.* in 2009, investigated the transformation zone around the crack tip in mode I , mode II and mode III loading using a new approach which combines the asymmetry between tension and compression. Like most models their model considers the martensitic volume fraction as internal variable. They predicted transformation zone shape and size for both plane stress and plane strain and found out that the results are in very good agreement with elasto-plasticity results from LEFM. They also performed two kinds of experiments. One was the tension test with displacement control procedure for NiTi rectangular sample in plane strain condition and thermal flow on one surface was observed using infrared camera. Same tests were done for closely plane stress condition. Results came from interpretation of the temperature fields before and during the crack initiation and propagation shows that the average temperature of the specimen remains stable while the local temperature at the crack tip differs significantly [42].

In a work done by Maletta and Furgiuele, in 2010, analytical and finite element analyses were done for shape memory alloys in order to find the evolution of stress induced martensitic transformation and the stress distribution near the crack tip for

plane stress condition. The effect of different thermomechanical parameters such as transformation stress and strain and elastic moduli on crack tip transformation behavior was investigated. They implemented Irwin's modified relation of the LEFM, combined with relations used for estimation of crack tip field in bilinear materials. They validated their model comparing the results with those came from numerical analyses by commercial finite element package. They found that the transformation region increases when transformation strain increases and the transformation stress decreases. They also stated that the transformation extent is so sensitive to testing temperature and the Young's moduli where these parameters affect the stress distribution near the crack tip. They neglected the effect of plastic deformation in fully martensitic region due to very small plastic zone compared to transformation zone in their model [30].

Later on, Maletta and Young, modified their proposed analytic model to include the plane strain condition by accounting the stress triaxiality. They added another parameter, the transformation constraint factor, which is based on the plastic constraint factor of elasto-plastic materials to include the effect of stress triaxiality. They validated this new model by comparing the results to those from synchrotron x-ray microdiffraction observations. They implemented this model to evaluate the boundaries of transformation zone at the crack tip of miniature CT specimen. As expected, transformation zone in plane stress was much greater than that in plane strain due to stress triaxiality which prevent crack from propagating. They stated that transformation zone radius which comes from experiment using X-rey diffraction mapping of the CT specimen, remains between those martensitic radii calculated from their theoretical model for plane strain and plane stress. Results for different a/W ratios showed more rapid decrease for austenite zone radius [28].

The other modification which Maletta did to this model was extracting the same analytical model without the assumption of constant stress during the transformation

process. They found a considerable variation of the transformation region but a small change in stress intensity factor when the slope of the stress-strain curve during phase transformation increase [29].

Malleta, *et al.* in 2011, defined two different stress intensity factors based on LEFM for both transformed (full martensite) and untransformed (austenite) regions to describe stress distribution. Results were compared to those obtained using linear elastic fracture mechanics approach. They found stress intensity factor obtained by their model greater for austenite but smaller for martensite region compared to the results from LEFM. They validated their proposed method by comparing the fracture process zone in SMAs with that of elastic-plastic material. They interpreted this as the result of Young's moduli differences between austenite and martensite and concluded that stress induced martensitic transformation has toughening effect because fracture always occurs in the fully martensite region [31].

Lexcellent, *et al.* in 2011, analytically predicted the phase transformation zone around the crack tip using a model that includes asymmetry between tension and compression including stress directional effect for transformation effect. They estimated the transformation zone for mixed mode loading condition as well as mode I, mode II and mode III loading using a general solution. These calculations were done for both plane stress and plane strain. Their phenomenological analysis was built on modifications on linear elastic fracture mechanics based models presented by Raniecki and Lexcellent, 1998, Bouvet, *et al.*, 2004, and Laydi and Lexcellent, 2010. They found that asymmetry between tension and compression is more important for plane stress than for plane strain especially for mode I loading [21].

To continue their efforts on characterization of shape memory alloys, Lexcellent, *et al.* examined plasticity theory-inspired model's prediction of shape and size of the transformation zone. They admitted the fact that the effect of asymmetry in 3D model

is more obvious for plane stress rather than for plane strain [22].

In 2012, Jiang Shu-yong, experimentally tried to understand the fracture behavior and the microstructure of the as-cast NiTi SMA which was not heat treated nor plastically worked. They conducted series of tensile and compression tests to obtain the properties of the material under displacement control. They reported different fracture mechanisms for different test temperatures. Tensile tests using as-cast NiTi SMA showed ductile fracture behavior at high temperature(750 °C) where the dominant fracture mechanism at room temperature and lower one (−100 °C), was cleavage fracture. They also found that in the case of compressive tests at (−100 °C), shear fracture with the compressive axis about (40 °C) was responsible for materials fracture behavior [19].

In 2011, Kwangjun Ehu, *et al.* made in-situ observation to describe fracture parameters of ferromagnetic Ni-Mn-Ga-Fe shape memory alloy. Microfracture was observed by SEM while loading and results showed that γ particles inside the β grain acted as blocking sites and make crack more difficult to propagate. Crack blunting and bridging were blocked as well and all these mechanisms led to stable crack growth. Consequently improved fracture toughness was reported. They also used linear elastic fracture mechanic assumption and calculated stress intensity factor [12].

Literature shows that thermomechanical properties of these alloys and martensitic phase transformation-associated effects like shape memory effect and pseudoelasticity have been investigated well since shape memory alloys have been introduced but compared to these subjects, relatively less portion of studies was devoted to underestanding mechanical and functional properties of SMAs. What makes such studies difficult is that these kinds of material react when they are subjected to either thermal or mechanical changes because the martensitic phase transformation and mechanical deformation act with together. In addition, local concentration of martensitic transformation in a

body which is subjected to deformation-imposing condition causes local deformation as well. The complexity of mechanical behavior has become a convincing motivation while SMAs are in the way of finding their place in industry. In the case of mechanical properties researches mostly go to evaluating elastic modulus of material, exploring fatigue behavior of material [38] and formation of martensitic phase under tensile loads but fracture behavior of these material needs more attention.

3. MOTIVATION

Lots of works in the field of frecture mechanics were done to understand the formation of local martensitic transformation at crack tip on initiation and propagation of micro and macro-cracks [27, 32]. Also efforts included characterization of dominant fracture mechanisms in such materials [15]. Several kinds of analysis such as scanning electron microscopy (SEM), X-ray microdiffraction analysis, digital image correlation (DIC) and infrared thermography were implemented [12, 17]. Some analytical models were established to characterize fracture behavior of shape memory alloys. [23, 30, 42]. The effect of stress-induced martensitic transformation in single loading mode and mixed-mode loading on the fracture parameters was investigated in the works by some other researchers. Some admit that stress-induced martensitic transformation (SIF), increases material's resistance against initiation and propagation of crack and increases fracture toughness [2,3,53] while some others came up with opposite conclusion [17,52]. The effect of SIF on shape and size of the plastic and transformation zone at the crack tip is one of the most noticed subjects in fracture mechanics of shape memory alloys [2]. Some researches were concentrated on the effect of reverse transformation that happens in the wake during loading [26, 41]. They all claim that this reverse transformation affects the amount of increase in toughness adversely [14]. Finite element analysis was implemented to simulate behavior of the material [13, 30, 47]. Different constitutive models such as Auricchio's model were used in FE packages [46].

Although some researchers conducted experimental examinations to characterize fracture behavior of shape memory alloys, shortage of reliable experimental results especially in calculation of stress intensity factor and martensitic transformation zone size is evident. Linear elastic fracture mechanics relations were the base of experimental calculation of stress intensity factor in most works [16, 45, 47]. Despite good information caming from linear elastic fracture mechanics predictions, because of many initial

assumptions and limitations in the theory of LEFM, standard procedures required to calculate fracture parameters cannot be satisfied completely. Because of these kinds of limitations it seems that extra experimental work is needed.

One of the best choices is non-contact in-situ observation methods. In a work by Daly [7], digital image correlation was used in full-scale measurement of localized strain in macroscopic scale during transformation. She evaluated a Kc value for plane stress using series of tensile tests with edge cracked thin sheet NiTi specimens. Like most other researchers, she used LEFM relations to obtain an average K. In the present work, the asymptotic relation which relates displacement field to fracture parameters like mode I and mode II stress intensity factors as well as T-stress is used instead of well-known stress intensity factor's relation in terms of load. This thesis uses DIC method to obtain full displacement and strain fields and the stress intensity factor based on linear elastic fracture mechanics assumptions.

4. PROBLEM STATEMENT

An edge cracked CT specimen is loaded and displacement is measured using DIC. The measured displacement field is fitted to the relation shown below in order to evaluate fracture parameters such as K_I and K_{II}.

$$\begin{aligned} u_y = \frac{K_I}{2\mu}\left(\frac{r}{2\pi}\right)^{\frac{1}{2}} \sin\frac{\theta}{2}\left(\frac{3-\nu}{1+\nu} - \cos\theta\right) - \frac{T\nu}{2\mu\,(1+\nu)} r\sin\theta + \\ \frac{K_{II}}{4\mu}\left(\frac{r}{2\pi}\right)^{\frac{1}{2}} \left(\frac{5\nu-3}{1+\nu}\cos\frac{\theta}{2} - \cos\frac{3\theta}{2}\right) + A_1 r\cos\theta + u_{0y} \end{aligned} \tag{4.1}$$

The values obtained are compared to those from traditional fracture test using fracture relations for an edge cracked plate and finite elements to find out whether all results fit together or a modification is needed in the relation in order to account for the complex behavior of NiTi shape memory alloy.

$$K_Q = \frac{P_Q}{B\sqrt{W}} f\left(\frac{a}{W}\right) \tag{4.2}$$

where

$$f\left(\frac{a}{W}\right) = \frac{\left(2+\frac{a}{W}\right)}{\left(1-\frac{a}{W}\right)^{\frac{3}{2}}}\left[0.886 + 4.64\frac{a}{W} - 13.32\left(\frac{a}{W}\right)^2 + 14.72\left(\frac{a}{W}\right)^3 - 5.6\left(\frac{a}{W}\right)^4\right] \tag{4.3}$$

This thesis also aims to evaluate the radii of different phases using strain field which is obtained from digital image correlation. This could be a challenging comparison tool between theoretical evaluation of the size of the transformation zone and finite

elements using results from other experimental tools mentioned earlier in this chapter.

Another aim is to explore the effect of martensitic phase transformation on fracture parameters of NiTi shape memory alloy when this transformation is prevented from occurring under the same loading condition. To do this, a specimen with the same size and form as the one tested at room temperature is loaded above the M_d temperature. A practical procedure was introduced in the work by Gullerthan, *et al.* in 2009 [17] to estimate martensitic deformation temperature. Gullerthan, *et al.* measured irreversible strain after loading/unloading the specimen at different temperatures. They observed that after a specific temperature, which they named as M_d, the residual strain after full unloading does not change. The experimental results in their work are shown in Figure 4.1.

All experiments are performed both at room temperature and high temperature (any temperature above M_d) to see differences between the two states which will demonstrate the effect of martensitic phase transformation on fracture parameters of NiTi shape memory alloys. Three methods will be used to calculate the fracture parameters in each case. The first method uses traditional ASTM tests along with fracture mechanics relations to find critical stress intensity factor for tested specimens. The second method uses the parameters calculated from the fitted displacement data by using Eq 4.1. Finally finite element analysis is used.

4.1. Conclusions

Shortage of experimental data for NiTi shape memory alloys brings many doubts to conclusion because if the results mentioned above do not confirm eachother, it is not possible to recognize which method gives more reliable results. Therefore it is better to do exactly same procedure on a well-known traditional material to validate that if DIC measurements are healthy or if true modeling in fnite element analysis is in progress.

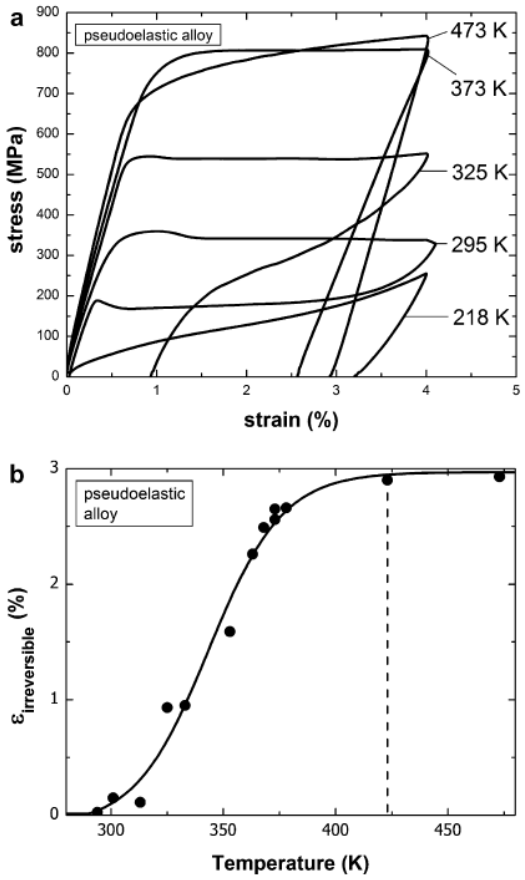

Figure 4.1. The effect of temperature on stress-strain behavior of pseudoelastic NiTi SMA (a) irreversible strain-temperature curve (b) dashed line denotes M_d [17].

If results for such material stand in a good accordance then we will apply the process to NiTi shape memory alloy with confdence. Validation process will be explained in Chapter 7.

4.2. Outline

This thesis starts with material characterization of NiTi shape memory alloy specimens used in experiments. The procedure, setup and results of tensile tests in

both rolling and transverse directions are presented in Chapter 5; optical micrography from the surface of the material is explained and the grain size is estimated as 15-20 Micron.

In Chapter 6, a brief introduction is given and major concepts of digital image correlation are explained using some examples. The schematics of DIC setup and the specification of a good pattern are illustrated.

The procedure of calculating critical stress intensity factor is given for aluminum in Chapter 7. Critical stress intensity factor is calculated at the moment of fracture using full-field displacement obtained from DIC is compared to those calculated from traditional linear elastic fracture test (ASTM E399-09) and from finite element analysis to validate the whole procedure.

Experimental investigation of fracture of NiTi using the validated method starts in Chapter 8. All experiments in this chapter are done at room temperature at which martensitic phase transformation occurs fully or partially. Two types of lenses with different fields of view are used to capture images. Finite elements is used to model the actual specimen through UMAT of ABAQUS.

In Chapter 9 the same fracture experiments are done for NiTi at a temperature above M_d in order to prevent martensitic phase transformation. To obtain mechanical properties of NiTi at high temperature, tensile tests are conducted, and the results are discussed. Finite elements at this temperature is explained and the results are shown.

Martensitic transformation zone based on the DIC full-field displacement measurements are estimated in the final Chapter. Two other theories, one from literature and the other from the simple assumption of similarity between transformed phase in NiTi SMA and plastic zone size in metals, are employed.

5. CHARACTERIZATION OF MATERIAL(MECHANICAL PROPERTIES)

Material is flat annealed with a pickled surface and was produced according to ASTM F 2063-05. Ni based shape memory alloy contains 55.99% Ni, less than 0.05% C, less than 0.05% O and less than 0.20% components like Co, Cr, Cu, Fe, Mn, Mo, Nb, Si, W. Austenite finish temperature for the material is reported as 16.1 °C by the manufacturer (Johnson Matthey). All specimens used in experiments were cut from 1.00 mm ± 0.1 mm thick and 95 mm wide and 457 mm long superelastic NiTi shape memory alloy plate. The original parent NiTi sheet is shown in Figure 5.1.

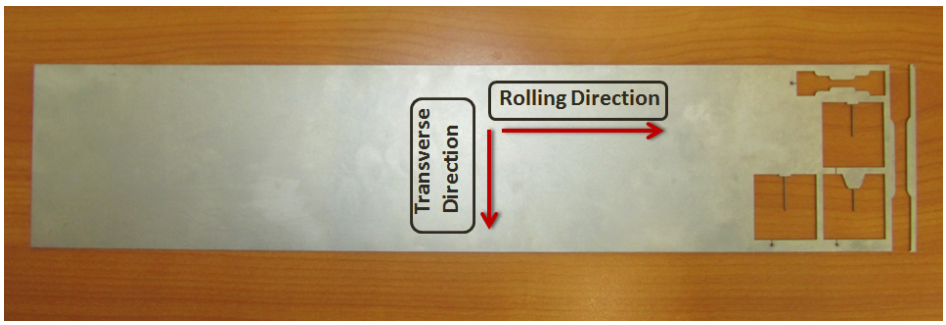

Figure 5.1. Parent sheet of NiTi and illustration of rolling and transverse directions on it.

Tension test is needed to characterize material's mechanical behavior. Tensile tests were performed in both RD and TD directions and stress-strain curves with upper and lower stress plateaus as well as transformation strain and total elongation were obtained. Test procedure was according to ASTM E8/E8M - 11 (Standard Test Methods for Tension Testing of Metallic Materials) as the main tensile test guideline for metallic materials and ASTM F2516 - 07 (Standard Test Method for Tension Testing of

Nickel-Titanium Superelastic Materials) which gives extra definitions and parameters uniquely for shape memory alloys. Two configurations were used for the test to meet the capacities and limits of existing tensile test machines.

Figure 5.2 and 5.3, show detailed view of the specimens used for tension tests in transverse directions (TD) and rolling direction (RD) respectively.

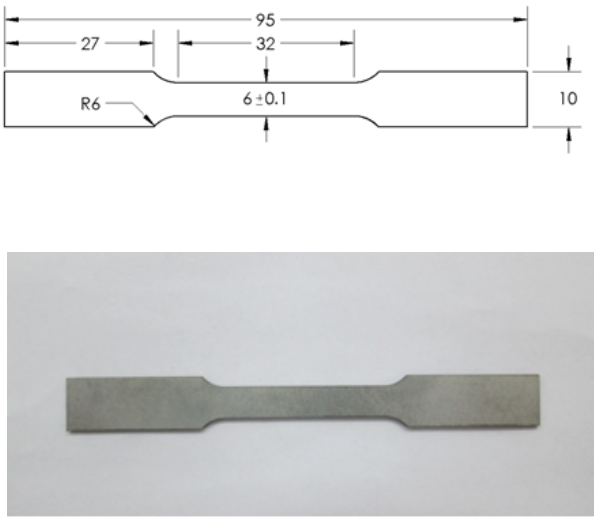

Figure 5.2. The specification of dog-bone test specimen cut in transverse direction.

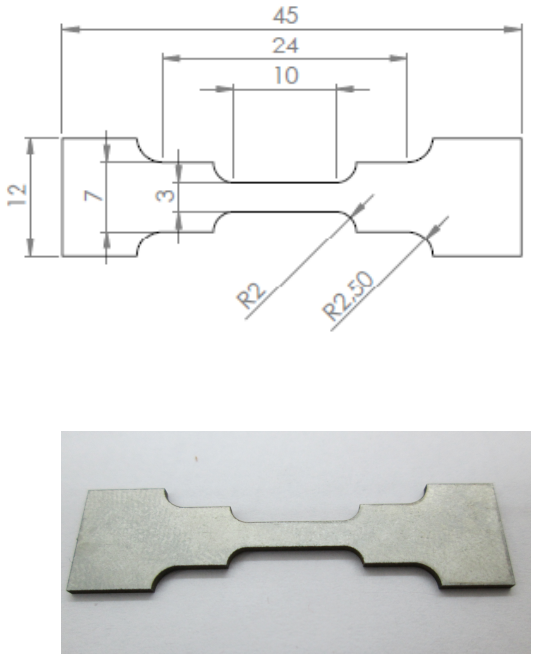

Figure 5.3. The specification of dog-bone test specimen for rolling direction.

As it can be seen, because the material is highly brittle, ASTM standard suggests a large fillet radius at the end of the gauge length.

5.1. Tensile test procedure

Tensile test consists of two stages. At the first step, the specimen is loaded up to 6% strain under displacement control mode with a rate of 0.5 mm/min and then is unloaded until stress level goes down to 7 MPa to obtain the hysteresis loop. At the second step the specimen is loaded at 5 mm/min displacement rate until failure. The test procedure is shown below schematically (ASTM F2516 - 07) [17]. Strain is measured using proper strain gages attached to the specimen such that it remains inside the gauge length of the specimen [18].

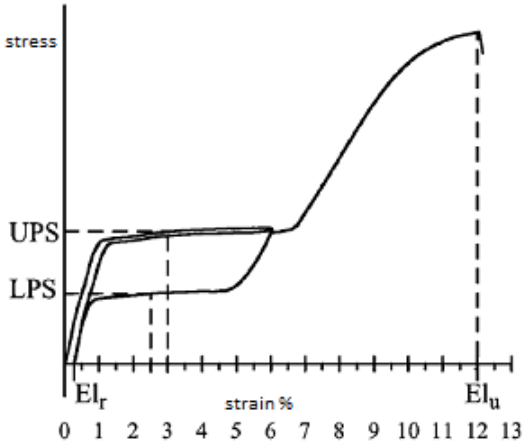

Figure 5.4. Schematic illustration of tension test procedure for pseudoelastic NiTi.

The reason that ASTM suggests relatively low rate of pulling at the first cycle, is because of the changes in material's temperature due to exothermal characteristic of forward martensitic transformation [21]. Material's temperature can vary in a long range at the moment of forward and reverse phase transformation. As it has been shown in some works the temperature which was measured by infrared camera, can vary on the order of 40 °C in edge-cracked specimens [21]. Low loading rate can ensure a quasi-static test condition which eliminates the effect of temperature on measured parameters of the material. Upper and lower plateau strength are measured at 3% and 2.5% strain respectively as shown in Figure 5.4. Residual elongation El_r is defined as the difference between the strain at 7 MPa during loading and that during unloading steps and total uniform elongation El_u is the amount of elongation at maximum stress right before necking or fracture [18].

5.2. Tension test for NiTi in Rolling Direction

5.2.1. Test setup

Figure 5.5 shows the setup used for tension tests in RD according to the procedure outlined in the previous section.

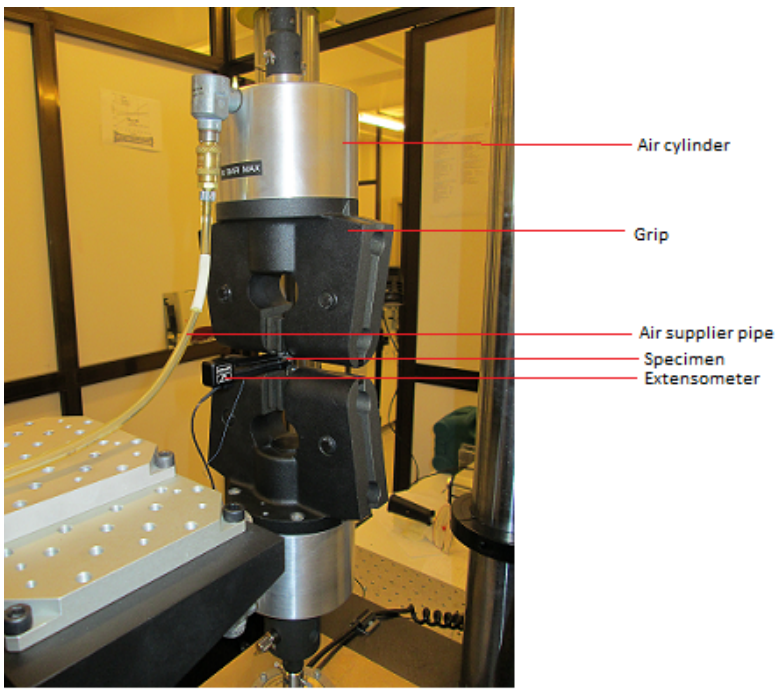

Figure 5.5. Tension test setup for RD direction.

To be able to hold specimens at higher loads, end tabs made of Aluminum 7075-T 651 are glued to the specimen using epoxy glue (Araldite 2000) and strong pneumatic grips were used to guarantee that slippage does not occur. Figure 5.6 shows the specimen with end tabs.

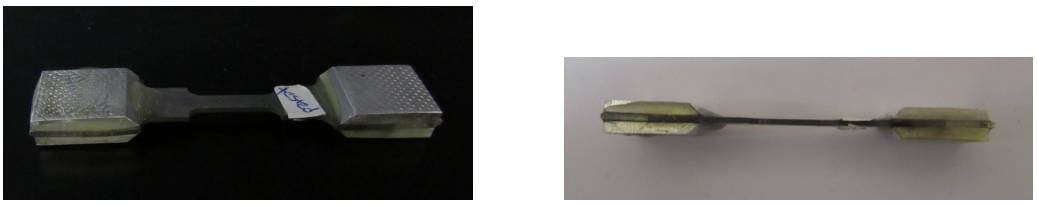

Figure 5.6. Small NiTi specimen with end tabs to prevent slippage.

2 KN INSTRON screw-driven microtester was used to load the specimen and strain amounts were obtained using strain gages. Strain can also be obtained from the testing machine's cross-head movement but the results which come from strain gage are more accurate and more reliable. Test procedure, as it was explained in the previous section, was defined into BLUEHILL control software. Small pre-load ,for example 20KN, would be very useful in order to eliminate the effect of the gaps between mechanical parts of the testing machine.

5.2.2. Results and discussion

Because of the capacity limits of testing machines, the very last step of testing which was supposed to lead to failure was eliminated and the specimen was pulled to a maximum of 7.5% strain instead. Figure 5.7 shows the stress-strain curve obtained from tests of two specimens. Two test results among series of tests are included in this thesis to show the repeatability of the test.

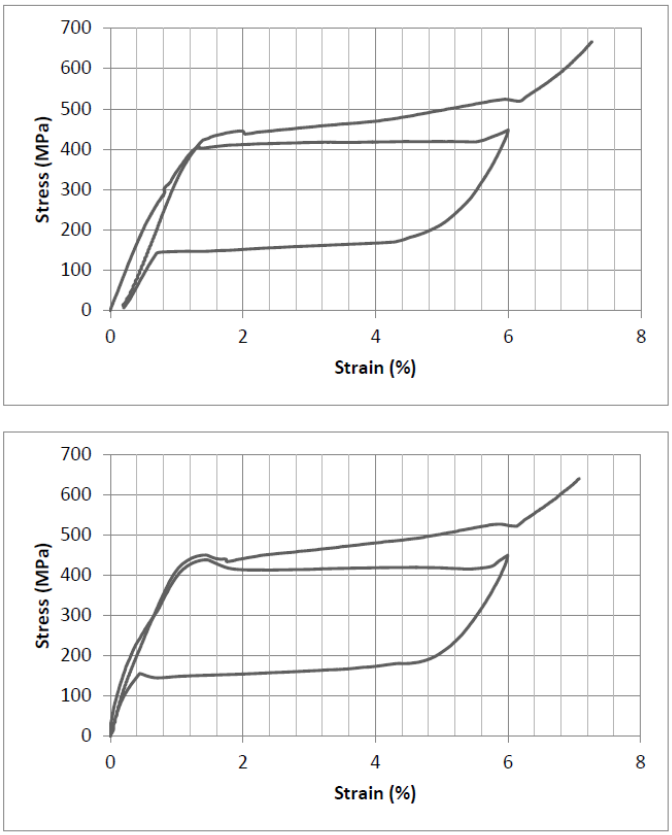

Figure 5.7. Stress-strain curve obtained for NiTi shape memory alloy at room temperature in RD.

Series of tension tests were performed to check repeatability of the test and to have adequate data for calculation of austenitic and martensitic elastic moduli, upper and lower stress plateaus and residual strain. Calculated parameters (average of results from series of tests) are shown in Table 5.1.

Table 5.1. Mechanical properties of NiTi shape memory alloy using 2 KN microtester at room temperature.

Pulling Direction	E_A (GPa)	E_M (GPa)	Upper Plateau Strength (MPa)	Lower Plateau Strength (MPa)
RD	43 ± 2	14 ± 1	415	157

As it can be seen stress-strain curve and consequently the stress plateau is rate dependent and with increasing loading rate, transformation stress is also increasing like slope of the stress plateau. (Nemat-Nasser and Guo 2006 [33]; Dayananda and Subba Rao 2008 [8]). Two main reasons are reported for this effect: First, increasing in temperature due to higher loading rate and second, the formation of stabilized martensite [1]. Also a high elastic modulus was obtained for Austenite. Very low value is reported for apparent martensitic elastic modulus which obviously cannot be true representative for the elastic property of martensite. As it mentioned in some literature, the Young's modulus obtained for martensite was affected by several phenomena such as small amount of strain that comes from transformation process, reorientation of grains, plastic deformation of austenite and detwinning or reorientation of martensite variants. Simple tension test predicts martensitic elastic modulus with errors. Actual elastic modulus of martensite- which was reported much higher than what comes from stress-strain curve- can be measured by different means such as neutron diffraction measurement or unloading-reloading technique and etc [25, 28, 37, 54].

5.3. Tension test in Transverse Direction

5.3.1. Test setup and results

Both screw driven and hydraulic tensile test machines were used to ensure that the results are independent of the type of testing machine. Specimens with end tab were used here too, to avoid slippage. Figure 5.8 illustrates the test setup used for tensile test in RD direction where 10 KN screw-driven ZWICK/ROELL Z010 was used.

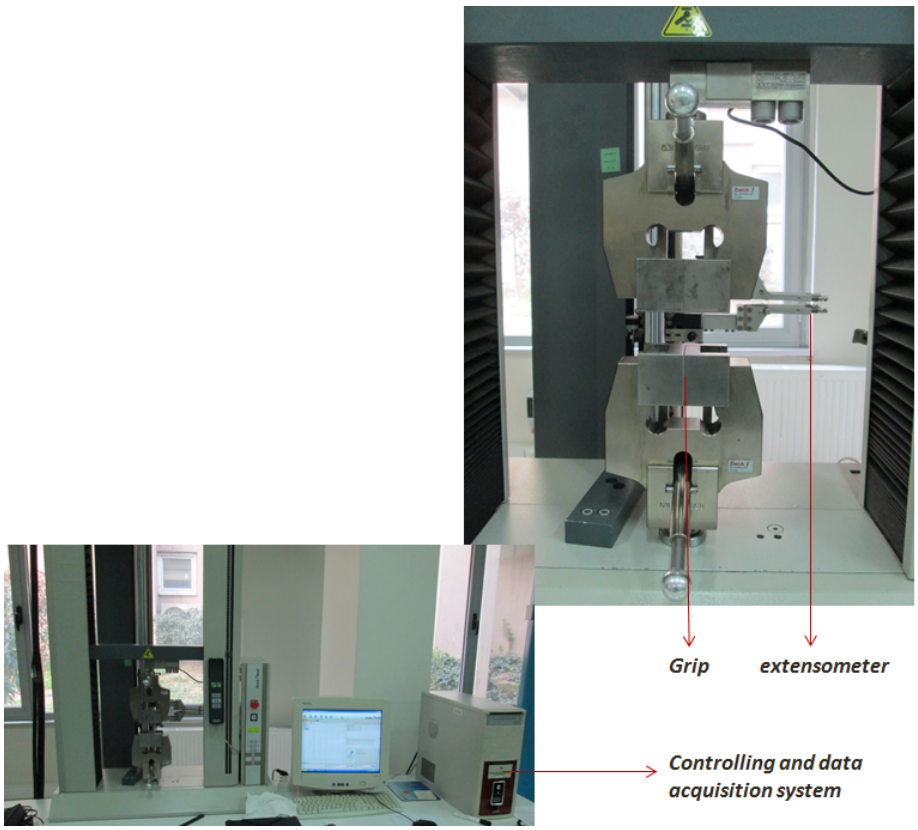

Figure 5.8. Tension test setup for TD direction (10 KN screw-driven ZWICK/ROELL Z010).

Test procedure is exactly the same as the previous one. Strains were obtained from extensometer and the results are shown below:

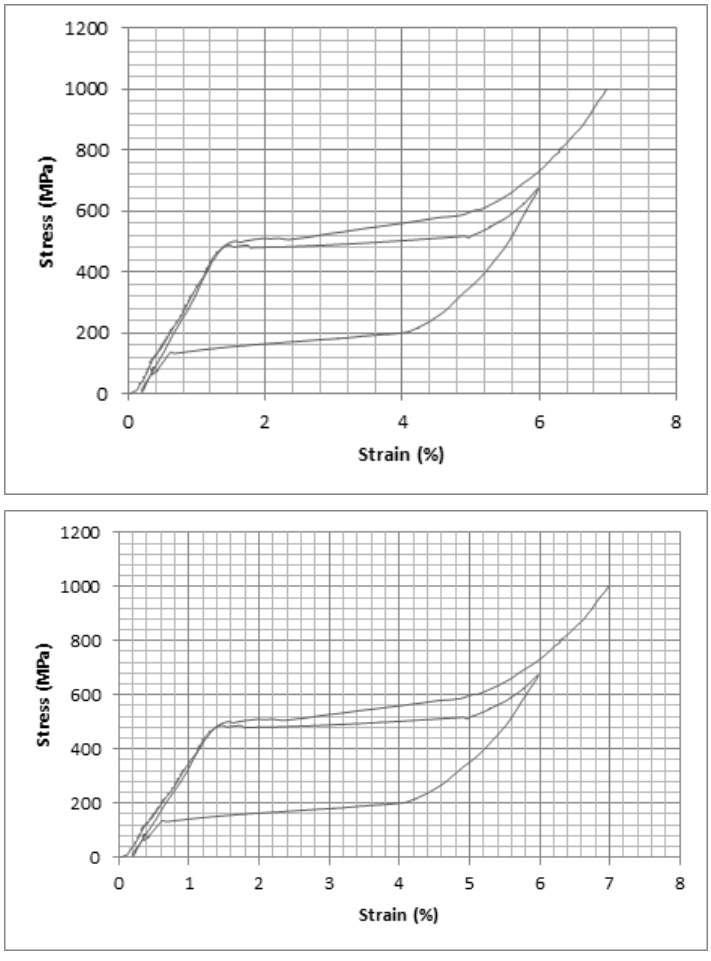

Figure 5.9. Stress-strain curves obtained in TD using ZWICK Z010 testing machine at room temperature.

Table 5.2. Mechanical properties obtained for NiTi shape memory alloy at room temperature in TD direction at room temperature.

Pulling Direction	E_A (GPa)	E_M (GPa)	Upper Plateau Strength (MPa)	Lower Plateau Strength (MPa)
TD	38 ± 1	34 ± 1	498	180

For 100 KN hydraulic INSTRON, the rate of loading at both steps were changed to 3mm/min because of high capacity of the machine and the type of force control used (small unloadings occured during test at lower rates). Implied loading rate was increased step by step until a loading rate of 3 mm/min which was acceptable was obtained. Tensile specimen was pulled up to 6% strain then unloaded to 7 MPa with the same loading rate. At the last step it was pulled up to 8% strain and the test was stopped at the end of loading. Different test rates of tensile test proves the rate dependency of stress-strain curve and stress plateau like it is reported in [4].

Figure 5.10 shows the test setup and Figure 5.11 and Table 5.3 present the stress-strain curve and mechanical properties of the material respectively.

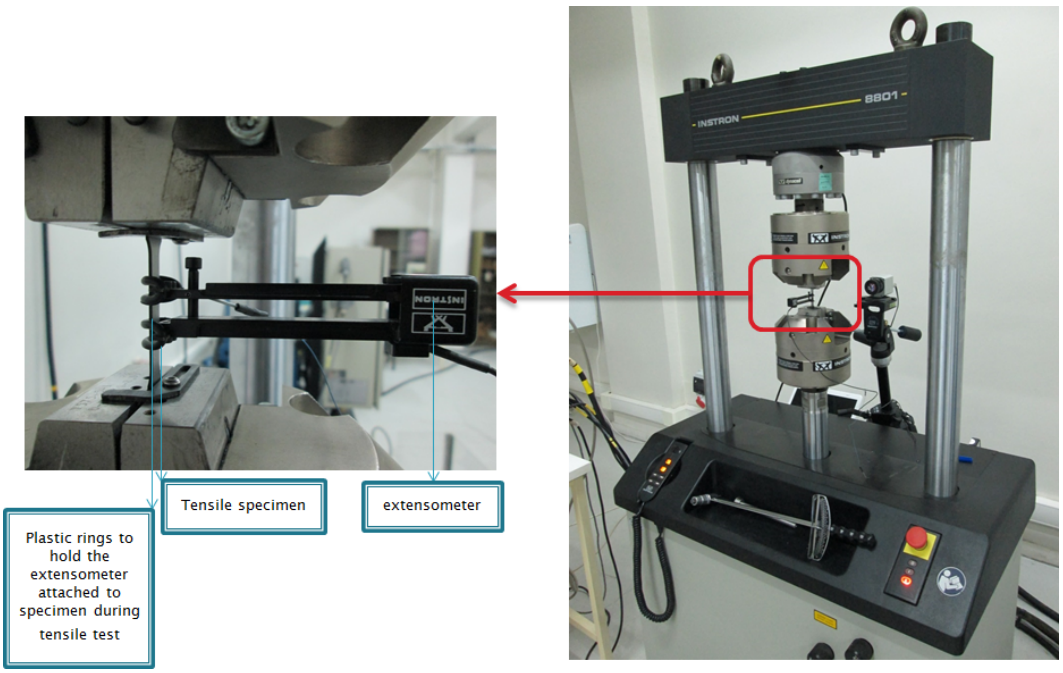

Figure 5.10. Instron 100 KN test machine at the right side and specimen installed on grips with an extensometer to get specimen's elongation at the left side.

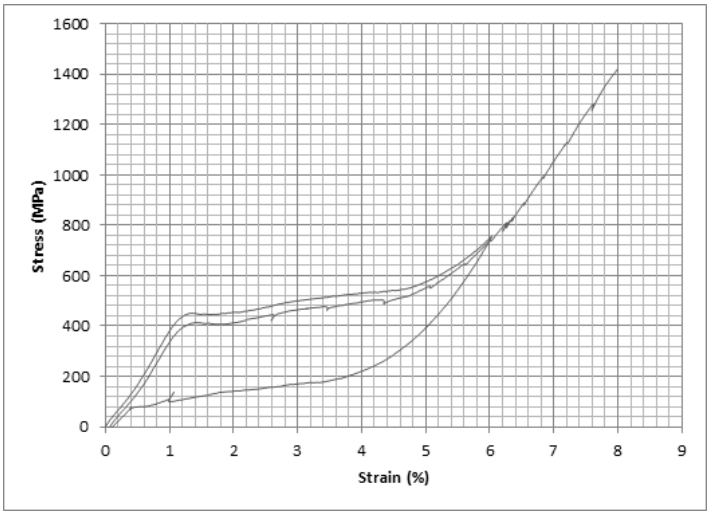

Figure 5.11. Stress-strain curve obtained for NiTi shape memory alloy using 100 KN Hydraulic INSTRON testing machine at room temperature.

Table 5.3. Material properties measured with 100 KN INSTRON.

Pulling Direction	E_A (GPa)	E_M (GPa)
TD	42 ± 2	35 ± 2

Series of tests in higher rates show an interesting rate dependency of the stress plateau. As it can be seen from stress-strain curves obtained at higher loading rate, the stress plateau has a positive slope unlike what was observed in lower rates where this plateau was relatively horizontal.

In order to find ultimate tensile strength of the material in TD another test was carried out and the specimen was loaded with a strain rate of 5 mm/min until it failed. This test also revealed another unexpected result. Besides finding the stress-strain curve and ultimate tensile strength, it was observed that elastic moduli for parent austenite phase and fully transformed martensite phase increased due to higher loading rate. Elastic modulus is obtained to be 48 MPa for austenite and 38 MPa for fully transformed martensite. This result brings a question into mind whether rate of loading affects the material's property even before the initiation of transformation. To answer this question another series of tension tests are needed at different loading rates. Elastic modulus and the stress at which transformation starts can be plotted vs. loading rate to give better idea about the exact effect. This subject is not included in this work.

Figure 5.12 illustrates stress-strain curve for tension test at 5mm/min strain rate. Ultimate tensile strength was obtained to be 1680 MPa at total 8% strain.

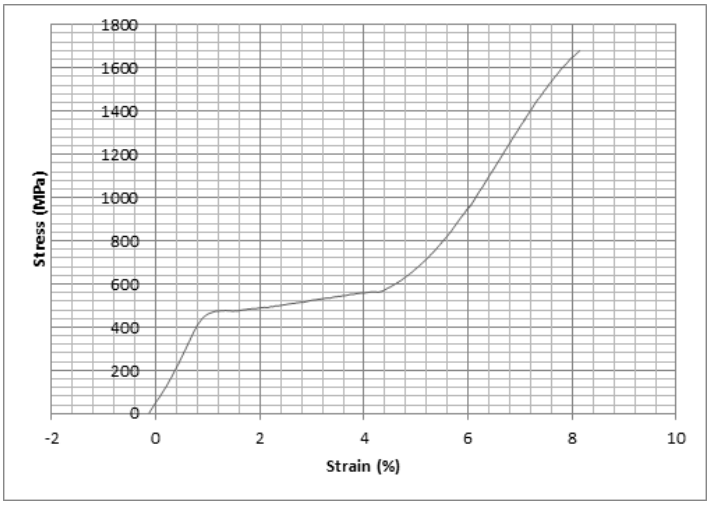

Figure 5.12. Stress-strain curve at 5mm/min strain rate until failure.

5.4. Microstructure

Optical micrograph of the surface was obtained after a good polishing procedure. To make grain boundaries visible, a solution of $3HNO_3 + 2H_2O + 1HF$ was used as etchant [40]. The etchant acts directly on grain boundaries where the stress concentration is at the highest amount and makes these boundaries more visible under microscope. Specimens were held inside the etchant twice each for 60 seconds and were washed by water immediately after they were removed out of etchant solution. To get a better view of the surface under the microscope, polishing started with P180 grinding paper using Metaserv 2000 Grinding and Polishing machine for 2 min. This action was repeated for P320, P400, P600, P1200, P2000 grinding papers. Final two stages were done using Aluminate solution containing 1 and 0.3 Micron particles which provides acceptable fine and mirror-like polished surface to observe grains and to estimate size of grains. Figure 5.13 illustrates the results obtained from this optical micrography. From these pictures it can be seen that the grain size is in the order of 15-20 Micrometer. Local uniform orientation of martensitic bands can also be seen inside each grain.

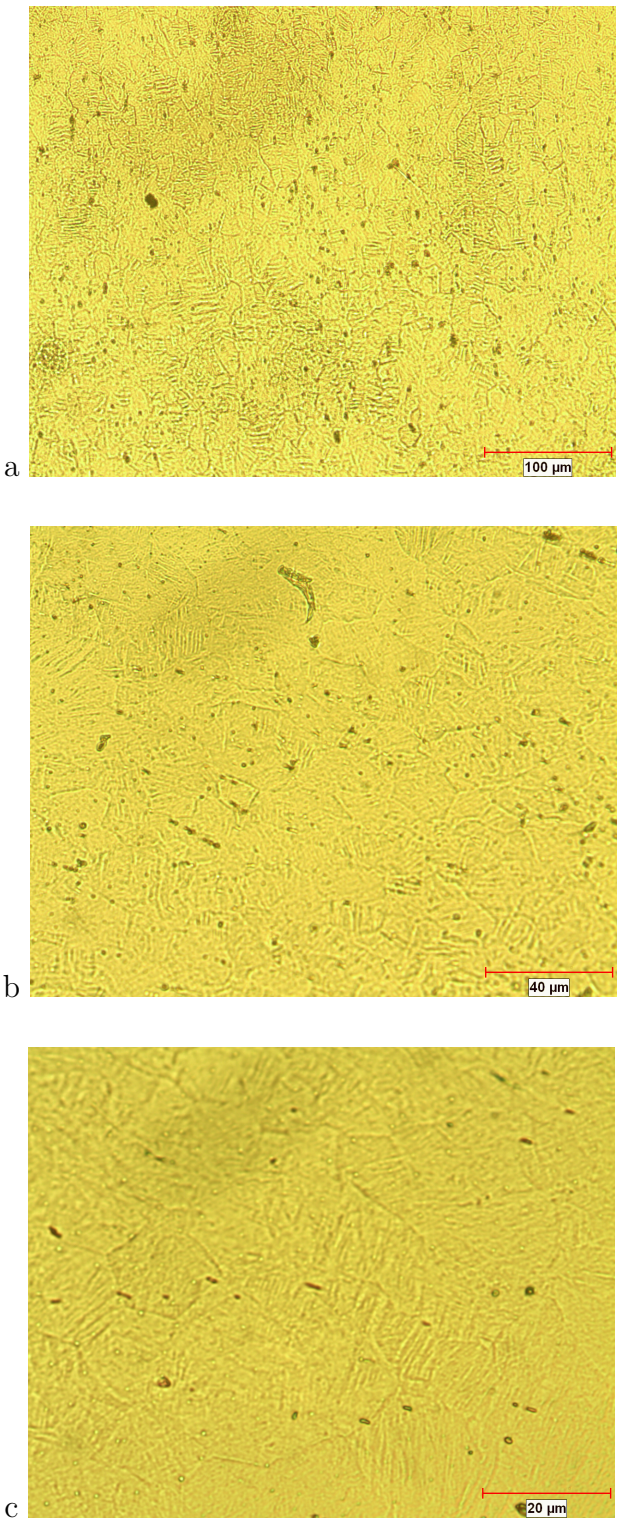

Figure 5.13. Optical micrography of the surface of NiTi shape memory alloy at (a) 20x (b) 50x and (c) 100x optical magnifications.

6. DIGITAL IMAGE CORRELATION (DIC)

6.1. Introduction

Digital image correlation method was developed in the early '80s at the University of South Carolina to measure in-plane displacements and the gradients of those displacement which form strain field for a deforming body [36]. In 1987, this method was implemented to measure crack initiation mode and stress intensity factor for some brittle material. A year later mixed-mode loading was studied using this method and in 1992, 3D effect near a crack tip was investigated. Wide range of application allowed scientists to measure deformation in micro and nano scale using this method. Plastic deformation in ductile materials in 1997 and large deformations in 1998 became two other applications of this method. In 2002, this method was used to construct crack growth resistance curve for functionally graded materials (FGM) [34] and in 2007 S. Daly used it in the case of shape memory alloys to find strain field related to martensitic transformation [7].

6.2. Basic conceps of DIC

Digital image correlation or DIC is a non-contacting optical measurement method to obtain deformation on the surface of a body. To do this, two images taken from the surface of the body in undeformed and deformed states are compared. Pictures should be taken from speckled surface to be able to be used in this method. This method supports a large range of size scale from 10^{-9} to 10^{2} meters and large range of time scale from static condition to 200 MHz. Using image deformation, surface deformation can be obtained and strains can be computed from displacements of features in images. Deformation or displacements of a point on surface are defined as vector difference between coordinates of that specific point in deformed and undeformed images. To

have sufficient number of points to identify displacement field, a proper grid on region of interest is needed. Displacement gradients on each grid point are calculated using classic continuum mechanics to form strain tensor. In DIC method this is done using standard derivative filters. The most important thing which should be kept in mind is that imaged surfaces must remain at the same distance during shooting of the picture and parallel to visual sensor. Any changes in distance or surface angle results in measurement errors. Perspective distortion could be the reason of artificial strains. This distortion occurs if the planar specimen surface is not parallel to image sensor (CCD camera). Another possible distortion which also causes parasitic displacement gradients is lens distortion. This distortion can be avoided by calibrating the lens before imaging. Out of plane motion which is another source of error in this method should be avoided as much as possible. One way to do this is to put a small preload on the specimen prior to main test. Digital image correlation technique is able to do full-field measurement with high accuracy. This method is accepted as a fast and economic way to do measurements without direct contact with specimen [5, 24, 43]. In Figure 6.1 a schematic illustration of method setup is shown.

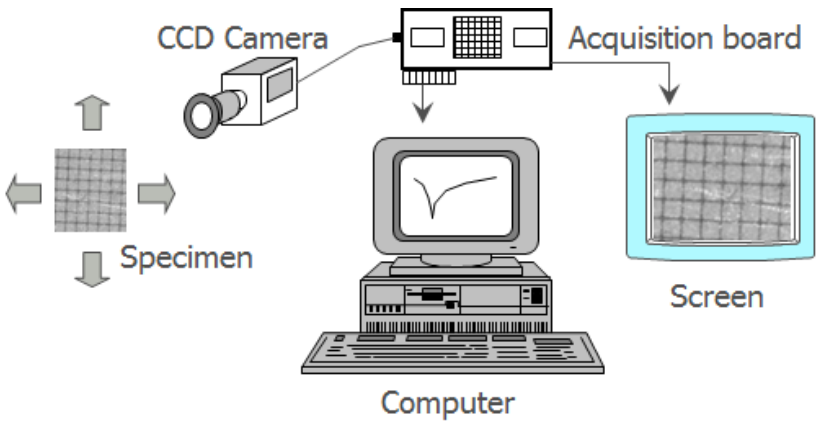

Figure 6.1. DIC setup.

Pictures from the surface of the specimen are taken by a CCD camera (charge

coupled camera) and an acquisition board sends these images to a screen. Data interpretation is done in another computer unit to extract displacement and strain fields. The basic idea in this method is to track a given point on the surface of a body (undeformed image), in different stages of deformation (deformed images) to find the best point which its signature minimizes the correlation factor. Figure 6.2 illustrates this idea on the actual images.

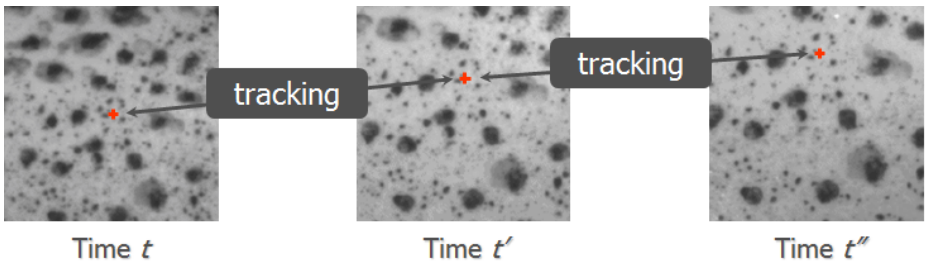

Figure 6.2. Tracking a specific point at different stages of deformation.

The signature can be any discrete characteristic of a point which makes it specific such as colored speckles. Obviously there are many points on the surface which could possibly have very similar signature. To track the point more accurately, a neighborhood named a subset is set around the point. Figure 6.3 shows how a subset is set on the surface of a body.

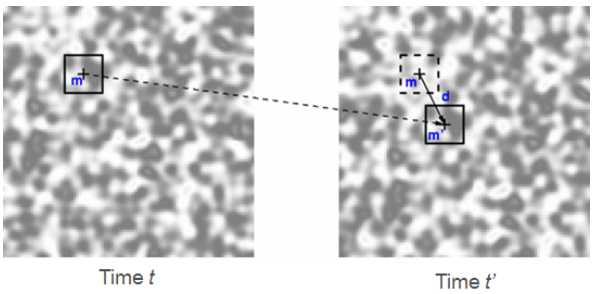

Figure 6.3. Subset tracking in deformed image.

The pattern which is used for tracking should have some properties. A non-repetitive, isotropic and high-contrast pattern is needed and the best pattern which satisfies these conditions is speckle pattern. Uniform pattern without any preferred orientation and with relatively dense speckle is considered as a good pattern. Sufficient number of speckles with suitable size must be guaranteed on the surface of the specimen. The best speckle size is approximately 3-5 pixels in size and its ratio to pixels is 5:1 [5]. This speckle size allows analysis with smaller subset and high spatial resolution. An acceptable pattern must deform with sample without imposing any force on the sample. Also the pattern should endure till the end of the deformation process. Figure 6.4 illustrates patterns with problems in size or number of the speckles.

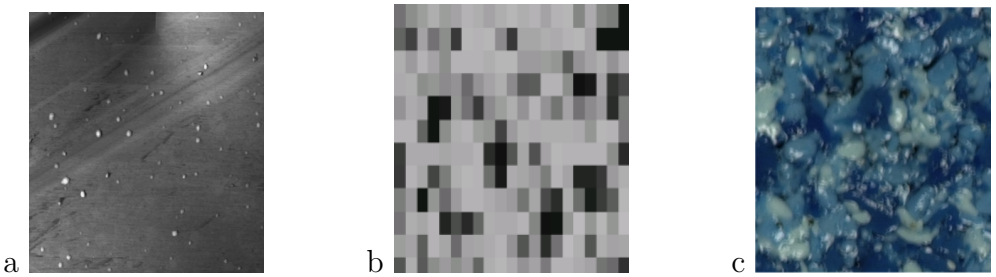

Figure 6.4. Improper patterns (a) few or no speckles (b) too small speckles (c) too big speckles.

Figure 6.5 show improper and proper patterns for DIC technique.

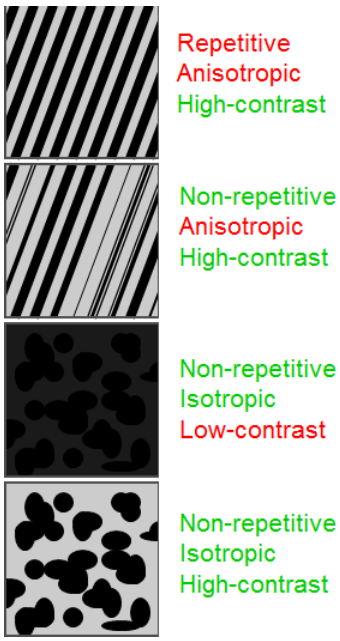

Figure 6.5. Improper and proper patterns for DIC method.

6.3. Image correlating algorithm

The example below from reference [24], simply represents the basic idea behind digital correlation: consider a 9×9 pixel image taken by a camera from a specimen with a pattern as shown in Figure 6.6. If we assign values of 100 to white pixels and 0 to the black ones, we can present the specimen by a matrix as shown in Figure 6.7.

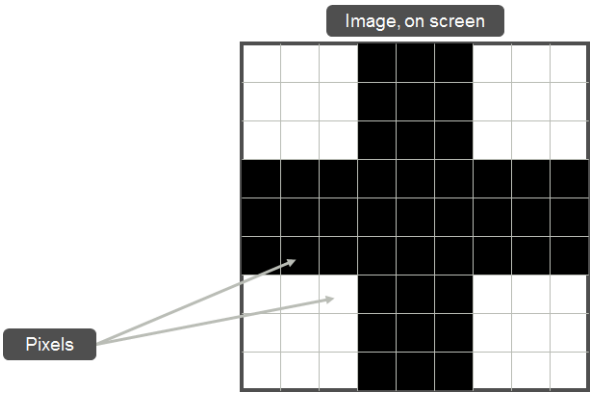

Figure 6.6. Chosen pattern on arbitrary specimen.

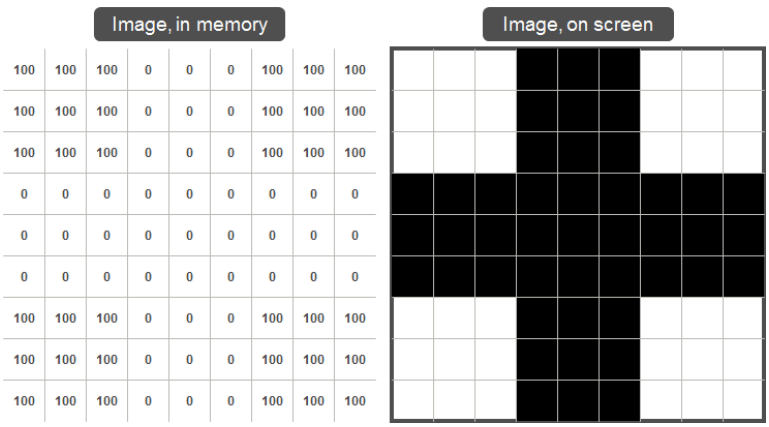

Figure 6.7. Values assigned to black and white pixels.

Now assume an arbitrary movement of the specimen by an amount 1 pixel in both x and y-directions as shown in Figure 6.8.

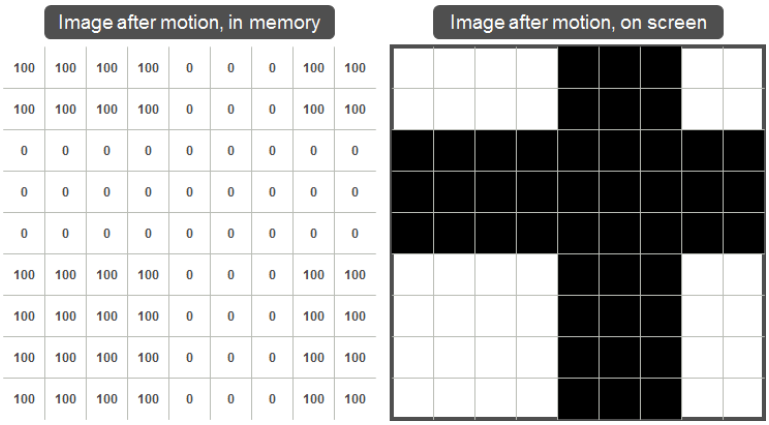

Figure 6.8. Deformed image, associated matrix and values assigned.

These matrices are used to explore the possible point in deformed configuration which is the best match for original point in undeformed image by plugging the pixel values in the correlation function. As it was mentioned before, the point which minimizes this function is recorded as the seeking point. Correlation function is sum of the squared differences of the pixel values and has the following form:

$$\mathbf{C}(x,y,u,v) = \sum_{i,j=-\frac{n}{2}}^{\frac{n}{2}} \Big(I(x+i,y+j) - I^*(x+u+i,y+v+j) \Big)^2 \tag{6.1}$$

where $\mathbf{C}$ is correlation function, x, y are pixel coordinate in undeformed image, u, v are displacement, n is subset size, I and I^* indicate pixel values in images before and after motion of the points $\binom{x+i}{y+j}$ and $\binom{x+i+u}{y+j+v}$ respectively.

Pixel or intensity values in most cases range from 0 to 255. Figure 6.9 shows a graphicl representation of a digital-speckle image.

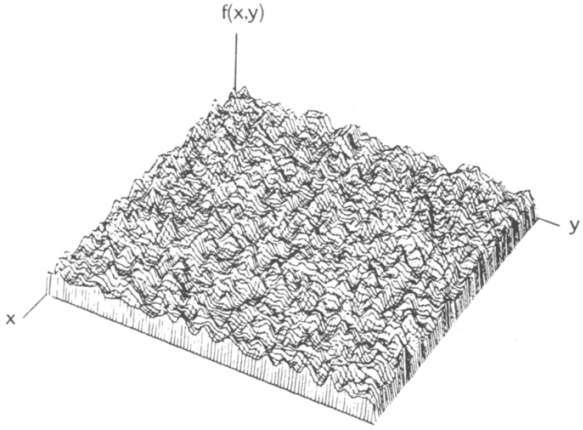

Figure 6.9. Graphical illustration of pixel values of an image.

Figure 6.10 shows two pixel-valued matrices for an arbitrary case, one for undeformed state and the other one for deformed state. Let's assume a 5×5 subset centered at the coordinate (5, 5) in 9×9 picture and guess initially a (-2, -2) displacement. The aim is to check if this is the displacement that has been occurred.

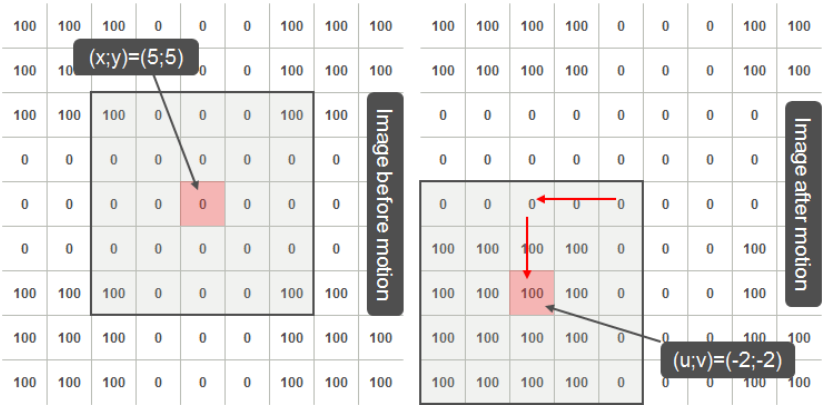

Figure 6.10. Iinitial guess for u and v for an arbitrary deformation to calculate the correlation factor.

Calculating C will tell us:

$$\mathbf{C}(5,5,2,2) = \sum_{i,j=-2}^{2} \Big(I(5+i,5+j) - I^{*}(5-2+i,5-2+j) \Big)^{2} = 1800$$

Now if we guess (u, v) as (1, 1) as it is shown in Figure 6.11 and calculate C, it will be:

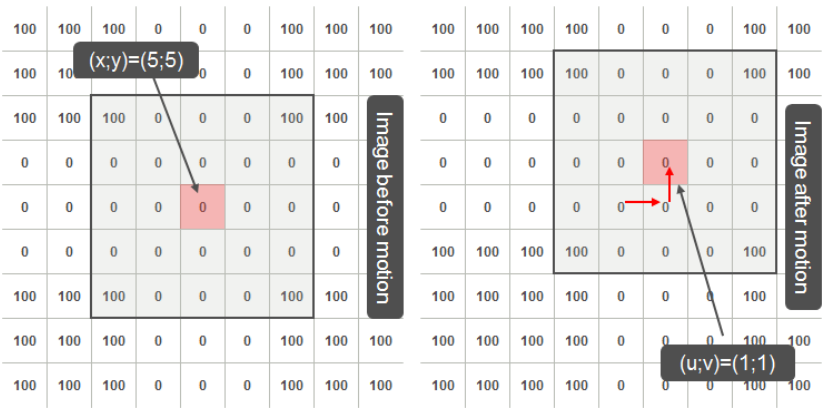

Figure 6.11. Second guess for u and v to calculate the correlation factor.

$$C(5,5,1,1) = \sum_{i,j=-2}^{2} \Big(I(5+i,5+j) - I^{*}(5+1+i,5+1+j) \Big)^{2} = 0$$

Obviously second guess which led to the minimum correlation factor is the sought displacement. This seeking process is done iteratively for all points and displacement field is extracted at the end. It should be mentioned that in real cases, where many kinds of external noises affect quality of images, the correlation factor does not necessarily become zero. For example for the case here it could be like:

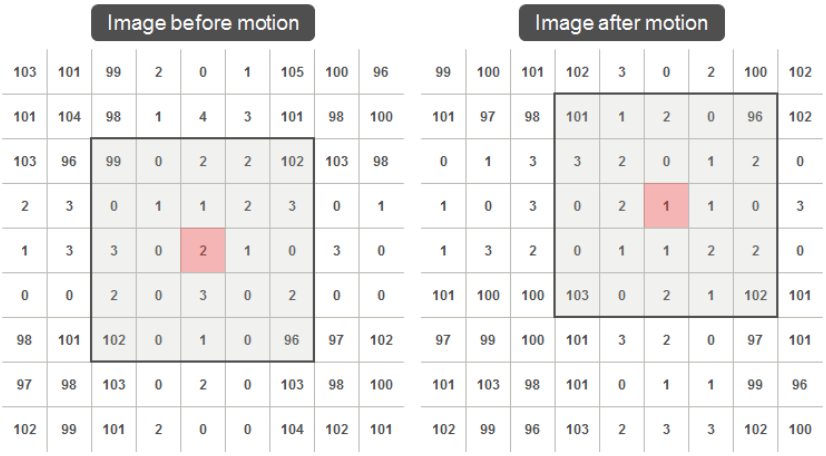

Figure 6.12. Effect of noise on calculating correlation coefficient.

Finding initial rough estimate as the first step, to get the best location of specific point in deformed image, refinement is needed. This refinement is done by using information that comes from the point's neighborhood. Several optimization methods are used in to refine subset displacement (u, v). Some of these methods are: a) FFT methods, b) Generic algorithms, c) Coarse-fine search, d) Iterative optimization

Pictures which were taken, are made of pixels and each pixel has a different gray scale value. These make the whole map to be a non-continuous one and each subset unique as shown in Figure 6.13. To reconstruct a continuous space, image interpolation using B-splines is done on images. Aa an example, two different interpolations are shown: one for first order and another one for 10th order interpolation in Figure 6.14 [24].

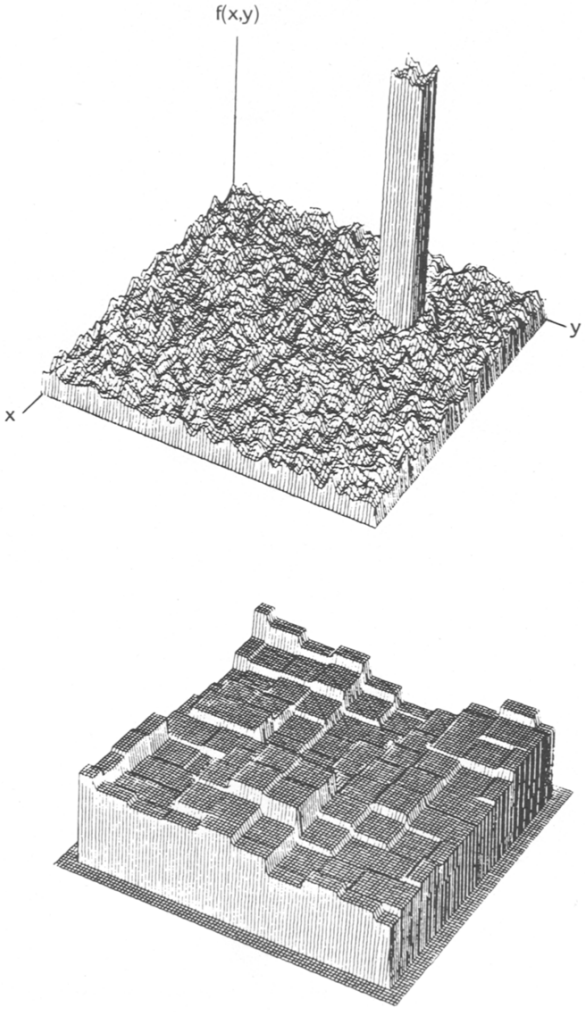

Figure 6.13. An arbitrary subset (top) and zeroth order interpolation (bottom).

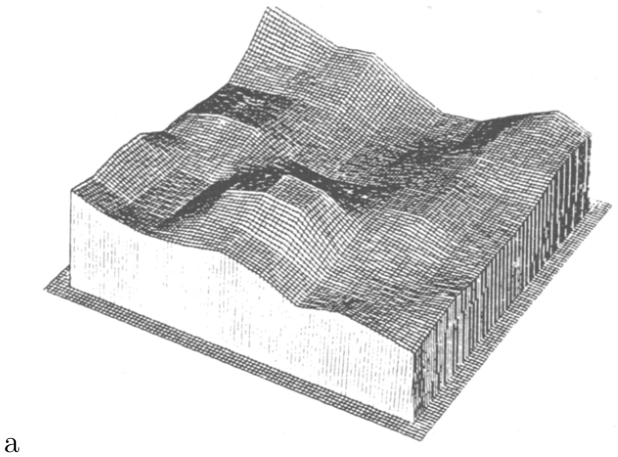

a

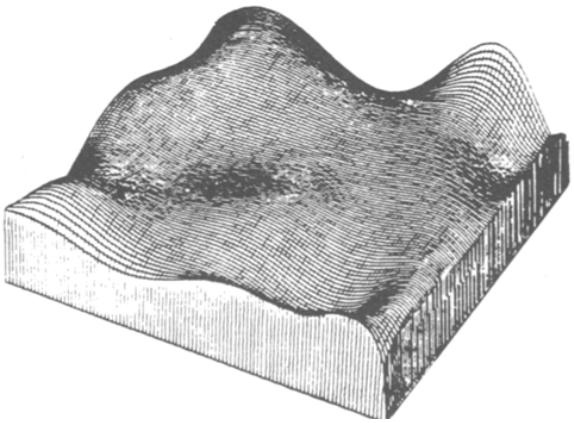

b

Figure 6.14. Bilinear (first order) (a) polynomial (order of 10) (b) interpolation schemes.

7. METHOD VALIDATION USING ALUMINUM

As it was mentioned in section 4, the whole procedure in this thesis needs validation to get the capability to be implemented on mechanically less known NiTi shape memory alloy. This validation could be done using a well-known traditional metal like aluminum. Aluminum is used for fracture testing very often because its brittleness beside low cast and existing in several forms make this metal very suitable to demonstrate fracture of industrial metals. Fracture parameters of aluminum have been extracted and are available widely.

7.1. Basic concepts of linear elastic fracture mechanics (LEFM)

For a cracked body, stress distribution around the crack tip can be obtained using an assumption of isotropic linear elastic material behavior. The stress distribution around the crack tip for such a material can be expressed as:

$$\sigma_{ij} = \left(\frac{k}{\sqrt{r}}\right) f_{ij}(\theta) + \sum_{m=0}^{\infty} A_m r^{\frac{m}{2}} g_{ij}^{(m)}(\theta) \tag{7.1}$$

where σ_{ij} is the stress tensor and r, θ are polar coordinates shown in Figure 7.1, k is a constant and f_{ij} is a function of r, θ.

Second part of the expression in Equation 7.1 shows higher order terms which depend on geometry.

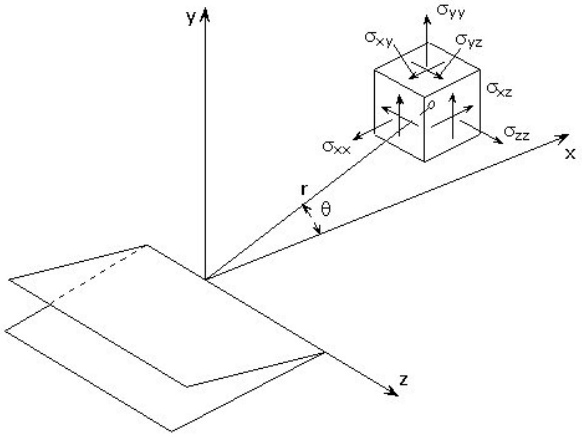

Figure 7.1. Coordinate system used at the tip of a crack in an infinite plate.

As it can be seen, for any configuration, approaching to the tip of crack ($r \to 0$) first term in Equation 7.1 tends to infinity because of $(1/\sqrt{r})$ term. It means that stress at the region near the crack tip highly depends on $(1/\sqrt{r})$ term and the second part of the Equation 7.1 is negligible. This is known as stress singularity around the crack tip.

Stress intensity factor represents the amplitude of the singularity at the tip of an ideal sharp crack in a material that shows linear elastic behavior and can define the condition at the crack tip completely. It means that if stress intensity at the crack tip is known, all other terms related to crack tip can be evaluated. Stress intensity factor depends on size of crack, amount of stress and geometry of the body and varies for different material. It is affected by temperature and loading rate.

For an infinite elastic isotropic plate which is subjected to remote uniform stress the stress fields can be expressed by Table 7.1

Table 7.1. Stress components at the tip of a crack for an infinite center-cracked body subjected to uniform stress.

	Mode I	Mode II	Mode III
σ_{xx}	$\frac{K_I}{\sqrt{2\pi r}}\cos\left(\frac{\theta}{2}\right)\left[1-\sin\left(\frac{\theta}{2}\right)\sin\left(\frac{3\theta}{2}\right)\right]$	$-\frac{K_{II}}{\sqrt{2\pi r}}\sin\left(\frac{\theta}{2}\right)\left[2+\cos\left(\frac{\theta}{2}\right)\cos\left(\frac{3\theta}{2}\right)\right]$	0
σ_{yy}	$\frac{K_I}{\sqrt{2\pi r}}\cos\left(\frac{\theta}{2}\right)\left[1+\sin\left(\frac{\theta}{2}\right)\sin\left(\frac{3\theta}{2}\right)\right]$	$\frac{K_{II}}{\sqrt{2\pi r}}\sin\left(\frac{\theta}{2}\right)\cos\left(\frac{\theta}{2}\right)\cos\left(\frac{3\theta}{2}\right)$	0
σ_{xy}	$\frac{K_I}{\sqrt{2\pi r}}\cos\left(\frac{\theta}{2}\right)\sin\left(\frac{\theta}{2}\right)\cos\left(\frac{3\theta}{2}\right)$	$\frac{K_{II}}{\sqrt{2\pi r}}\cos\left(\frac{\theta}{2}\right)\left[1-\sin\left(\frac{\theta}{2}\right)\sin\left(\frac{3\theta}{2}\right)\right]$	0
	0 (plane stress) $\nu(\sigma_{xx}+\sigma_{yy})$ (plane strain)	0 (plane stress) $\nu(\sigma_{xx}+\sigma_{yy})$ (plane strain)	-
σ_{xz}	0	0	$-\frac{K_{III}}{\sqrt{2\pi r}}\sin\left(\frac{\theta}{2}\right)$
σ_{yz}	0	0	$\frac{K_{III}}{\sqrt{2\pi r}}\cos\left(\frac{\theta}{2}\right)$

The displacement fields around the crack tip for Mode I and Mode II are shown in table 7.2.

Table 7.2. Displacement field around the tip of crack for mode I and II.

	Mode I	Mode II
u_x	$\frac{K_I}{2\mu}\sqrt{\frac{r}{2\pi}}\cos\left(\frac{\theta}{2}\right)\left[\kappa-1+2\sin^2\left(\frac{\theta}{2}\right)\right]$	$\frac{K_{II}}{2\mu}\sqrt{\frac{r}{2\pi}}\sin\left(\frac{\theta}{2}\right)\left[\kappa+1+2\cos^2\left(\frac{\theta}{2}\right)\right]$
u_y	$\frac{K_I}{2\mu}\sqrt{\frac{r}{2\pi}}\sin\left(\frac{\theta}{2}\right)\left[\kappa+1-2\cos^2\left(\frac{\theta}{2}\right)\right]$	$-\frac{K_{II}}{2\mu}\sqrt{\frac{r}{2\pi}}\cos\left(\frac{\theta}{2}\right)\left[\kappa-1-2\sin^2\left(\frac{\theta}{2}\right)\right]$

The displacement field for Mode III is:

$$u_z = \frac{K_{III}}{\mu}\sqrt{\frac{r}{2\pi}}\sin\left(\frac{\theta}{2}\right) \tag{7.2}$$

where μ is shear modulus, $\kappa = 3 - 4\nu$ is for plane strain and $\kappa = (3-\nu)/(1+\nu)$ is for plane stress.

For this configuration, under pure Mode I loading and by assuming that stress intensity factor changes proportional to remote stress:

$$K_I = \sigma\sqrt{\pi a}\,(MPa\sqrt{m}) \tag{7.3}$$

For other specimen configurations a correction factor is needed. This factor is a function of the ratio of the crack length to plate's width (a/W) and is formulated for different configurations experimentally.

7.2. Stress intensity factor as a material property

For small scale yielding, plane strain condition is satisfied in the interior of the specimen away from free surfaces. The critical stress intensity factor K_c is considered as material resistance to fracture and is named as fracture toughness. The effect of specimen thickness on stress intensity factor is shown in Figure 7.2. It can be seen that stress intensity factor decreases by increasing thickness until it becomes constant with further increasing in thickness after a specific thickness. For a cracked material subjected to increasing load, failure occurs when stress intensity factor reaches material's fracture toughness value.

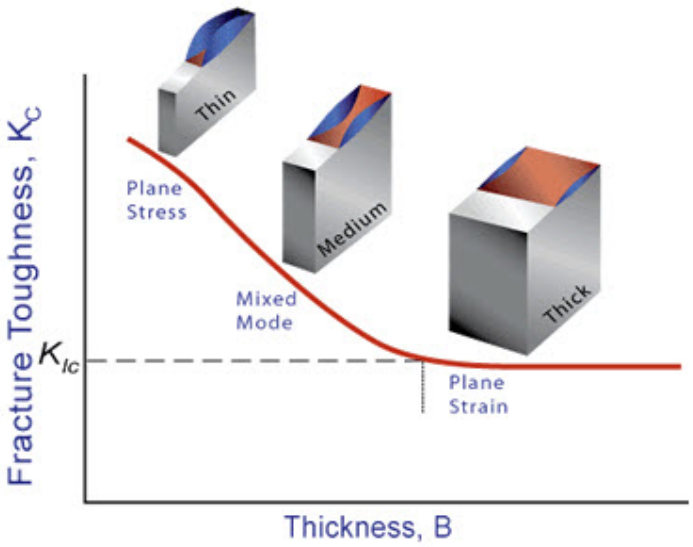

Figure 7.2. Variation of stress intensity factor at the crack tip with thickness [11].

7.3. Experiments using Aluminum

7.3.1. Test setup

The test setup used for experiments mentioned in section 3, is shown in Figure 7.3

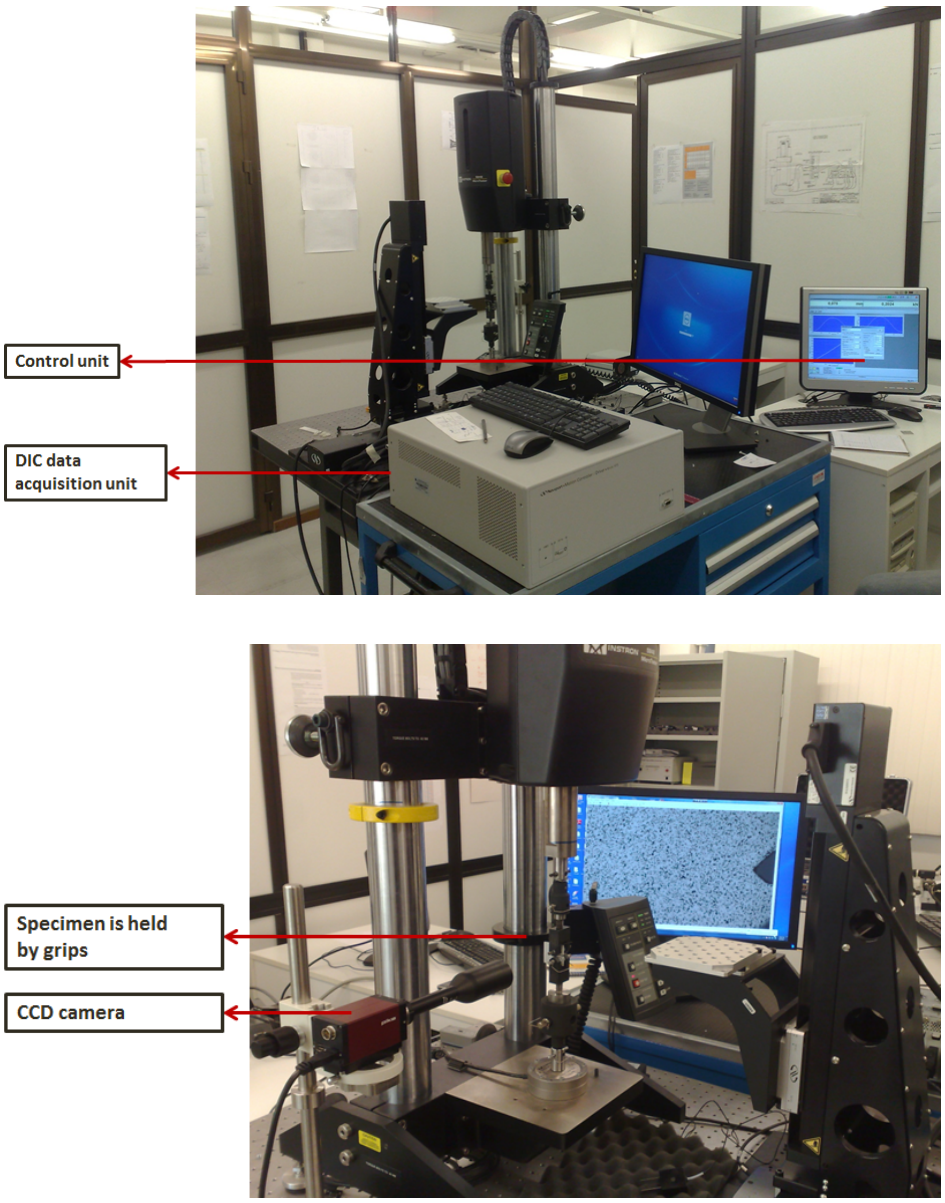

Figure 7.3. Test setup for Digital Image Correlation (DIC) technique used for aluminum.

The whole surface of the specimen is painted using a white spray, then black speckles are sprayed on white surface several times in very short intervals. Painted specimen is shown in Figure 7.4.

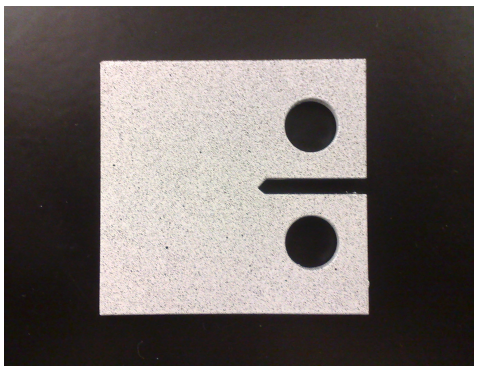

Figure 7.4. Aluminum DT specimen used for fracture test.

WinDIC menu 1.3 software is used to extract displacement and strain fields form deformed and undeformed images. In this thesis a Python code was used to run WinDIC menu 1.3. Most important input data is deformed and undeformed images which must be in the proper size and resolution (1006×990 in this case). Each 61 pixel represent 1 millimeter therefore field of view for the applied lens is 16.5×16.3 mm^2. A proper grid was set on the images.

For the first step a coarse optimization was done using initial guesses for u and v. A subset of the size subset size (2nsub+1, 2msub+1) around any point was set. This neighborhood was used to characterize each point. Coarse optimization was done inside the coarse region defined by coarse size (2nrtx+1, 2nrty+1) around any point G. Correlating two images, an initial estimation for new position of G in deformed image was stored. This new position move of the amount coarse step (ntrincx, ntrincy) and correlation repeats and another position for G in deformed image was found. This was done iteratively until the best position which makes correlation function minimum, was found. For the next step coarse step was divided by step divider (nconfigx, nconfigy) and the whole process was repeated. Dividing coarse step continues until it becomes equal to final coarse step size (nacc). The last position found for G in deformed image

was used to calculate strain and displacement at that point.

Undeformed and deformed images used for DIC analysis are shown in Figure 7.5, and the grid is shown in Figure 7.6.

a 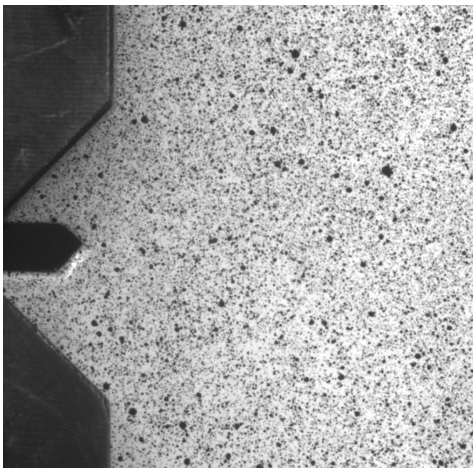 b 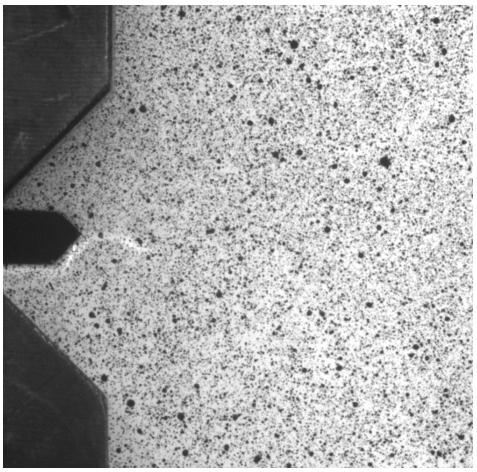

Figure 7.5. Aluminum CT specimen at load-free condition (a) image right before fracture (b).

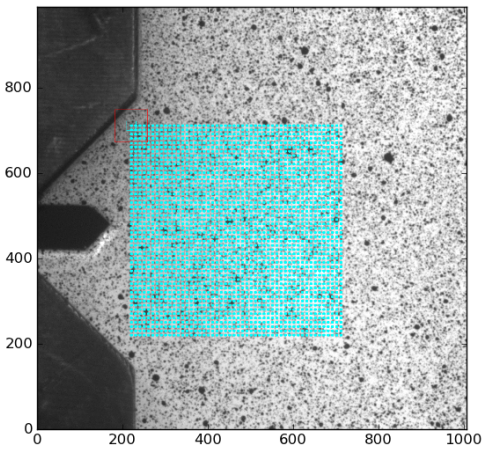

Figure 7.6. Grid on undeformed image set by WinDIC menu 1.3 software.

Extracted displacement data in y-direction was fitted to Equation 4.1 using a Matlab code to obtain K_I, K_{II}, T, A_0, u_0 which are Mode I and Mode II stress intensity factors, T-stress, rigid body rotation and rigid body translation respectively.

7.3.2. Specimen properties and configuration

To validate experimental procedure, Aluminum 7075-T651 was chosen because of its good brittleness that makes it a proper material for fracture tests. Material properties are tabulated in Table 7.3 and specimen configuration is shown in Figure7.7.

Table 7.3. Mechanical properties of Aluminum.

Ultimate Tensile Strength	538 (MPa)
Tensile Yield Strength	469 (MPa)
Modulus of Elasticity	71.7 (GPa)
Poisson's Ratio	0.33

7.3.3. Test procedure

Compact tension specimen under plane stress loading was used to calculate critical stress intensity factors. Test guideline was chosen as ASTM E399-09 (American Society for Testing and Material Standard Test Method for Linear-Elastic Plane-Strain Fracture Toughness K_{Ic} of Metallic Materials). It should be noted that the aim of this thesis is not to find and establish plane strain fracture toughness value for certain material but to explore the effect of martensitic transformation on the fracture parameters like critical stress intensity factor. In addition, Aluminum and NiTi shape memory alloy are both highly brittle materials that insures very small plastic zone under normal loading condition.

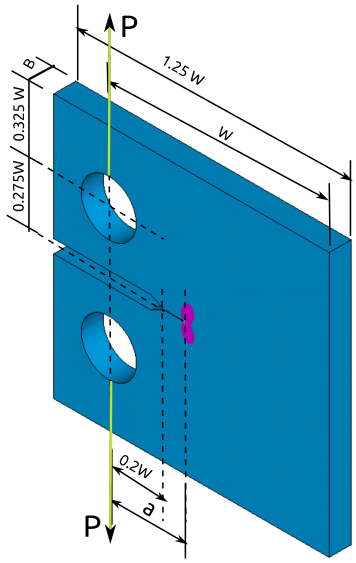

Figure 7.7. CT specimen configuration used for fracture test.

Experiments have shown that a mechanical narrow notch does not represent an actual growing crack and cannot simulate real stress condition at the crack tip. To produce an ideally sharp crack, fatigue precracking was done prior to tests. Fatigue pre-crack ensures the propagation in the crack plane and prevents out-of-plane crack growth. Cyclic loading was carried out until proper precrack was achieved. Pre-cracking load must be such that the stress intensity during cycles does not exceed from 80% of the estimated or reported fracture toughness of the material [9]. For aluminum that was used in this experiment the estimated fracture toughness was around 25 $MPa\sqrt{m}$ and stress intensity under cyclic loading should not reach and go further than 20 $MPa\sqrt{m}$. A maximum pre-cracking force of 0.4 KN was chosen and it took 6000 cycles to produce a precrack with appropriate length.

Aluminum fatigue pre-cracked CT specimen was subjected to incrementally increasing load and at the end of each increment, the test was stopped and a corresponding image was taken. Smaller increments provide better estimations of fracture

moment. The very last image before apparent fracture was chosen as deformed image and an image was taken before imposing any load on the specimen was chosen as undeformed image in digital image correlation software. Little relaxation is expected that can cause a relatively higher resistance to further crack initiation. This means the obtained critical stress intensity factor could possibly be greater than its actual value. This is considered to have a negligible effect at the end of the day. Dimensions of the specimen and results are shown in Table 7.4 . The aim was just to find out whether the DIC technique yielded the same fracture parameters as Finite Elements and other linear elastic fracture mechanics results.

7.3.4. Results and discussion

Load-load line vs. extension curve for this experiment is shown in Figure 7.8.

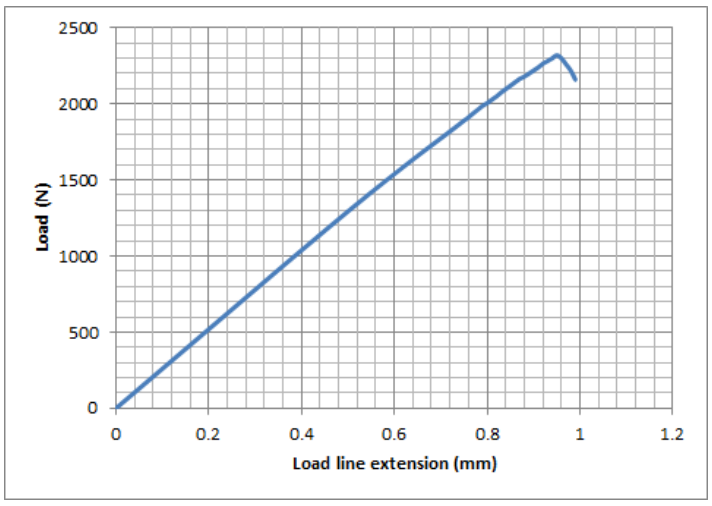

Figure 7.8. Load-extension curve for Aluminum at room temperature.

Table 7.4. Critical stress intensity factors calculated using DIC data.

Condition	B mm	W mm	a mm	a/W	r_{min}	r_{max}	K_I MPa$\sqrt{m}$	K_{II} MPa$\sqrt{m}$	T MPa	A_0	u_0
Plane stress	2	26	8.8	0.338	0.045	0.36	43.18	-0.89	-65.59	-0.0021	0.3359

Figure 7.9 (a) demonstrates a graphical illustration of the displacement field around the crack tip and Figure 7.9 (b) represents the filtered region and the area at the crack tip on which the calculation are based. Boundaries of this region are specified in Table 7.4 with the name r_{min} and r_{max} such that the ratio r/a (where $r^2 = x^2 + y^2$) stays between r_{min} and r_{max}. Also because displacement at the crack surface blows, another filter takes data from $-179°$ to $179°$ to eliminate the unwanted data.

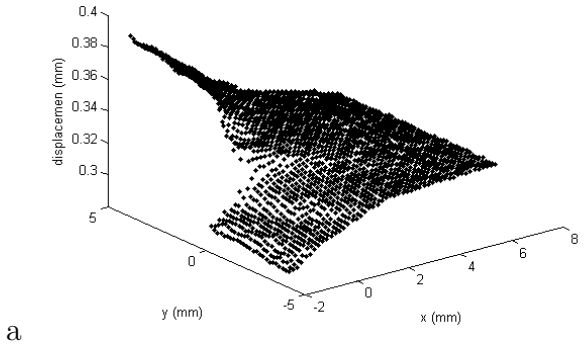

a

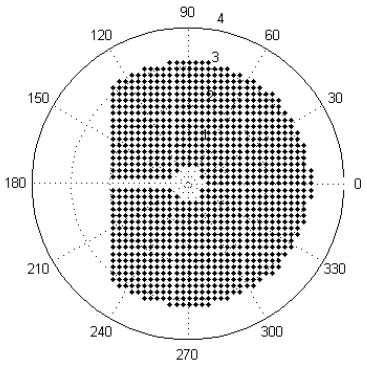

b

Figure 7.9. (a) Displacement field in the direction of loading for aluminum obtained by DIC (b) Filtered data region.

Displacement contour was plotted for field extracted from DIC data and after doing least-squares fit to Equation 4.1 and after finding five constants of this equation. The calculated displacement field with obtained constants is also plotted on the same graph.

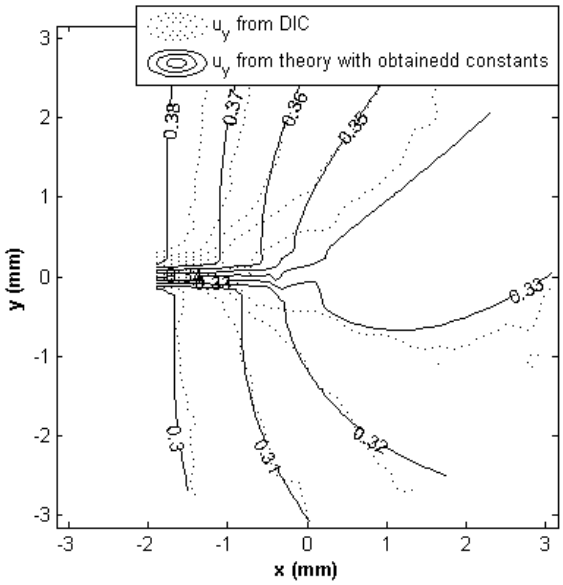

Figure 7.10. Displacement contours for data from DIC and from Equation 4 using the calculated constants for aluminum.

7.4. Calculation of critical stress intensity factor using LEFM

ASTM E399-09 testing standard suggests calculating fracture toughness of linear elastic isotropic material with Hooke's low by using the stress-CMOD (crack mouth opening displacement) curve. First of all, a conditional result K_Q is calculated using P_Q. P_Q is obtained from the mentioned curve by drawing a secant line OP_5 which passes the origin and has a slope of 0.95 PA (linear portion of the curve) (Figure 7.11). Three possible cases were considered in calculation of P_Q. If the force at the part of the curve before P_5 is less than that for any data point, then P_Q is P_5 (type I). If there is any force amount greater than P_5 before it, then P_Q will be that force (type II and III) [9].

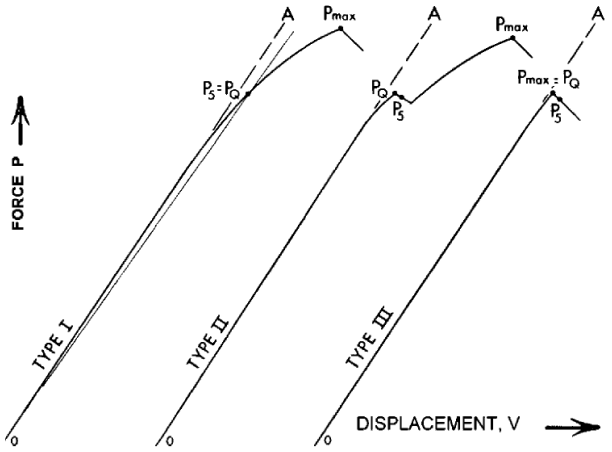

Figure 7.11. Possible force-displacement curves which can be obtained from fracture tests and the definition of P_Q for each.

Obtained P_Q was used to calculate K_Q and as it was mentioned previously that if it satisfies some criteria, the K_Q obtained can be denoted as material fracture toughness. Although in this thesis, conditions do not meet the criteria, this K_Q still was

used as the critical stress intensity factor for this specific thickness and loading type. Therefore using the maximum load reached in DIC test, a good estimation of critical stress intensity factor at the crack tip right before the fracture can be obtained and can be compared to those obtained from DIC. To calculate K, Equation 4.2 for an edge-cracked CT specimen was used.

$$K = \frac{P}{B\sqrt{W}}.f\left(\frac{a}{W}\right) \tag{7.4}$$

where P is force as determined using Force- Displacement records, B is specimen thickness, W is specimen width, a is crack size and

$$f\left(\frac{a}{W}\right) = \frac{\left(2+\frac{a}{W}\right)}{\left(1-\frac{a}{W}\right)^{\frac{3}{2}}}\left[0.886 + 4.64\frac{a}{W} - 13.32\left(\frac{a}{W}\right)^2 + 14.72\left(\frac{a}{W}\right)^3 - 5.6\left(\frac{a}{W}\right)^4\right] \tag{7.5}$$

The dimensions of the specimen and the results are shown in Table 7.5

Table 7.5. K calculation by LEFM relation for CT specimen (ASTM E399-09).

Condition	B (mm)	W (mm)	a (mm)	a/W	P_Q (N)	f	K_Q (MPa$\sqrt{m}$)
Plane stress	2	26	8.8	0.338	2300	6.2	44.21

7.5. Calculation of the critical stress intensity factor using finite elements

Commercial finite element package Abaqus is used to model the specimen. Half of the specimen was modeled and the peak load obtained from DIC test was applied to the upper hole in the form of a concentrated force. A small part of the mid-plane with the length of the actual pre-crack (notch is modeled like its actual configuration) is set free to simulate crack and rest of the plane is constrained toward the movement along the direction of loading. The very last point of the model on the mid-plane along the crack is fixed in all direction to prevent unwanted body motion and rotation. CPS8 plane stress element is used and displacements for each node in loading direction (y) were extracted. The calculated displacement field is fit to Equation 4.1 with a Matlab code exactly like data from DIC. Results are shown below in Table 7.6.

Table 7.6. Specimen dimensions and critical stress intensity factors calculated from displacement field obtained using FE method.

Condition	B mm	W mm	a mm	a/W	r_{min}	r_{max}	K_I MPa$\sqrt{m}$	K_{II} MPa$\sqrt{m}$	T MPa	A_0	u_0
Plane stress	2	26	8.8	0.338	0.045	0.36	44.34	-10.8752	142.9328	-0.0016	-0.0013

Figure 7.12 shows node distribution and displacement field on the surface of specimen obtained from finite element analysis and Figure 7.13 illustrates the region on the surface of specimen with which the critical stress intensity factor is calculated. As shown in Table 7.6, this region is set to be same as the one in DIC analysis. In Figure 7.14, displacement contours on the surface of modeled specimen are shown. Solid lines indicate iso-displacement lines for actual data from finite element analysis which are fitted to find the constants in Equation 4.1 and dashed lines are the iso-

displacement lines drawn using coordinates of data points and the obtained constants plugged into equation 4.1. As it can be seen better fit is achieved for data from finite elements rather than data from actual tests. Comparing three calculated critical stress intensities shows a good match between three methods of calculations of critical stress intensity factor at the crack tip right before failure. Less than 3% deviation of results using DIC from other two methods gives a good certainty for the whole procedure and verifies that the same measurements can be applied to NiTi shape memory alloys.

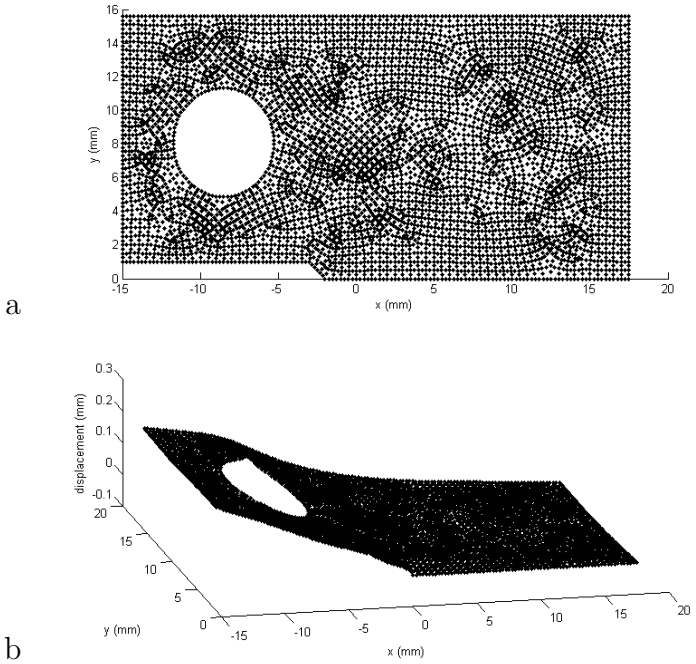

Figure 7.12. Node distribution (a) and displacement field (b) for Aluminum obtained using Finite elements.

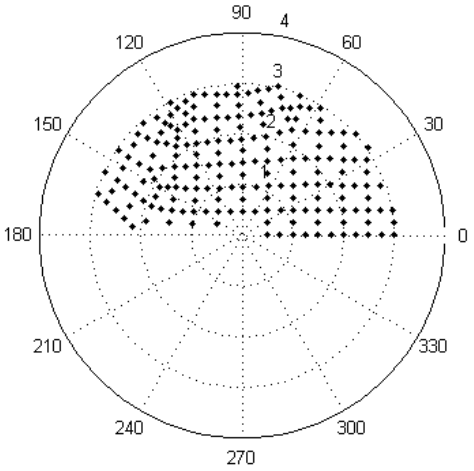

Figure 7.13. Filtered data region for calculation of critical stress intensity (Aluminum).

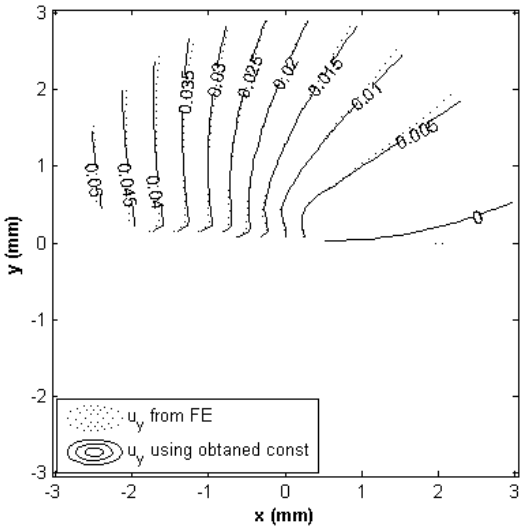

Figure 7.14. Displacement contours on the surface of the modeled specimen (Aluminum).

8. EVALUATION OF FRACTURE PARAMETERS OF NiTi SHAPE MEMORY ALLOY

8.1. Implementation of DIC method to NiTi

The CT specimen made from NiTi shape memory alloy cut by the electrical discharge machine (EDM) and L-T specimens are produced. Definition of L-T specimen on the rolled sheet is shown in Figure 8.1. Also the original NiTi sheet from which these specimens were cut from is shown in Figure 5.1.

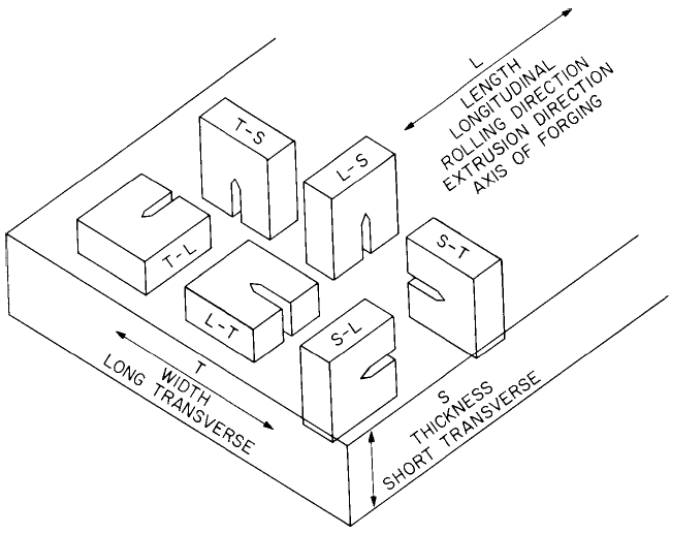

Figure 8.1. Definition of specimen directions on a rolled sheet.

The procedure was introduced in Section 4 and was implemented in section 7, and was validated by experiments and calculations in the case of aluminum.

Following the same procedure, experiments were done both at room temperature and at a higher temperature above the martensitic deformation temperature. Stepwise loading was done and after each step, the test was stopped and the related image from the surface of the specimen was taken. Figure 8.2 illustrates the configuration of the NiTi specimen that was used in experiments. This configuration is a modified form of what is introduced in ASME standard E399-09 [9].

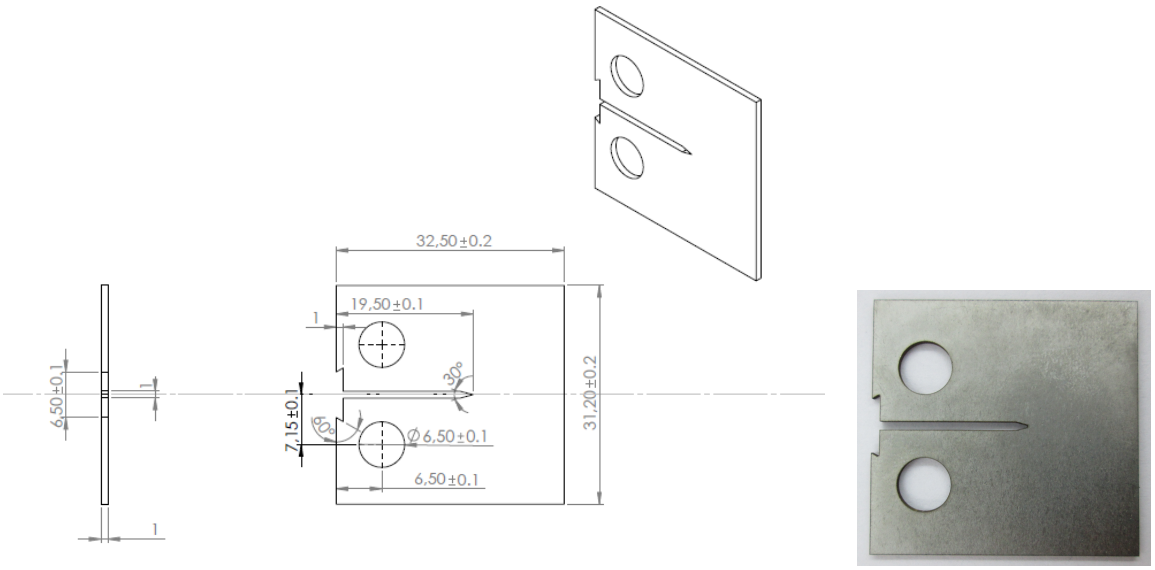

Figure 8.2. NiTi CT specimen configuration for fracture test.

Specimens were precracked using cyclic loading between 0 and 0.2 KN at a frequency of 5 Hz until an ideally sharp precrack with proper length of 2mm was obtained. The number of cycles differs from one specimen to another but for all specimen it remains between 8000 and 9000. Figure 8.3 shows sharp precrack combined with notch to create actual crack.

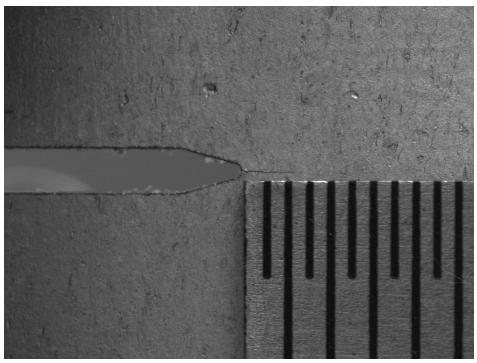

Figure 8.3. Ideally sharp crack obtained at the end of pre-cracking for NiTi specimen.

Two different lenses were used to obtain different fields of view to check if the type of lenses affects the DIC measurement. These lenses, which were installed on PIKE ALLIED Vision Technologies capturing CCD camera, are DOUBLE GAUSS 54690 50mm (EDMOND OPTICS) and COMPUTAR ZOOM LENS 18-108/2.5. The setup was exactly same as what was used for aluminum. In order to prevent any out of plane movement, four brass bushes were installed to fill the gap between the thickness of specimen and grips (8.4).

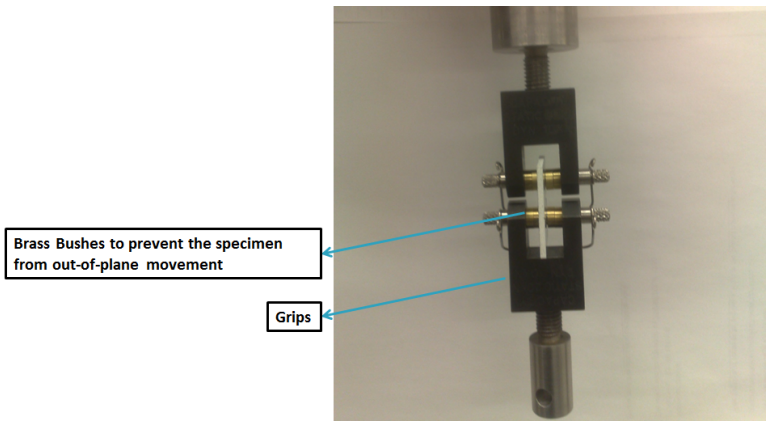

Figure 8.4. The use of brass bushes to limit the specimen's out-of-plane movement.

8.2. The results of the fracture test

Stepwise strain control loading was applied in the fracture tests. The displacement and load values associated with these incremental displacements are shown in Table 8.1. In Figure 8.8 it can be seen that the fracture occurs at load of 387.2 N after which a sudden drop in load is observed.

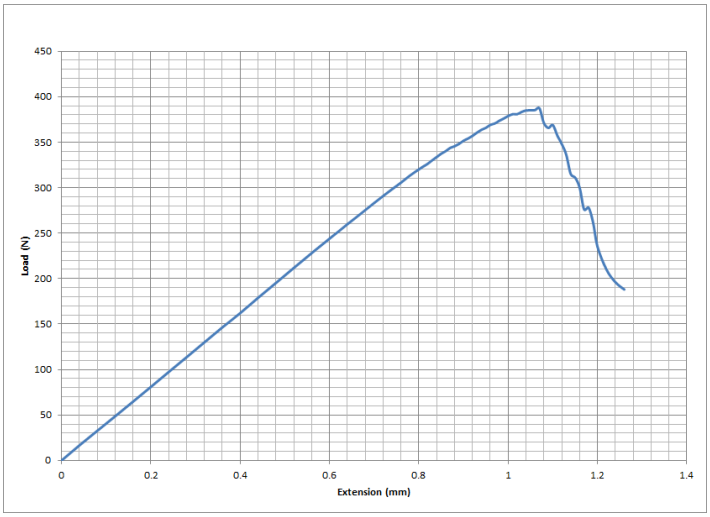

Figure 8.5. Load- displacement curve for NiTi in fracture test at room temperature.

Table 8.1. Displacement increments and associated loads in fracture test for NiTi CT specimen at room temperature.

Displacement (mm)	Load (N)	Displacement (mm)	load
0	0	0.45	351.6
0.02	16.6	0.455	354
0.04	32.6	0.46	356.9
0.06	48.6	0.465	360.5
0.08	64.7	0.47	363.6
0.1	80.9	0.475	365.8
0.12	97.3	0.48	369
0.14	113.6	0.485	370.6
0.16	130	0.49	373.5
0.18	146.3	0.495	376
0.2	162	0.5	378.8
0.22	178.9	0.505	380.8
0.24	195.2	0.51	380.8
0.26	211.7	0.515	383.2
0.28	228	0.52	384.9
0.3	243.9	0.525	385
0.31	251.8	0.53	385.3
0.32	259.8	0.535	387.2
0.33	267.5	0.54	371
0.34	275.3	0.545	365.7
0.35	283.1	0.55	368.8
0.36	290.8	0.555	357.3
0.37	298.3	0.56	348
0.38	305.5	0.565	336.1
0.39	313.3	0.57	315
0.4	320	0.575	311
0.405	323.3	0.58	300
0.41	326.3	0.585	276
0.415	330.1	0.59	278
0.42	333.7	0.595	262
0.425	337.3	0.6	235
0.43	340.1	0.61	210
0.435	343.7	0.62	196
0.44	345.5	0.63	188
0.445	348.1		

To perform DIC analysis, the undeformed image and the one associated to the force of 387.2 N were chosen. Images from the left side were captured using DOUBLE GAUSS 54690 50 mm (EDMOND OPTICS) lens and needed to be modifed before using the WinDIC software. These changes include horizontal flipping and cropping the desired region because the WinDIC software had problems with coordinates greater than 999 in x-direction and there are limitation due to the size of imported images. Final imported images are shown below:

a 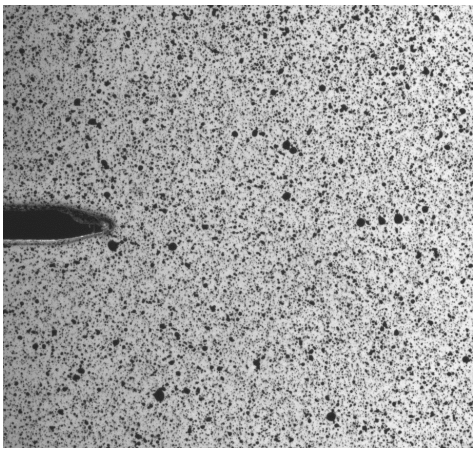 b 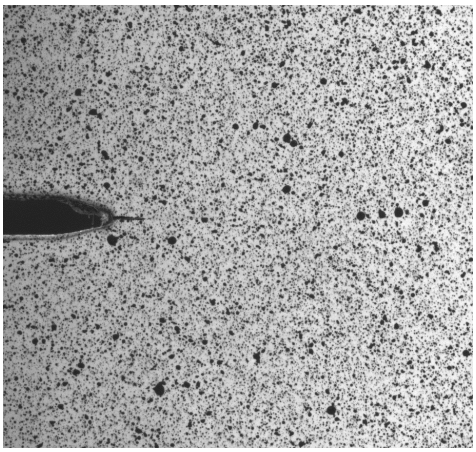

Figure 8.6. Modified undeformed(a) and deformed(b) images of NiTi CT specimen which were taken during the test at room temperature using DOUBLE GAUSS 54690 50mm lens and were imported to DIC analysis.

For the second specimen, Images taken using COMPUTAR ZOOM LENS 18-108/2.5 did not need flipping but the necessary size changes were applied (Fig 8.7).

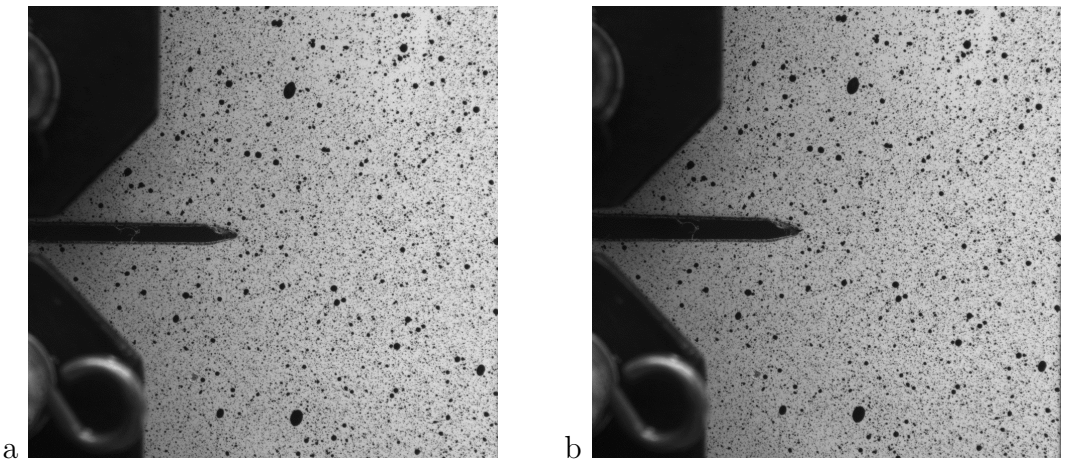

Figure 8.7. Undeformed and deformed images of NiTi CT specimen taken using COMPUTAR ZOOM LENS 18-108/2.5.

For the first lens, the modified images have the resolution of 916×864 pixels where 66 pixels are equal to 1 mm. Therefore its field of view is $13.87 \times 13.09\, mm \times mm$. For second lens the resolution is 935×900 pixels and 40 pixels represent 1 mm which means $23.37 \times 22.6\, mm \times mm$ field of view. Correlating these images, the displacement and strain field were extracted the same way as what was done for aluminum in Section 7. Fitting data to Equation 4.1 revealed that the magnitude of fracture parameters (K_I and K_{II}) are highly dependent on the place of coordinate system. At the first step, the origin placed on the tip of the precrack. Several data regions were taken into the consideration. Results are announced just for two cases, first to show that final values do not vary so much by choosing different areas which are small and close enough to the tip of the crack and secondly to avoid unnecessary information.

There is another parameter that plays a significant role on calculations. In literature it is mentioned that at the tip of the crack, austenite is fully transformed into

martensite and crack propagates in the martensitic region. Therefore it is suggested that material's elastic behavior at the tip of crack should be defined by martensitic elastic modulus. If the elastic modulus of the fully transformed martensite is used in calculations, the results will be as calculated in Table 8.2. Elastic modulus of fully transformed martensite was calculated as 14 GPa in section 5.

Table 8.2. K_I, K_{II}, T, A_0, u_0 inside mentioned boundaries (r_{min} and r_{max}) for both lens types using fully transformed martensitic elastic modulus of 14 GPa at the crack tip(NiTi CT specimen).

Lens type	COMPUTAR ZOOM LENS 18-108/2.5	COMPUTAR ZOOM LENS 18-108/2.5	DOUBLE GAUSS 54690 50mm	DOUBLE GAUSS 54690 50mm
r_{min}	0.04	0.01	0.04	0.01
r_{max}	0.3	0.4	0.3	0.4
K_I	10.87	11.38	11.68	12.03
K_{II}	0.40	0.66	-0.19	-0.16
T	98.46	126.7	63.49	88.59
A_0	-0.0039	-0.0038	-0.0040	-0.0040
u_0	0.2037	0.2038	0.2127	0.2127

As it will be seen in the next section, the values obtained are much less than the values that linear elastic fracture mechanics and finite element analysis predict. On the other hand, if elastic modulus of austenite were used as elastic behavior of material in fracture, results would be closer to those of other techniques. A similar assumption can be found in [46] where elastic modulus of austenite was chosen as the material property in calculations. In Table 8.3 results where an elastic modulus of 43 GPa was used are tabulated.

Table 8.3. K_I, K_{II}, T, A_0, u_0 inside mentioned boundaries (r_{min} and r_{max}) for both lens types using fully transformed martensitic elastic modulus of 43 GPa at the crack tip and with the orign of cartesian coordinate system on the tip of precrack.(NiTi CT specimen).

Lens type	COMPUTAR ZOOM LENS 18-108/2.5	COMPUTAR ZOOM LENS 18-108/2.5	DOUBLE GAUSS 54690 50mm	DOUBLE GAUSS 54690 50mm
r_{min}	0.04	0.01	0.04	0.01
r_{max}	0.3	0.4	0.3	0.4
K_I	33.4	34.97	35.89	36.96
K_{II}	1.25	2.04	-0.59	-0.51
T	302.42	389.16	195.02	272.11
A_0	-0.0039	-0.0038	-0.0040	-0.0040
u_0	0.2037	0.2038	0.2127	0.2127

It seems that the location of coordinate system plays an important role on calculated values of critical stress intensity factor. Therefore the location of the origin should be chosen wisely. In the previous case Cartesian coordinate systems origin was put at the tip of crack before loading. It means tip of the precrack in undeformed image. In another analysis, origin of the Cartesian coordinate system was put at the tip of the crack right before fracture which means at the tip of the crack in deformed image. Results are tabulated in Table 8.4. According to Table 8.4 and other set of analysis critical stress intensity was found to be $31 \pm 1\ MPa\sqrt{m}$.

Table 8.4. K_I, K_{II}, T, A_0, u_0 inside mentioned boundaries (r_{min} and r_{max}) for both lens types using fully transformed martensitic elastic modulus of 43 GPa at the crack tip and with the orign of cartesian coordinate system on the tip of crack at failure.(NiTi CT specimen).

Lens type	COMPUTAR ZOOM LENS 18-108/2.5	COMPUTAR ZOOM LENS 18-108/2.5	DOUBLE GAUSS 54690 50mm	DOUBLE GAUSS 54690 50mm
r_{min}	0.04	0.01	0.04	0.01
r_{max}	0.3	0.4	0.3	0.4
K_I	30.5	31.88	30.87	31.51
K_{II}	2.09	2.4	-1.5	-1.48
T	319.55	378.35	241.16	280.16
A_0	-0.0038	-0.0038	-0.0041	-0.0041
u_0	0.2023	0.2024	0.2101	0.2101

Displacement field and filtered region of data for DOUBLE GAUSS 54690 50mm lens, are shown in Figure 8.8 respectively. Figure 8.9 illustrates contour plots for actual data extracted from DIC where DOUBLE GAUSS 54690 50mm lens is used and those of which were obtained using equation 4.1 where five unknowns are replaced by the ones evaluated using the displacement fit.

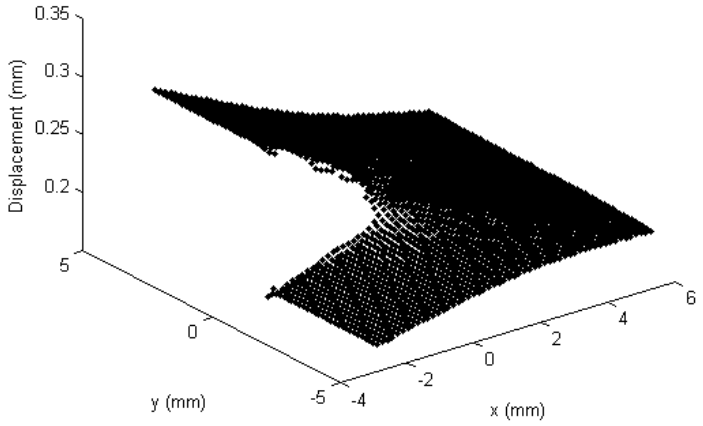

a

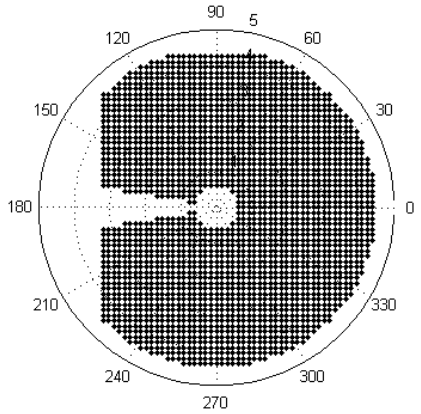

b

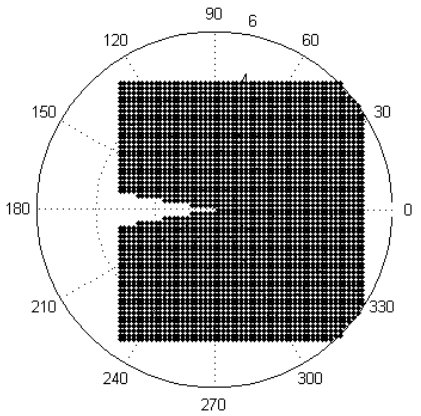

c

Figure 8.8. (a) displacement field around the crack tip (b) data region filtered by rmin=0.04 rmax=0.3 and (c) by rmin=0.01 rmax=0.4 for DOUBLE GAUSS 54690 50mm lens (NiTi CT specimen at room temperature).

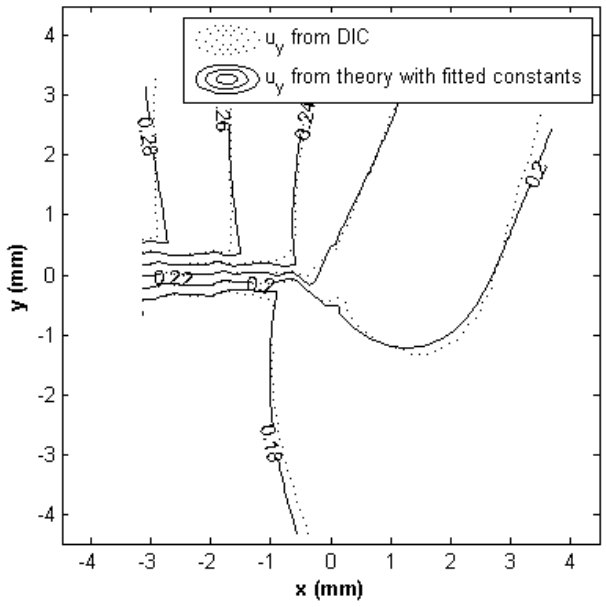

Figure 8.9. Displacement contours obtained using DIC technique (dashed lines)[DOUBLE GAUSS 54690 50mm lens] and calculated theoretically using Equation 4.1 with obtained K_I, K_{II}, T, A_0, u_0 substituted in the equation (solid lines).

Figure 8.10 and 8.11 are similar plots as previous ones except this time COMPUTAR ZOOM LENS 18-108/2.5 lens was used.

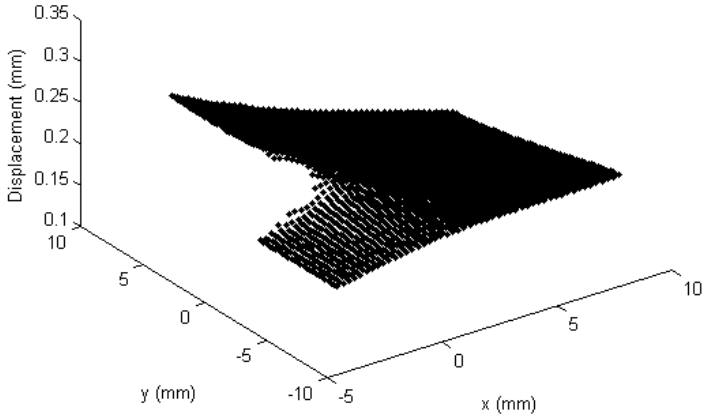

a

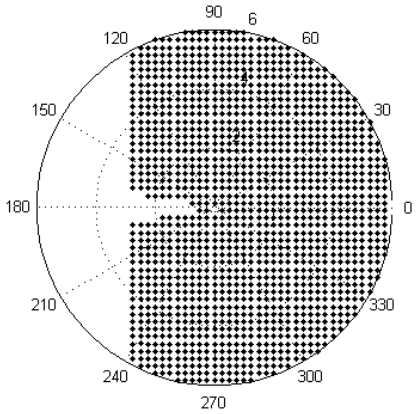

b

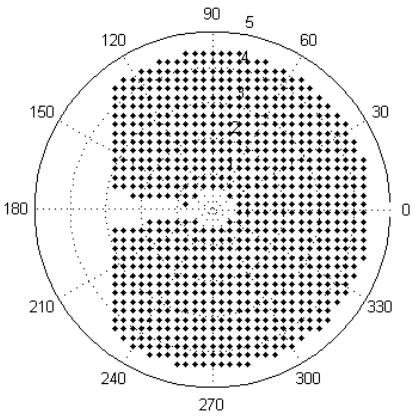

c

Figure 8.10. (a) Displacement field around the crack tip at room temperature (b) data region filtered to rmin=0.04 rmax=0.3 and (c) to rmin=0.01 rmax=0.4 (COMPUTAR ZOOM LENS 18-108/2.5 lens).

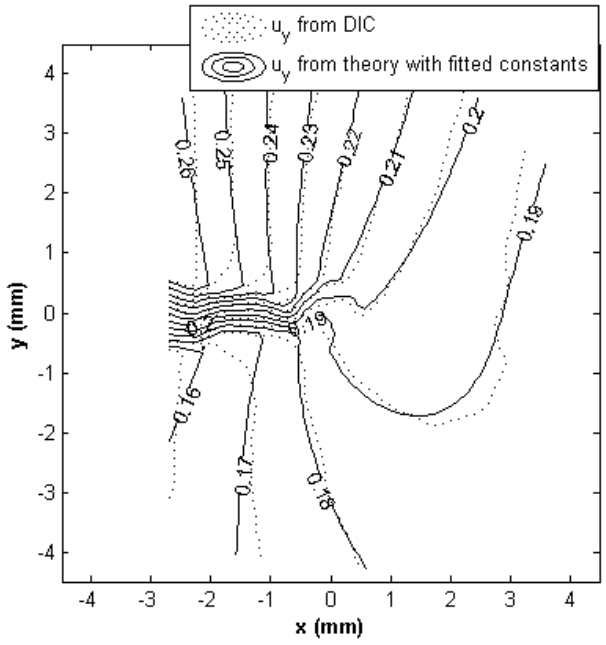

Figure 8.11. Displacement contour plot for data from DIC technique (dashed lines) and those calculated theoretically using equation 4.1 with the obtained constants replaced in the equation (solid lines) for COMPUTAR ZOOM LENS 18-108/2.5 lens (NiTi CT specimen at room temperature).

8.3. Calculation of critical stress intensity factor using LEFM

If we assume that the plastic zone around the crack tip is very small compared to the size of the specimen, then linear elastic fracture mechanics relations can be used for estimation of fracture behavior. With this assumption, and referring to ASTM E399-09, critical stress intensity factor for this case can be calculated. Although this standard requires that load-displacement curve should be plotted using displacement values that are read from strain gage at crack mouth (CMOD), it is also safe enough to read displacement from machine's cross-head because it has no effect on value of P_Q and in calculations there is nothing associated with the area under the curve. For the

load- extension curve in Figure 8.12 a 5% secant line was traced to find P_Q and the critical stress intensity factor was calculated using the load at the intersection of the curve and the secant line which was found to be 380 N.

In Table 8.5 critical stress intensity factors calculated for NiTi shape memory alloy at room temperature are tabulated.

Table 8.5. Critical stress intensity factor calculated using LEFM for NiTi CT specimen at room temperature.

Condition	B mm	W mm	a mm	a/W	P_Q N	f	K_Q MPa$\sqrt{m}$
Plane stress	1	26	13±2=15	0.577	380	12.51	29.471

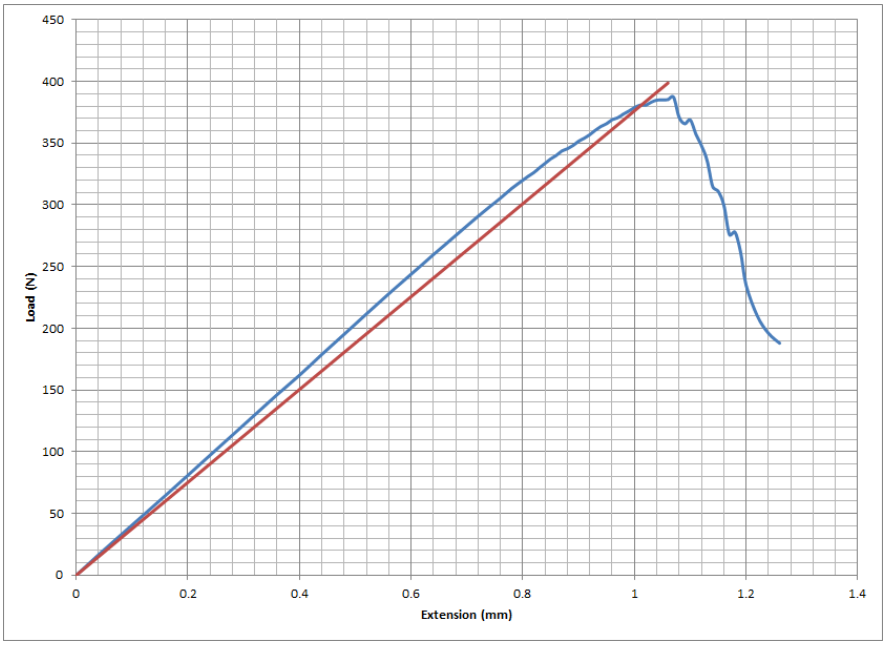

Figure 8.12. Load-crosshead extension curve for NiTi CT specimen at room temperature (5% secant line used for P_Q).

8.4. Finite element analysis of edge cracked NiTi at room temperature

Finite elementsis used to validate experimental results. In the case of aluminum, a good agreement was achieved when both methods for extracting displacement field (DIC and FE) left similar critical stress intensity values. The results which were satisfactorily close to those ones predicted by LEFM were enough for validation of the method and the capability of DIC to be used together with Equation 4.1. ABAQUS was used and half of NiTi specimen was modeled and mechanical properties obtained from displacement-controlled uniaxial tension test were used as input. Plane stress mode was used and an ideally sharp crack was defined to represent actual precracked specimen. The geometry of the problem is shown in Figure 8.2.

Specimen was subjected to a concentrated load of 380N at the top of the hole and the

crack plane was constrained both in-plane directions from the tip of the crack to the end point of specimen in that part of the body which does not have a notch. ABAQUS's UMAT for superelastic shape memory alloy was used to model the material behavior. Superelastic behavior input data was based on the uni-axial behavior of material and shown in the next page.

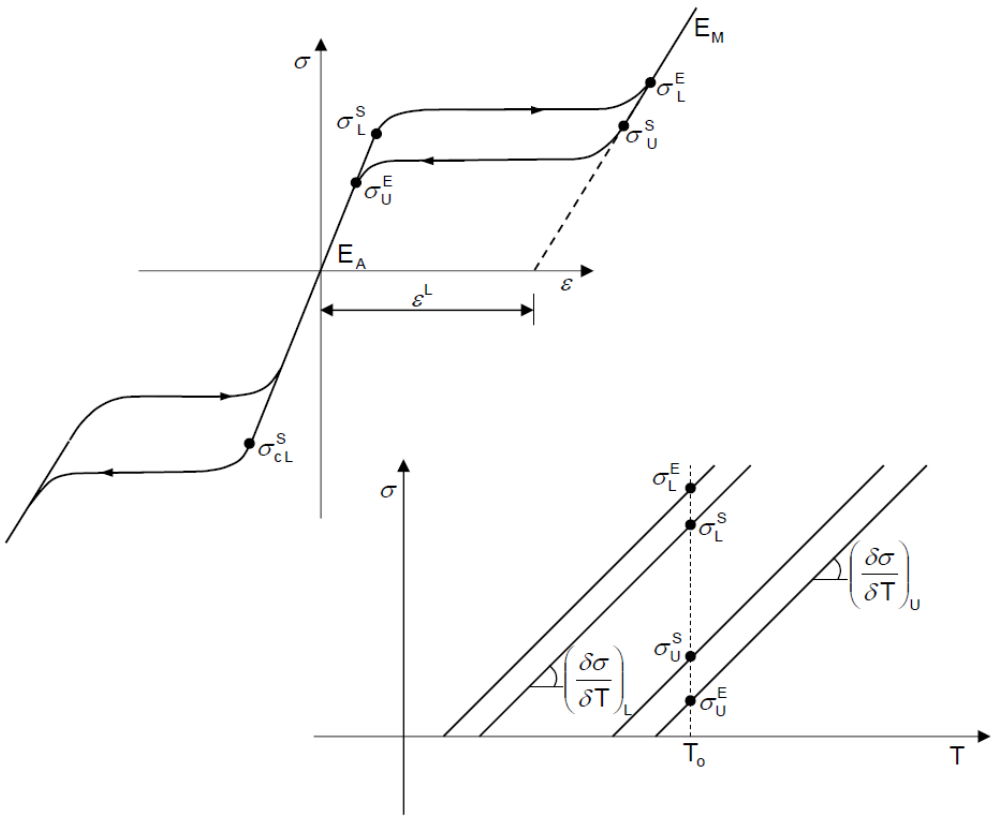

Figure 8.13. Definition of input data to define superelasticity by UMAT.

where E_A is Young's modulus (austenite), E_M is Young's modulus (martensite), K_I is Stress intensity factor (applied), T_0 is Reference temperature, $\left(\frac{\delta\sigma}{\delta T}\right)_L$ is Rate of stress increase with change in temperature during loading, ε^L is Transformation strain, ε_V^L is Volumetric transformation strain, ε_{pt} is Strain at which phase transformation

occurs, ε_{sat} is Strain at which saturation occurs, σ_L^S is Stress at the start of transformation during loading, σ_L^E is Stress at the end of transformation during loading, σ_U^S is Stress at the start of transformation during unloading, σ_U^E is Stress at the end of transformation during unloading, ν_A is Poisson's ratio (austenite), ν_M is Poisson's ratio (martensite), α is Pressure sensitivity parameter

Displacement field was extracted as output and was fitted to Equation 4.1. Results are listed below:

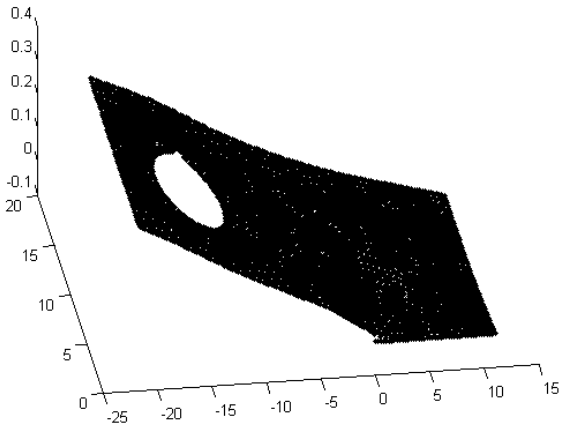

Figure 8.14. Displacement field for NiTi obtained by Finite element with the origin at the tip of pre-crack (RT).

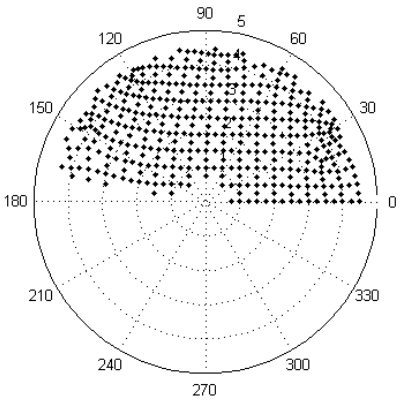

Figure 8.15. Filtered region for calculation of critical stress intensity factor with the origin at the tip of the pre-crack (RT).

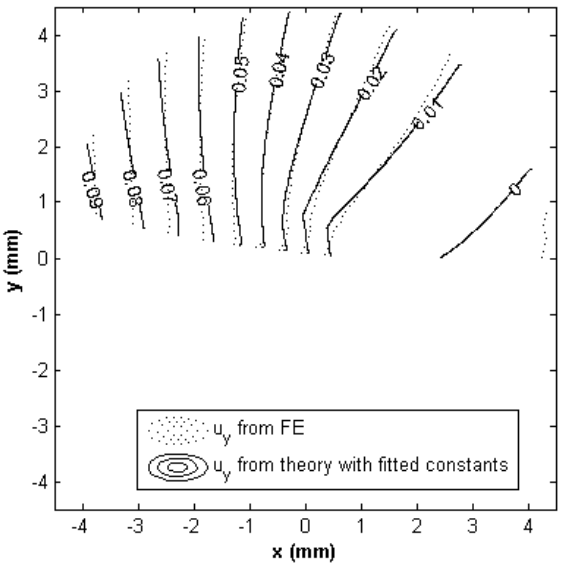

Figure 8.16. Displacement contours on the surface of the modeled specimen with the origin at the tip of the pre-crack (RT).

Table 8.6. Critical stress intensity calculation using FE analysis for NiTi CT specimen at room temperature with the origin on the tip of the pre-crack.

Condition	B mm	W mm	a mm	a/W	r_{min}	r_{max}	K_I MPa$\sqrt{m}$	K_{II} MPa$\sqrt{m}$	T MPa	A_0	u_0
Plane stress	1	26	15	0.577	0.04	0.3	36.33	-2.79	-256.79	-0.002	0.0031

Stress intensity factor that was calculated with this model (36.33 $MPa\sqrt{m}$) was in a good agreement with the one that was obtained from DIC (35±2 $MPa\sqrt{m}$).
If the origin of the Cartesian coordinate system is placed on the tip of the crack at failure (found by DIC analysis), interesting results would be obtained:

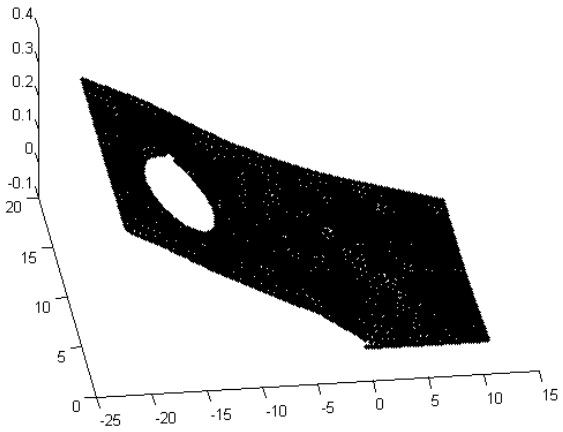

Figure 8.17. Displacement field for NiTi obtained by Finite element with the origin on the tip of crack at failure (RT).

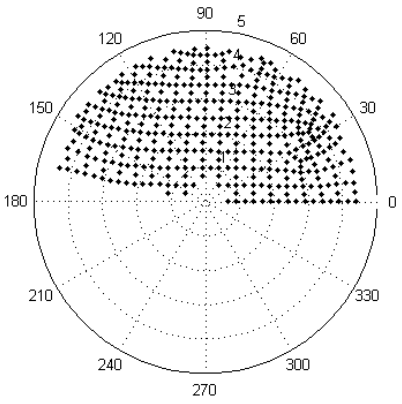

Figure 8.18. Filtered region for calculation of critical stress intensity with the origin on the tip of crack at failure (RT).

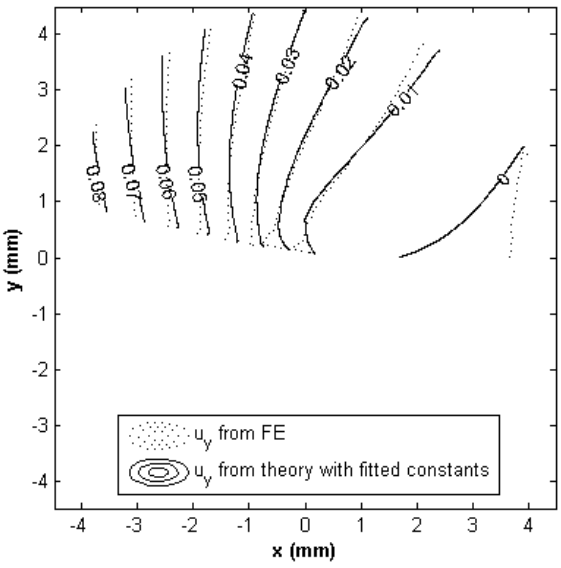

Figure 8.19. Displacement contours on the surface of the modeled specimen With the origin on the tip of crack at failure (RT).

Table 8.7. Critical stress intensity calculation using FE analysis for NiTi CT specimen at room temperature with the origin on the tip of crack at failure (RT).

Condition	B mm	W mm	a mm	a/W	r_{min}	r_{max}	K_I MPa$\sqrt{m}$	K_{II} MPa$\sqrt{m}$	T MPa	A_0	u_0
Plane stress	1	26	15	0.577	0.04	0.3	31.5	-2.53	54.61	-0.0051	0.0050

Very close matching can also be seen there when origin is located at the tip of crack at failure. A critical stress intensity factor of 31.50 $MPa\sqrt{m}$ by finite elements admits that the choice of the origin at the tip of crack at failure instead of at pre-crack; and applying 43 MPa as material's modulus of elasticity, gives a result very close 31 ± 1 $MPa\sqrt{m}$ that was obtained from DIC and 29.47 $MPa\sqrt{m}$ that was obtained by LEFM.

8.5. Experiments at a temperature above M_d

8.5.1. Tension test above M_d

The properties of the material at room temperature have been explained in Section 5. In order to explore the effect of martensitic transformation on the fracture properties of NiTi shape memory alloys, the this transformation is prevented from happening. This is done by raising the temperature to above martensitic deformation temperature M_d. Reaching and crossing this temperature will suppress the martensitic transformation [39]. Tensile test is done at high this temperature (approximately 100 °C) to obtain the material's property when it is subjected to a loading where there is no transformation. High temperature air flow on the surface of specimen provided the desired test temperature throughout the operation. Thermal camera, which was

added to the test setup, made it possible to track the temprature at the surface of the body and ensured that the temperature remains around 100 °C. Series of tests were done using 100 KN Instron testing machine which has strong grips thet prevent slipping. Loading rate was chosen to be 3 mm/min. These tests make sure that the transformation does not take place at this temperature. Figure 8.20 illustrates the setup which was used to do this test and Figure 8.21 shows stress-strain curves obtained from tensile test. In the first test (a) specimen was pulled up to 2.2% strain and then unloaded. In the second one (b), specimen was loaded to 2.5% strain then unloaded at the same rate. Both tests show that the unloading line traces a path parallel to the loading one and residual plastic deformation is observed at the end of full unloading. This demonstrates that martensitic phase transformation did not happen during loading.

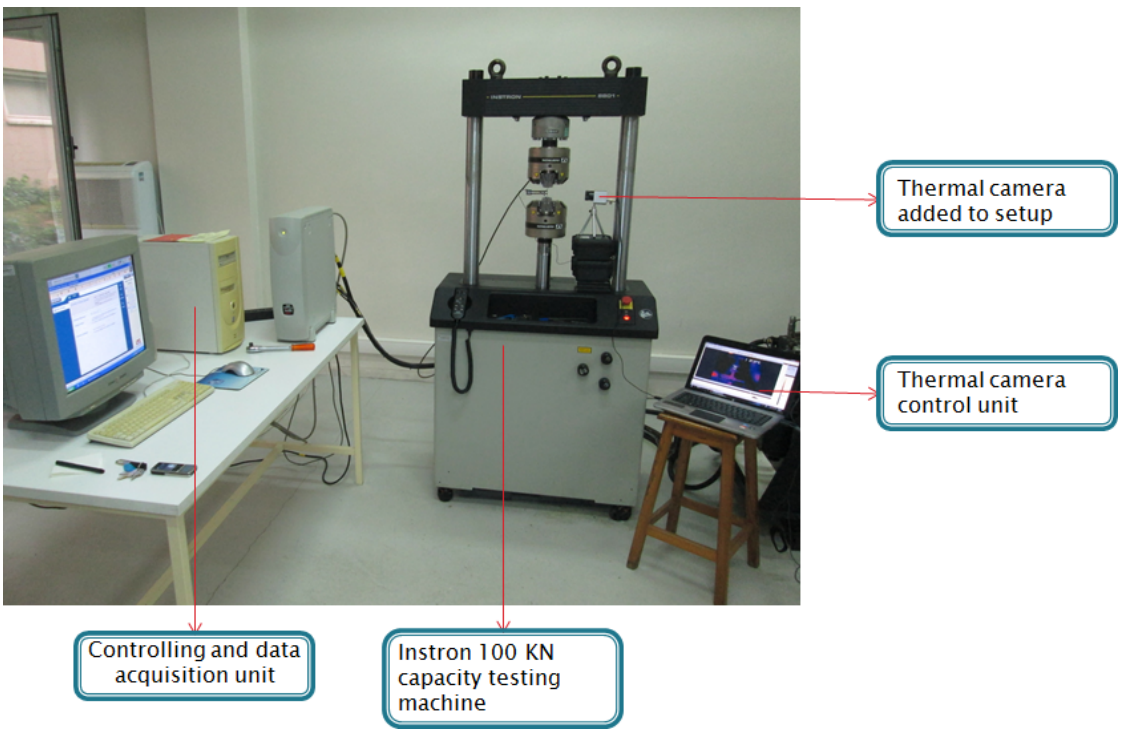

Figure 8.20. Test setup for tensile test at a temperature above Md in TD.

a

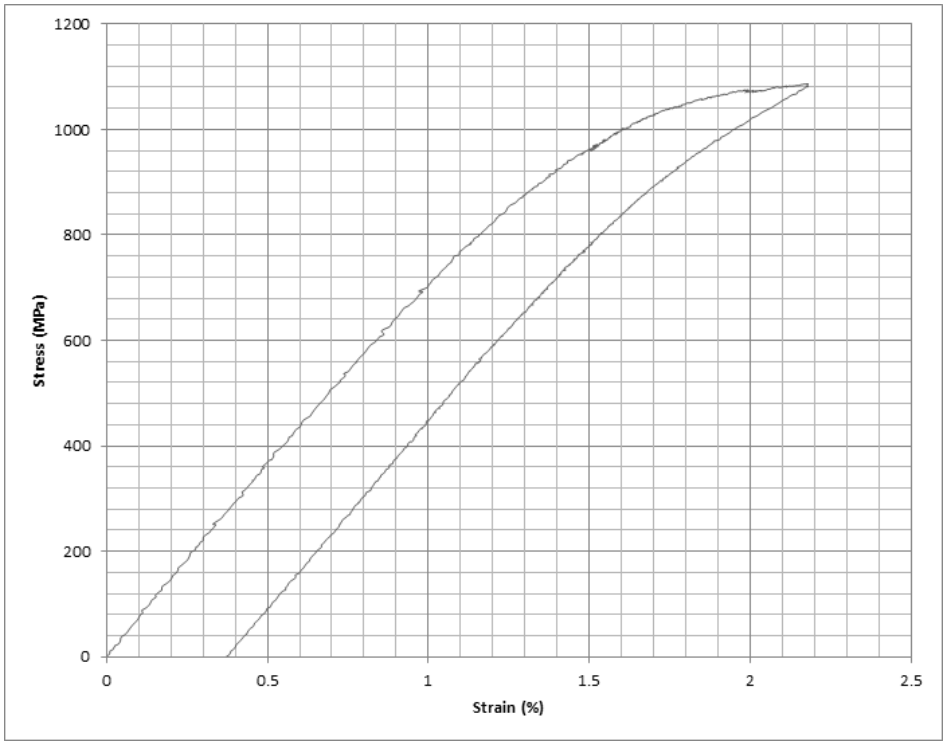

b

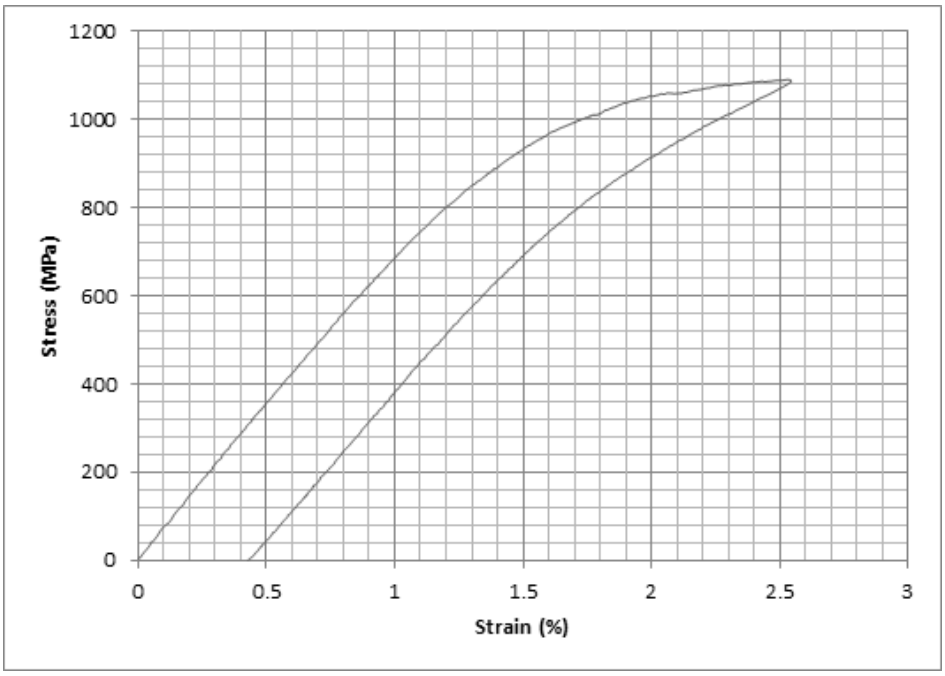

Figure 8.21. Stress -strain curves for NiTi shape memory alloy at 100 °C (temperature above M_d) using 100KN Instron with a loading rate of 5 mm/min.

Same as what was concluded when the results for different loading rates were compared. Here the material's response even in the case of elastic behavior of austenite differs when temperature changes. The slope of stress-strain curve changed drastically and material responded to loading by an elastic modulus of 70 GPa in the elastic region. This is by far greater than what was obtained a room temperature. Table 8.8 shows the results of 3 tests.

Table 8.8. Results of tensile test for NiTi shape memory alloy at 100 °C (above M_d).

	Pulling Direction	E_A (GPa)	Ultimate Tensile Strength (MPa)
Test 1	TD	71	——-
Test 2	TD	70	——-
Test 3	TD	70	1262

8.5.2. Test procedure

The procedure that was applied in the previous chapter, was applied to the same NiTi specimen with same composition and configuration but at a temperature above M_d to prevent martensitic transformation from occurring. To make sure that environmental factors and other factors like camera properties do not affect experiments, two cameras were used to capture the specimen from both sides while loading. Both sides of the specimen were painted with small differences in speckles' size. Thermal camera was added to the setup to measure the temperature at the surface of the specimen to make sure that specimen remains at desired test temperature (above 100 °C) during the experiment. Stepwise loading by incremental increase in crosshead extension is plotted and is illustrated in Figure 8.22. Like the experiment at room temperature,

5% secant with the 0.95 slope of linear portion, is traced to obtain P_Q. According to Figure 8.22 P_Q was found to be 434 N. Data are tabulated in Table 8.9 and the test setup is shown in Figure 8.23.

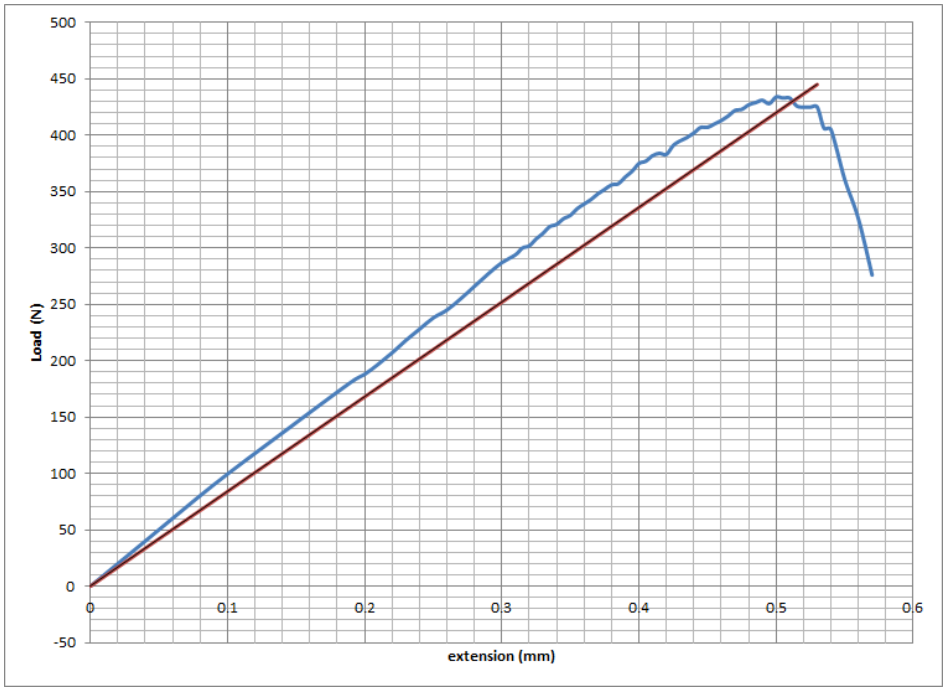

Figure 8.22. Load-extension curve for NiTi at 100 °C (above M_d).

Table 8.9. Load- displacement data obtained from DIC for NiTi at the temperature above M_d.

Displacement (mm)	Load (N)	Displacement (mm)	load
0	0	0.395	368
0.02	20	0.4	375
0.04	40	0.405	377
0.09	90	0.41	382
0.14	136	0.415	384
0.19	181	0.42	383
0.2	188	0.425	391
0.21	197	0.43	395
0.22	207	0.435	398
0.23	218	0.44	402
0.24	228	0.445	407
0.25	238	0.45	407
0.26	245	0.455	410
0.27	255	0.46	413
0.28	266	0.465	417
0.29	277	0.47	422
0.3	287	0.475	423
0.31	294	0.48	427
0.315	300	0.485	429
0.32	302	0.49	431
0.325	308	0.495	428
0.33	313	0.5	434
0.335	319	0.505	433
0.34	321	0.51	433
0.345	326	0.515	426
0.35	329	0.52	425
0.355	335	0.525	425
0.36	339	0.53	425
0.365	343	0.535	406
0.37	348	0.54	405
0.375	352	0.55	361
0.38	356	0.56	326
0.385	357	0.57	276
0.39	363		

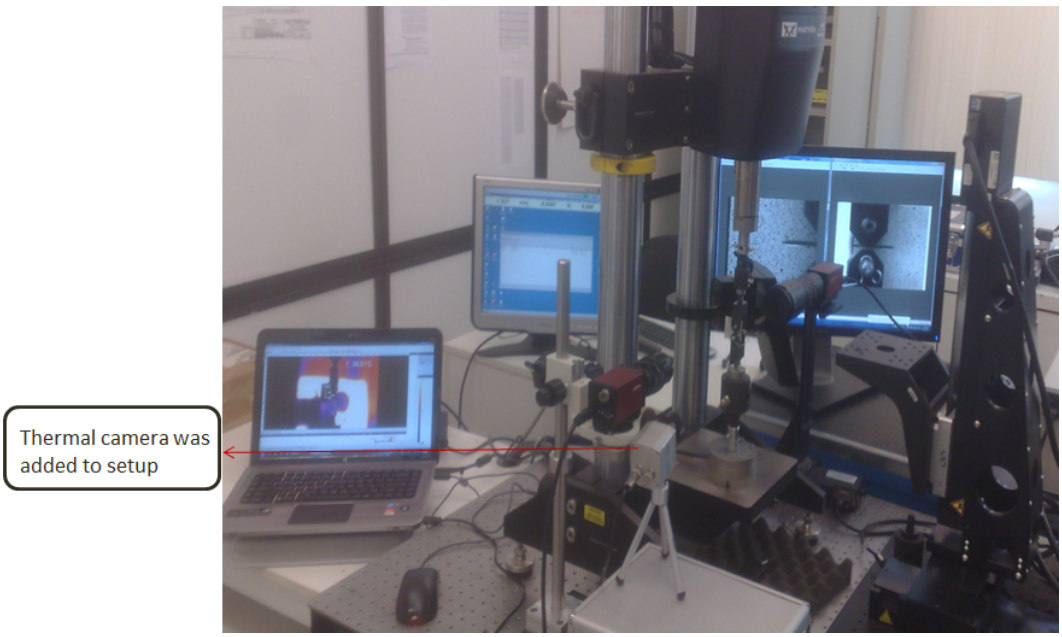

Figure 8.23. Test setup for DIC at temperature above M_d.

Austenite elastic modulus was set to be 70GPa as was obtained in previous section for tensile test specimen at 100 °C. Data region and calculated results are shown in Table 8.10. Figure 8.24 illustrates displacement contours for data that were obtained from DIC and the one calculated using Equation 4.1 using constants calculated. Like in previous cases a good agreement between these two contours are achieved. Figure 8.25 contains displacement field and filtered data region.

Table 8.10. K_I, K_{II}, T, A_0, u_0 from data inside mentioned boundaries (r_{min} and r_{max}) using an austenitic elastic modulus of 70 GPa (HT).

Lens type	DOUBLE GAUSS 54690 50mm	DOUBLE GAUSS 54690 50mm
r_{min}	0.04	0.01
r_{max}	0.3	0.4
K_I	35.53	36.17
K_{II}	-0.95	-1.01
T	599.51	638.39
A_0	-0.0019	-0.0020
u_0	0.3306	0.3306

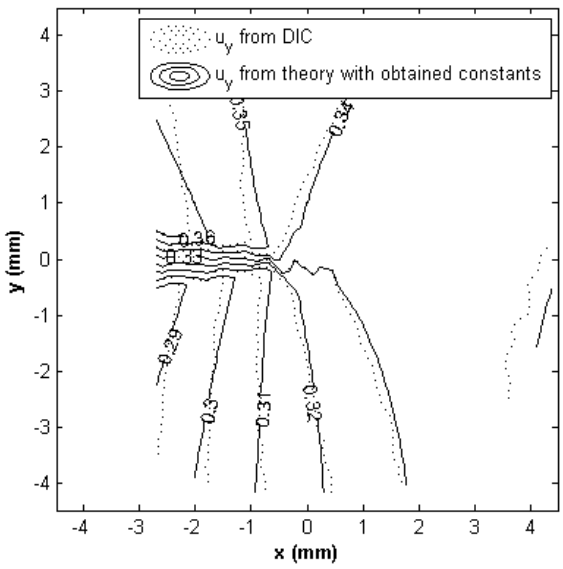

Figure 8.24. Displacement contours from actual data measured by DIC (dashed lines) and from 4.1 using obtained constants (solid lines) (HT).

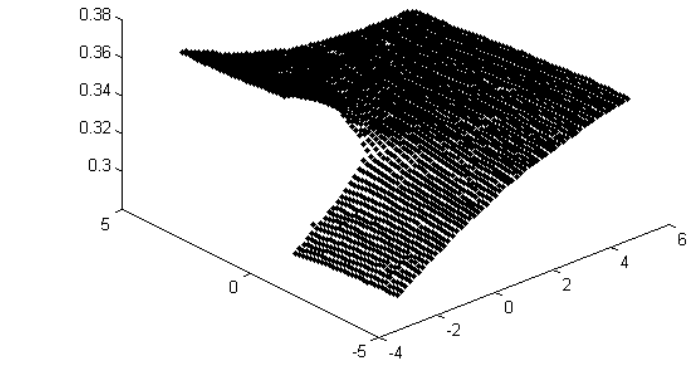

a

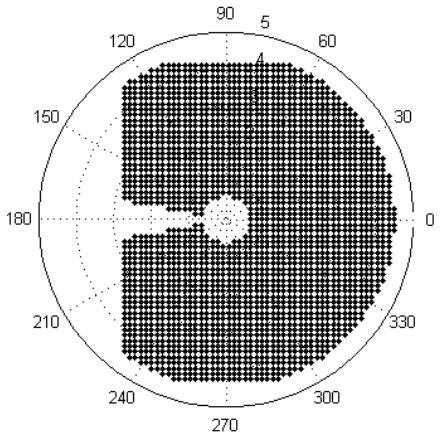

b

Figure 8.25. Displacement field (a) and filtered data region (b) for NiTi with r_{min}=0.03 and r_{max}=0.4 using DOUBLE GAUSS 54690 50mm lens at temperature at 100 °C.

The critical stress intensity was calculated to be 35±2 $MPa\sqrt{m}$ which is surprisingly higher than the one obtained in experiments at room temperature.

8.6. Calculation of critical stress intensity factor using LEFM at a temperature above M_d

To have a better understanding about this increase in K, LEFM was used as an alternative calculation method and the results obtained are tabulated in Ttable 8.11. This approach admits that toughness increased like what DIC results told previously.

Table 8.11. Critical stress intensity factor calculated using LEFM for NiTi CT specimen at 100 °C.

Condition	B mm	W mm	a mm	a/W	P_Q N	f	K_Q MPa$\sqrt{m}$
Plane stress	1	26	13±1.9=14.9	0.537	434	12.33	33.2

Two possible explanations come to mind at this point. One is that toughness actually decreases when martensitic phase transformation occurs. This was reported in works which were briefly explained in section 3 e.g. [17] and present work is an experimental prove for them. Another comment on this unexpected result is because of the nature of loading which was stepwise where after each step some time was needed to record the amount of load and displacement besides saving associated image at higher temperature; pausing the experiment under constant load even for a short while at high temperature, could have possibly caused the material to have enough time for relaxation. This is the moment when crack blunting started and this occurred at each time interval. This means plasticity increased and slip dislocation mechanisms became active. On the other hand, higher temperatures lower material's elastic constants and can induce plasticity in traditional metals. This is can be a reason for the results obtained. Further investigation is needed to clarify the main reason behind this behavior

of NiTi shape memory alloy with this composition and material properties.

8.7. Finite element analysis of NiTi a temperature above M_d

Exactly the same geometry that was used to model the experiment at room temperature, was implemented to model NiTi shape memory alloy at a temperature above M_d. The difference is that in this case material needed not be modeled using UMAT. For this case martensitic phase transformation did not occur and the material could be modeled as a material with an elastic modulus of 70 GPa which was found in uniaxial tension test at 100 °C. Boundary conditions were the same as in the previous case and a concentrated load of 434 N obtained during fracture test was applied. Table 8.12 tabulates results from ABAQUS.

Table 8.12. Critical stress intensity factor using FE analysis for NiTi CT specimen at 100 °C with origin at the tip of the crack at failure.

Condition	B mm	W mm	a mm	a/W	r_{min}	r_{max}	K_I MPa$\sqrt{m}$	K_{II} MPa$\sqrt{m}$	T MPa	A_0	u_0
Plane stress	1	26	15	0.577	0.04	0.3	34.5	-2.53	77.59	-0.0030	-0.0034

It can be seen that in the case of loading the NiTi at the temperature above the martensitic deformation M_d, the proposed method gives relatively same values for critical stress intensity factor. Calculated values of critical stress intensity factors were 35±2 $MPa\sqrt{m}$, 33.2 $MPa\sqrt{m}$ and 34.5 $MPa\sqrt{m}$ by implementing DIC method, LEFM and FE respectively which are very close and all of them show the same amount

of increase when compared to values obtained from experiments at room temperature which were 31±1 $MPa\sqrt{m}$ from DIC, 29.47 $MPa\sqrt{m}$ by LEFM and 31.50 $MPa\sqrt{m}$ by FE. These results lead to the conclusion that at the temperature above the M_d , toughness increased despite martensitic phase formed in negligible amount or did not appeared at all.

8.8. Estimation of transformation zone using DIC

The stress-strain curve for NiTi shape memory alloy at room temperature has three distinct regions: elastic deformation of austenite, a stress plateau, where phase transformation from single oriented austenite to detwinned martensite occurs, and elastic deformation of fully transformed martensite. If the strain is taken as the controlling parameter, there will be two characteristic strains on the stress strain curve. One is the strain needed to initiate phase transformation and the other is the strain at which the transformation process ends. In fact the latter can be a tool to estimate of the size of the transformation zone. If the location where this strain is achieved in the surface of specimen is known, then we can approximate it as the boundary of the transformation zone. Figure 8.26 is an illustration of the strain which is needed for NiTi to be fully transformed when it is subjected to loading in rolling direction.

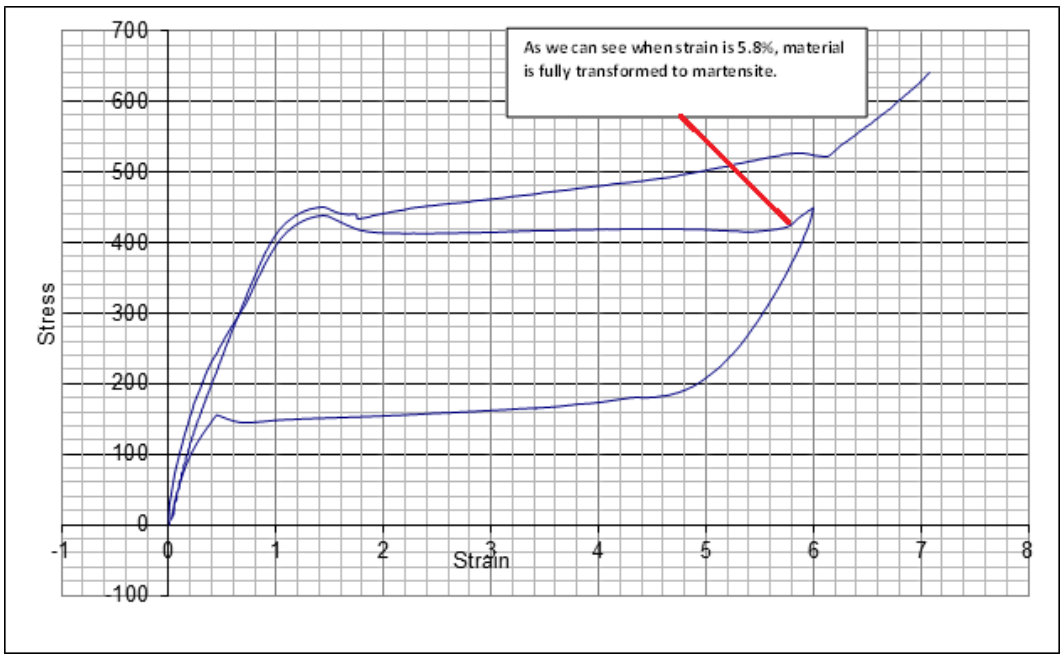

Figure 8.26. Stress-strain curve for NiTi pulled in RD at room temperature.

Therefore if we determine the location where this amount of strain is reported on the surface of CT specimen using DIC technique, we can conclude that any region between this point and the tip of crack contains at least some austenite. Now if we look at the full-field quantitative strain distribution in the vicinity of the crack tip and plot it, we can obtain the size of fully transformed martensite zone along crack plane. Figure 8.8 shows strain field around the crack tip for NiTi at room temperature.

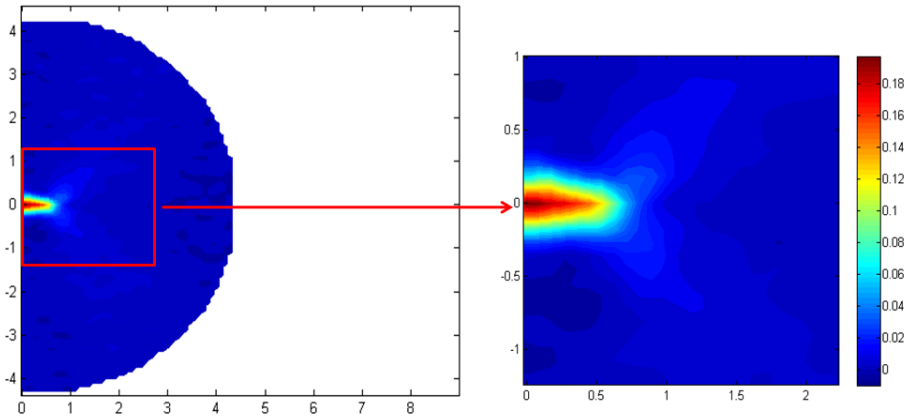

Figure 8.27. Full-field strain distribution in the direction of loading for NiTi obtained by DIC at room temperature (left) and closer view of strain field around the crack tip at the right.

The shape of the martensitic transformation zone at the onset of crack growth can be characterized by three regions: one region starts from the tip of crack and extends along the crack plane and is named as fracture process zone. The other two lobes that start from the end of fracture process zone and develop along directions that make approximately 60° with plane of the crack on both sides. A similar distribution was reported by Daly, *et al.* [7]. Now if one looks closer to the distribution, it can be estimated that 5.8% strain occurs at around x=0.72 mm which in this case represents the transformation zone size on the x axis (θ=0). To compare to other works which calculated transformation zone size, a work by Carmine Maletta , Franco Furgiuele [30], was recalled. They manipulated Irwine's modification on linear elastic fracture mechanics to establish an analytical method that could predict the extent of the transformation region in the vicinity of a crack tip. Their method has been validated by comparing the result to the ones which were obtained by numerical simulation using commercial finite element package. They suggest equation 8.1 for calculation of transformation zone [30].

$$r_M = \frac{1}{2\pi}\left(\frac{2(1-\nu)K_{Ie}}{(2(1-\nu)\sigma^{tr} + \varepsilon_L E_A)}\right)^2 \tag{8.1}$$

where

ν is Poisson's ratio = 0.3

K_{Ie} is the effective stress intensity factor and from DIC and is about 31 $MPa\sqrt{m}$

σ^{tr} is the transformation stress where graph starts to deviate from linearity

ε_L notional permeability factor

E_A is the martensite elastic modulus

(austenitic elastic modulus was replaced due to results obtained in section 8)

Figure 8.28 shows parameters used in Equation 8.1 on stress-strain curve for NiTi shape memory alloy.

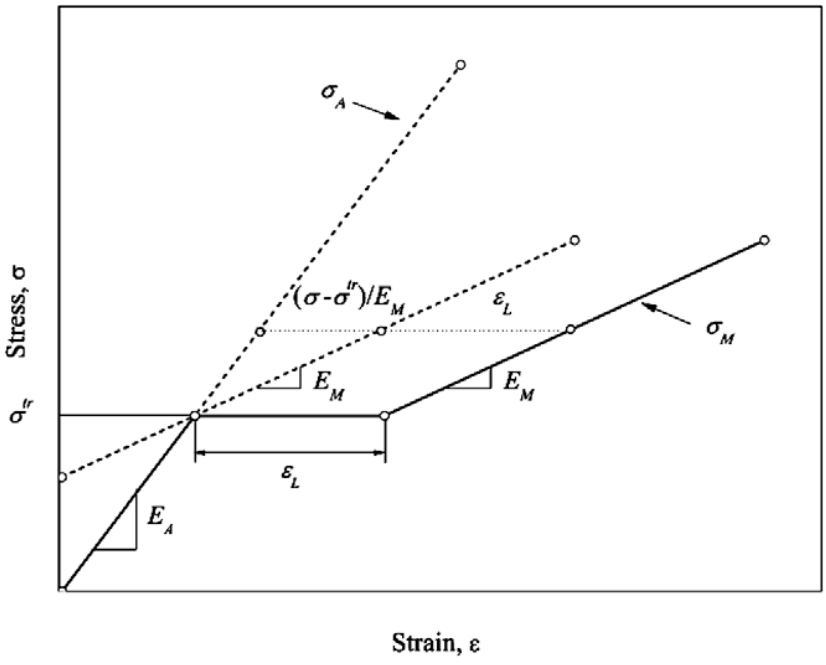

Figure 8.28. Schematic stress-strain curve for NiTi shape memory alloy which has parameters of equation 1 on it [30].

Plugging those values in Equation 8.1 gives:

$$r_M = \frac{1}{2\pi}\left(\frac{2\,(1-0.3)\,30\,MPa\sqrt{m}}{2\,(1-0.3)\,415\,MPa + 0.045\times 14\,MPa}\right)^2 \times 1000\,mm/m = 0.826\,mm$$

Two methods show an approximate difference of 18% at the end.

If we simply estimate martensitic zone to be the same as plastic zone in ordinary material like what was assumed in many works, it will yield a martensitic transformation size as follows:

$$r_M = \frac{1}{2\pi}\left(\frac{K_{Ie}}{\sigma^{tr}}\right)^2 = 0.888\,mm$$

Which as it was expected deviated from the experimental result.

8.9. Summary and Conclusions

In this work, digital image correlation was used to obtain full-field displacement with which the critical stress for an edge-cracked specimen was calculated. Displacement field was fitted to the Eq 4.1 which is also based on linear elastic fracture mechanics. LEFM calculation of critical stress intensity factor and Finite element analysis besides the result from DIC measurements revealed that a good match can be obtained if two conditions are satisfied. First, it was found that NiTi's fracture behavior does not depend on local elastic properties of fully transformed material. It was illustrated that general parent elastic behavior of the material governs its fracture behavior. It can also be inferred that even if it is assumed that local elastic properties of the material are the governing properties, then the actual elastic modulus of the martensite is supposed to be higher than what is obtained for the fully transformed material with the tensile test. The second observation is that in all calculations, the crack length at the moment of fracture should be chosen as the actual crack size. The crack size after pre-cracking and before loading does not represent the real crack size.

The experiments at the temperature above M_d demonstrate an increase in both critical stress intensity factor and the fracture toughness at the specified thickness. This result was validated by FE results and fracture equations based on LEFM.

Finally, an experimental estimation of the transformation zone was carried out based on DIC measurements. Although the estimated transformation zone differs from

the theoretical calculations done by Maletta, *et al.* by 18-20 % , it is closer to the theoretical calculations than other experimental estimations [38]. Calculations was also done using two assumptions mentioned above; austenitic elastic modulus is used as elastic property of material at fracture and crack length at the moment of fracture was used as actual crack length. Although these prediction about the behavior of NiTi subjected to fracture, its local and general elastic properties and also the effect of martensitic phase transformation are investigated to some extents, but it seems that extra work containing more experiments are needed in the field of fracture in the future.

REFERENCES

1. Baxevanis T., Y. Chemisky and D. C. Lagoudas, "Finite Element Analysis of The Plane Strain Crack-Tip Mechanical Fields in Pseudoelastic Shape Memory Alloys", *Smart Materials and Structures*, Vol. 21, No. 9, 2012.

2. Birman V., "On Mode I Fracture of Shape Memory Alloy Plates", *Smart Materials and Structures*, Vol. 7, No. 4, p. 433, 1998.

3. Chen J. H., G. Z. Wang and W. Sun, "Investigation on the Fracture Behavior of Shape Memory Alloy NiTi", *Metallurgical and Materials Transactions,* Vol. 36A, No. 4, pp. 941-955, 2005.

4. Chen W. W. and B. Song, "Dynamic Characterization of Soft Materials", *Dynamic Failure of Materials and Structures*, pp. 1-28, 2010.

5. Chu T. C., W. F. Ranson and M. A. Sutton, "Applications of Digital-Image-Correlation Techniques to Experimental Mechanics", *Experimental Mechanics*, Vol. 25, No. 3, pp. 232-244, 1985.

6. Creuziger A., L. J. Bartol, K. Gall and W. C. Crone, "Fracture In Single Crystal NiTi", *Journal of the Mechanics and Physics of Solids*, Vol. 56, No. 9, pp. 2896-2905, 2008.

7. Daly S., A. Miller, G. Ravichandran and K. Bhattacharya, "An Experimental Investigation of Crack Initiation in Thin Sheets of Nitinol", *Acta Materialia*, Vol. 55, No. 18, pp 6322-6330, 2007.

8. Dayananda G. N. and M. Subba Rao, "Effect of Strain Rate on Properties of Superelastic NiTi Thin Wires", *Materials Science and Engineering*, Vol. 486, No. 1, pp. 96-103, 2008.

9. ASTM Designation, E399-90, "Standard Test Method for Plane-Strain Fracture Toughness of Metallic Materials", *Annual Book of ASTM Standards*, Vol. 3, pp. 485-510, 1997.

10. Dilibal S., “General Applications of NiTi Shape Memory Alloys (SMAs).” *Presentation*, 2008.

11. NDT Resource Center, “Fracture toughness”, http://www.ndt-ed.org/EducationResources/CommunityCollege/Materials/Mechanical/FractureToughness.htm, June 2013.

12. Euh K., J. M. Lee, D. H. Nam and S. Lee, “In-Situ Fracture Observation and Fracture Toughness Analysis of Ni-Mn-Ga-Fe Ferromagnetic Shape Memory Alloys”, *Metallurgical and Materials Transactions A*, Vol. 42, No. 13, pp. 3961-3968, 2011.

13. Falvo A., F. Furgiuele, A. Leonardi and C. Maletta, “Stress-Induced Martensitic Transformation in the Crack Tip Region of a NiTi Alloy”, *Journal of Materials Engineering and Performance*, Vol. 18, No. 5, pp. 679-685, 2009.

14. Freed Y. and L. Banks-Sills, “Crack Growth Resistance of Shape Memory Alloys by Means of a Cohesive Zone Model”, *Journal of the Mechanics and Physics of Solids*, Vol. 55, No. 10, pp. 2157-2180, 2007.

15. Gall K., N. Yang, H. Sehitoglu and Y. I. Chumlyakov, “Fracture of Precipitated NiTi Shape Memory Alloys” *International Journal of Fracture*, Vol. 109, No. 2, pp. 189-207, 2001.

16. Gollerthan S., D. Herberg, A. Baruj and G. Eggeler, “Compact Tension Testing of Martensitic/Pseudoplastic NiTi Shape Memory Alloys”, *Materials Science and Engineering*: A, Vol. 481, pp. 156-159, 2008.

17. Gollerthan S., M. L. Young, A. Baruj, J. Frenzel, W. W. Schmahl and G. Eggeler, “Fracture Mechanics and Microstructure in NiTi Shape Memory Alloys”, *Acta Materialia*, Vol. 57, No. 4, pp. 1015-1025, 2009.

18. ASTM International. Designation f2516 – 07, “Standard Test Method for Tension Testing of Nickel-Titanium Superelastic Materials”, *2008 Annual Book of ASTM Standards*, Vol. 13, 2008.

19. Jiang S. H., Y. Zhang and H. Fan, "Fracture Behavior and Microstructure of As-cast Niti Shape Memory Alloy", *Transactions of Nonferrous Metals Society of China*, Vol. 22, No. 6, pp. 1401-1406, 2012.

20. Lagoudas D. C., 2008, "*Shape Memory Alloys: Modeling and Engineering Applications*", Springer.

21. Lexcellent C., M. R. Laydi and V. Taillebot, "Analytical Prediction of the Phase Transformation Onset Zone at a Crack Tip of a Shape Memory Alloy Exhibiting Asymmetry Between Tension and Compression", *International Journal of Fracture*, Vol. 169, No. 1, pp. 1-13, 2011.

22. Lexcellent C., R. M. Laydi and V. Taillebot, "Impact of the Choice of a 3D Thermomechanical Model for Shape Memory Alloys on The Fracture and the Delamination Predictions", *Procedia Engineering*, Vol. 10, pp. 2232-2237, 2011.

23. Lexcellent C. and F. Thiebaud, "Determination of the Phase Transformation Zone at a Crack Tip in a Shape Memory Alloy Exhibiting Asymmetry Between Tension and Compression", *Scripta Materialia*, Vol. 59, No. 3, pp. 321-323, 2008.

24. Lindner S., Introduction to Digital Image Correlation. *Presentation*.

25. Liu Y. and H. Xiang, "Apparent Modulus of Elasticity of Near-Equiatomic NiTi", *Journal of Alloys and Compounds*, Vol. 270, No. 1, pp. 154-159, 1998.

26. Lopez H. F., "Transformation Induced Toughening in a NiTi Shape Memory Alloy", *Materials Letters*, Vol. 51, No. 2, pp. 144-150, 2001.

27. Lu Y. H., L. J. Qiao, and W. Y. Chu, "Characteristics of Microcrack Initiation in CuNiAl Shape Memory Alloy", *Fatigue & Fracture of Engineering Materials & Structures*, Vol. 25, No. 5, pp. 509-518, 2002.

28. Maletta C. and M. L. Young, "Stress-Induced Martensite in Front of Crack Tips in NiTi Shape Memory Alloys, Modeling Versus Experiments", *Journal of Materials engineering and performance*, Vol. 20, No. 4, pp. 597-604, 2011.

29. Maletta C., "A Novel Fracture Mechanics Approach for Shape Memory Alloys with Trilinear Stress-Strain Behavior", *International Journal of Fracture*, Vol. 177, No. 1, pp. 39-51, 2012.

30. Maletta C. and F. Furgiuele, "Analytical Modeling of Stress-Induced Martensitic Transformation in the Crack Tip Region of Nickel-Titanium Alloys", *Acta Materialia*, Vol. 58, No. 1, pp. 92-101, 2010.

31. Maletta C. and F. Furgiuele, "Fracture Control Parameters for NiTi Based Shape Memory Alloys", *International Journal of Solids and Structures*, Vol. 48, No. 11, pp. 1658-1664, 2011.

32. Miyazaki S., K. Otsuka, H. Sakamoto and K. Shimizu "The Fracture of Cu-Al-Ni Shape Memory Alloy", *Transactions of the Japan Institute of Metals*, Vol. 22, No. 4, pp. 244-252, 1981.

33. Nasser S. N. and W. Guo, "Superelastic and Cyclic Response of NiTi SMA at Various Strain Rates and Temperatures", *Mechanics of Materials*, Vol. 38, No. 5, pp. 463-474, 2006.

34. Oral A., J. Lambros and G. Anlas, "Crack Initiation in Functionally Graded Materials Under Mixed Mode Loading: *Experiments and Simulations*", *Journal of Applied Mechanics*, Vol. 75, No. 5, 2008.

35. Otsuka K. and C. M. Wayman, 1999, "*Shape Memory Materials*", Cambridge University Press, New York.

36. Pan B., K. Qian, H. Xie and A. Asundi, "Two-Dimensional Digital Image Correlation for In-Plane Displacement and Strain Measurement: a Review", *Measurement Science and Technology*, Vol. 20, No. 6, 2009.

37. Rajagopalan S., A. L. Little, M. Bourke and R. Vaidyanathan, "Elastic Modulus of Shape-Memory NiTi From In-Situ Neutron Diffraction During Macroscopic Loading, Instrumented Indentation and Extensometry", *Applied Physics Letters*, Vol. 86, No. 8, 2005.

38. Robertson S. W., A. Mehta, A. R. Pelton and RO. Ritchie, “Evolution of Crack-Tip Transformation Zones in Superelastic Nitinol Subjected to In-Situ Fatigue: A Fracture Mechanics and Synchrotron X-ray Microdiffraction Analysis”, *Acta Materialia*, Vol. 55, No. 18, pp. 6198-6207, 2007.

39. Robertson S. W., A. R. Pelton and R. O. Ritchie, “Mechanical Fatigue and Fracture of Nitinol”, *International Materials Reviews*, Vol. 57, No. 1, pp. 1-37, 2012.

40. Shabalovskaya S. A., J. Anderegg, F. Laab, P. A. Thiel and G. Rondelli, “Surface Conditions of Nitinol Wires, Tubing and As-Cast Alloys. The Effect of Chemical Etching, Aging in Boiling Water and Heat Treatment”, *Journal of Biomedical Materials Research, Part B: Applied Biomaterials*, Vol. 65, No. 1, pp. 193-203, 2003.

41. Stam G. and E. Giessen, “Effect of Reversible Phase Transformations on Crack Growth” *Mechanics of Materials*, Vol. 21, No. 1, pp. 51-71, 1995.

42. Taillebot V., C. Lexcellent, P. Malecot and R Laydi, “Analysis of the Phase Transformation Near the Crack Tip in Shape Memory Alloys”, *In European Symposium on Martensitic Transformations*, p. 06034, EDP Sciences, 2009.

43. Vendroux G., “A digital Image Correlation Program for Displacement and Displacement Gradient Measurements”, *Graduate Aeronautical Laboratories, California Institute of Technology*, Pasadena CA 91125, 1990.

44. Wang G. Z., “Effects of Notch Geometry on Stress-Strain Distribution, Martensite Transformation and Fracture Behavior in Shape Memory Alloy NiTi”, *Materials Science and Engineering: A*, Vol. 434, No. 1, pp. 269-279, 2006.

45. Wang G. Z., “Effect of Martensite Transformation on Fracture Behavior of Shape Memory Alloy NiTi in a Notched Specimen”, *International Journal of Fracture*, Vol. 146, No. 1, pp. 93-104, 2007.

46. Wang G. Z., “A Finite Element Analysis of Evolution of Stress-Strain and Martensite Transformation in Front of a Notch in Shape Memory Alloy NiTi”, *Materials Science and Engineering: A*, Vol. 460, pp. 383-391, 2007.

47. Wang X., B. Xu, Z. Yue and X. Tong, "Fracture Behavior of the Compact Tension Specimens in NiTi Shape Memory Alloys", *Materials Science and Engineering: A*, Vol. 485, No. 1, pp. 14-19, 2008.

48. Wang X. M., Z. Z. Lu and Z.F Yue, "The Effect of Notches on the Fracture Behavior in NiTi Shape Memory Alloys", *International Journal of Solids and Structures,* Vol. 46, No. 3, pp. 557-571, 2009.

49. Xiong F. and Y. Liu, "Effect of Stress-Induced Martensitic Transformation on the Crack Tip Stress-Intensity Factor in Ni-Mn-Ga Shape Memory Alloy", *Acta Materialia,* Vol. 55, No. 16, pp. 5621-5629, 2007.

50. Yan W., C. H. Wang, X. P. Zhang and Y. Mai, "Effect of Transformation Volume Contraction on the Toughness of Superelastic Shape Memory Alloys", *Smart Materials and Structures,* Vol. 11, No 6, p. 947, 2002.

51. Yan W., C. H. Wang, X. P. Zhang and Y. Mai, "Theoretical Modeling of the Effect of Plasticity on Reverse Transformation in Superelastic Shape Memory Alloys", *Materials Science and Engineering: A*, Vol. 354, No. 1, pp. 146-157, 2003.

52. Yi S. and S. Gao, "Fracture Toughening Mechanism of Shape Memory Alloys Due to Martensite Transformation", *International Journal of Solids and Structures*, Vol. 37, No. 38, pp. 5315-5327, 2000.

53. Yi S., S. Gao and L. Shen, "Fracture Toughening Mechanism of Shape Memory Alloys Under Mixed-Mode Loading Due to Martensite Transformation", *International Journal of Solids and Structures,* Vol. 38, No. 24, pp. 4463-4476, 2001.

54. Young M. L., M. F-X. Wagner, J. Frenzel, W. W. Schmahl and G. Eggeler, "Phase Volume Fractions and Strain Measurements in an Ultrafine-Grained NiTi Shape-Memory Alloy During Tensile Loading", *Acta Materialia*, Vol. 58, No. 7, pp. 2344-2354, 2010.